INFORMATION TO USERS

This manuscript has been reproduced from the microfilm master. UMI films the text directly from the original or copy submitted. Thus, some thesis and dissertation copies are in typewriter face, while others may be from any type of computer printer.

The quality of this reproduction is dependent upon the quality of the copy submitted. Broken or indistinct print, colored or poor quality illustrations and photographs, print bleedthrough, substandard margins, and improper alignment can adversely affect reproduction.

In the unlikely event that the author did not send UMI a complete manuscript and there are missing pages, these will be noted. Also, if unauthorized copyright material had to be removed, a note will indicate the deletion.

Oversize materials (e.g., maps, drawings, charts) are reproduced by sectioning the original, beginning at the upper left-hand corner and continuing from left to right in equal sections with small overlaps. Each original is also photographed in one exposure and is included in reduced form at the back of the book.

Photographs included in the original manuscript have been reproduced xerographically in this copy. Higher quality 6" x 9" black and white photographic prints are available for any photographs or illustrations appearing in this copy for an additional charge. Contact UMI directly to order.

UMI

A Bell & Howell Information Company
300 North Zeeb Road, Ann Arbor MI 48106-1346 USA
313/761-4700 800/521-0600

DESIGN AND FABRICATION OF A FREE SPACE OPTICAL INTERCONNECT SYSTEM USING HOLOGRAPHIC OPTICAL ELEMENTS

by

Darrell Lynn Ramsey

A Thesis Submitted to the Faculty of the

DEPARTMENT OF ELECTRICAL AND COMPUTER ENGINEERING

In Partial Fulfillment of the Requirements
For the Degree of

MASTER OF SCIENCE
WITH A MAJOR IN ELECTRICAL ENGINEERING

In the Graduate College

THE UNIVERSITY OF ARIZONA

1995

STATEMENT BY AUTHOR

This thesis has been submitted in partial fulfillment of requirements for an advanced degree at The University of Arizona and is deposited in the University Library to be made available to borrowers under rules of the Library.

Brief quotations from this thesis are allowable without special permission, provided that accurate acknowledgment of source is made. Requests for permission for extended quotation from or reproduction of this manuscript in whole or in part may be granted by the copyright holder.

SIGNED: Darrell Lynn Ramsey

APPROVAL BY THESIS DIRECTOR

This thesis has been approved on the date shown below:

Raymond K. Kostuk
Associate Professor
of Electrical and Computer Engineering

11-30-95
Date

Acknowledgments

I would like to specially thank (Spin) Dr. Tae Jin Kim for his help and encouragement, and many thanks to my advisor Dr. Ray Kostuk for his patience.

Good luck and good work to all past, present, and future members of the HOSER (ahem!) ADEOS Lab.

TABLE OF CONTENTS

TABLE OF CONTENTS - *Continued*

TABLE OF CONTENTS - *Continued*

TABLE OF CONTENTS - *Continued*

TABLE OF CONTENTS - *Continued*

LIST OF ILLUSTRATIONS

LIST OF ILLUSTRATIONS - *Continued*

LIST OF ILLUSTRATIONS - *Continued*

LIST OF ILLUSTRATIONS - *Continued*

LIST OF ILLUSTRATIONS - *Continued*

LIST OF TABLES

ABSTRACT

This thesis presents the design, fabrication, and analysis of a board level free space interconnect system based on holographic optical elements. The interconnect scheme is implemented in a prototype with four fully interconnected transceiver modules. The design and fabrication procedure for the holographic optical elements is presented in detail. The impact of the electro-optical and electronic components on the system is analyzed and the performance of the integrated system is presented. Alternate components for future development such as diffractive binary lens arrays are discussed.

Chapter 1
Introduction

1.1 Overview

The application of optics to communication and interconnects has evolved from the use of fiber optics in long distance telecommunication, to local area networks and limited functions in computers[1]. Optics-based communication technology has been replacing electrical communication at shorter distances as data rates increase, and this trend can be expected to continue. Optical interconnects offer several advantages over electrical signal transmission including reduced susceptibilty to electromagnetic interference and the absence of transmission-line related design limits (see for example ref. [2,3]). Of the available means for transmitting optical signals: fiber optics, planar waveguides[4], and free-space optics[5], free space interconnect offers the advantage of high density interconnects at short distances (<1m). This form of optical interconnect is uniquely suited to backplane signal connections in a high speed computer environment.

1.2 Thesis Objective

The objective of this thesis is to implement a specific proposed free-space optical interconnect structure. The interconnect structure first proposed by Dr. Kun Yii Tu and developed in other forms by Dr. Tae Jin Kim is shown in figure 1.1[6] This symmetric free space interconnect structure provides fully connected communication between the four sides of a square. The sides of the square can be individual boards or paths to multiple boards. The schematic shows a transmitter and receiver on each side with each transmitter signal broadcast to all other boards. At the receiver; either all three incoming

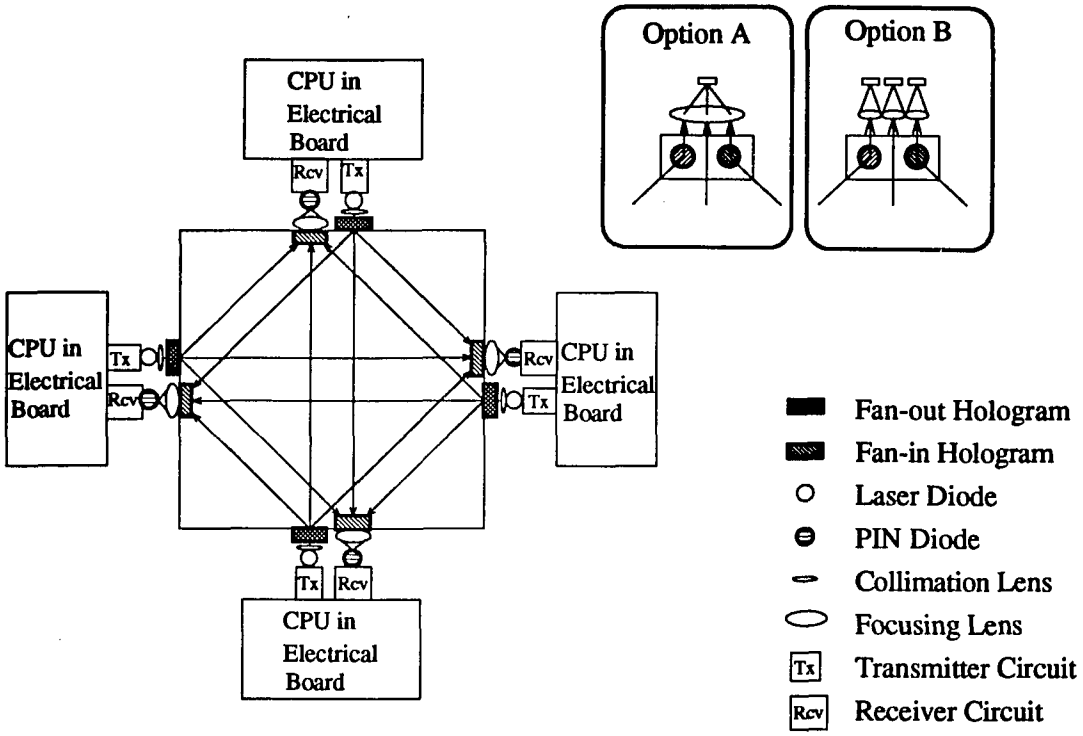

Figure 1.1 Connection Cube Schematic

signals are combined on one detector (option A), or each signal is detected on separate detectors (option B). Option A is a simple configuration which is used in the prototype system, but external sychronization of the board signals is necessary to prevent signal overlap. Option B eliminates signal interference, but is more complex. When this interconnect concept is expanded to a linear array in the vertical direction it has potential for applications such as a high speed data bus.

The schematic shown in figure 1.1 is the starting point for all work in this thesis. There are many objectives in designing and fabricating a prototype that implements this free space interconnect structure and some of these include:

-demonstrate feasibility of free space interconnects

-demonstrate modular packaging design

-demonstrate production capabilities of volume holographic elements

-demonstrate end-to-end prototype with electrical signal in and electrical signal out

-develop design issues

-form baseline for future development

One of the most important goals of this thesis is to demonstrate that a free space interconnect system can be packaged for a "real world" manufacturing environment. This means that the prototype must represent aspects of expected systems even if the physical appearance of the prototype is different from those systems. One expected property of a real world system is the modularity of components in the system. A good design separates functions into basic units, or modules, which are then assembled to create the system. This modular design approach simultaneously increases manufacturability of the modules and provides for the maximum flexibility in the system design.

Another expectation in a real world design is for "plug-in" modules that require no adjustment. This requirement is the most stringent for an optical system because the total design must provide for alignment within a given alignment error budget. The prototype design provides plug-in modularity for both the Holographic Optical Element Modules and the Electro-Optic Modules with surface references and guide-pin alignment references.

Several technologies can be considered for free-space interconnects such as etched surface relief diffractive optics (binary optics), standard refractive optics, and optically generated holographic elements. This thesis concentrates on the potential for manufacturing practical optical elements using optically generated holographic elements in

Dichromated Gelatin (DCG) films. There are strengths and weaknesses to each technology so that an optimized system may use all of them. For example, lithographically defined arrays of binary optic lenses may be useful for source collimation and focusing of arrays of optical signal beams, while large and efficient volume holographic elements can be used more effectively for beamsplitting and beam directing.

One requirement for the prototype system is that it must be constructed using available electro-optic and electronic components. The prototype system was limited to a single vertical channel because of the higher cost of obtaining array sources and detectors. Although only a single channel prototype is produced, all of the methods used can be applied to array designs. The design of the prototype system includes the capability for extension to a small linear array in the vertical direction (see chapter 2). Concepts for expanding free space interconnects to include more processing boards is discussed in chapter 7.

1.3 Chapter Summary

This thesis describes the design, development, and analysis of the connection cube free-space interconnect prototype. Chapter 2 details the opto-mechanical design of the total system and fabrication procedures. Chapter 3 presents theoretical models used to evaluate volume holographic elements and processing details for Dichromated Gelatin (DCG) films. Chapter 4 presents a design procedure for simple holographic elements and the fabrication procedure for the Holographic Optical Element Modules.

Chapter 5 describes the electro-optical components (laser diode, detector) and the electronics (laser driver, transimpedance amplifier). The detailed characteristics of the laser diode spectrum are presented for dc current and with modulation. Signal waveforms and data from the completed system are presented and analyzed.

Chapter 6 covers the system alignment analysis. An error budget is constructed from estimated fabrication errors and applied to an optical model. Data from the prototype system demonstrates alignment of the system within expected parameters.

Chapter 7 provides direction for further development of free-space interconnects by presenting alternate components and comparing them to prototype components and discussing methods of expanding the number of processing boards.

Chapter 8 provides concluding remarks on the completed system and compares free space optical interconnects to alternate technologies.

Chapter 2
Prototype Opto-Mechanical Design

The prototype design implements the connection cube configuration given in figure 1.1. The prototype design emphasizes modularity to permit step by step design and fabrication. Modular design also enables interchange of modules using different types of components, such as replacing the plastic aspheric lens with a binary diffractive lens, or different component configurations such as replacing the single source and detector with small arrays.

The major considerations in the size of the system were the available collimating lenses, laser diode, and detector. These components required approximately 9 mm center to center spacing between the laser diode and detector lenses. The constraints due to the DCG HOE plate thickness and a desire to demonstrate a compact system set the connection cube size.

2.1 Connection Cube Geometry

The symmetric beam geometry underlying the connection cube is shown in figure 2.1. This geometry allows the sides of the square to be expanded or contracted without affecting the alignment of the transceiver modules. Also, multiple modules can be arranged as shown in figure 1.2c with this symmetric geometry. The connection cube design (figure 2.2, 2.3, 2.4) uses this basic geometry with the geometrical axes of the transmitted beams and receiver beams outside the Holographic Optical Element (HOE) Module intersecting in a common plane. The actual optical beams are diverted by a glass cover slip over the transmitter hologram that provides environmental protection and a

Glass Spacer over the receiver holograms that provides beam spacing. Section 2.2 describes the optical design that produces the effective geometry of figure 2.1 while providing spacing between the receiver beams.

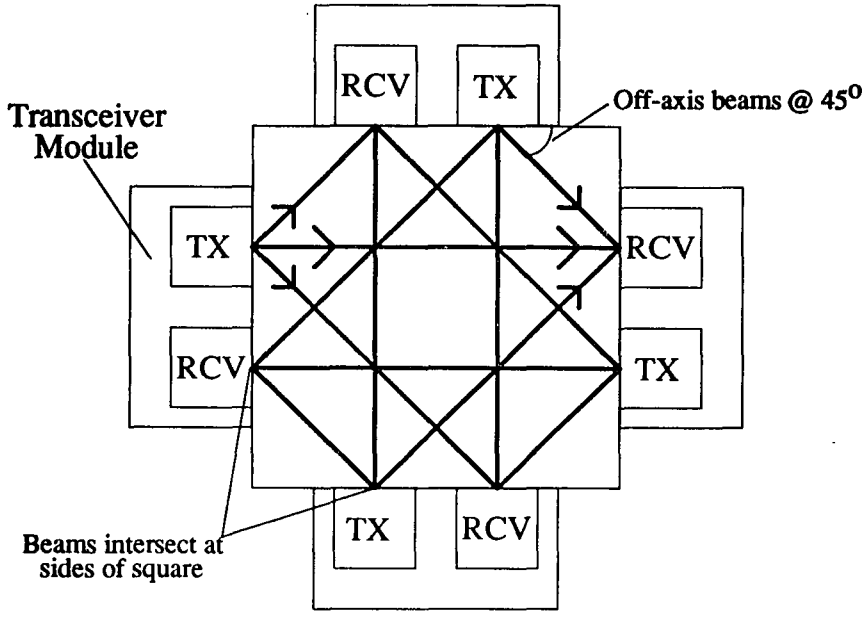

Figure 2.1 Connection Cube Geometry

2.2 Connection Cube Optical Path Detail

In the connection cube design, collimated beams produced by the laser diode and lens in the transmitter are incident normal to the cube face (figure 2.2). The transmit beam is split three ways at the transmit hologram, redirected by receiver holograms on the detector side, and three beams emerge normal to each respective cube face. The three receiver beams are then focused by an aspheric lens onto a PIN detector.

The off-axis beams are set at 45 degrees to the normal. Each off-axis beam travels to the side plates, is refracted at the surface of a glass spacer and is then diffracted by a single planar grating to produce a beam normal to the cube face. The normal beam from

the multiplexed transmit hologram travels thru a clear center space between the planar gratings. There are two reasons for producing beam separation at the detector side of the HOE plate. The first is to allow for the detection of individual beams and the second is to permit the use of an efficient single grating to redirect the beam to the cube face normal.

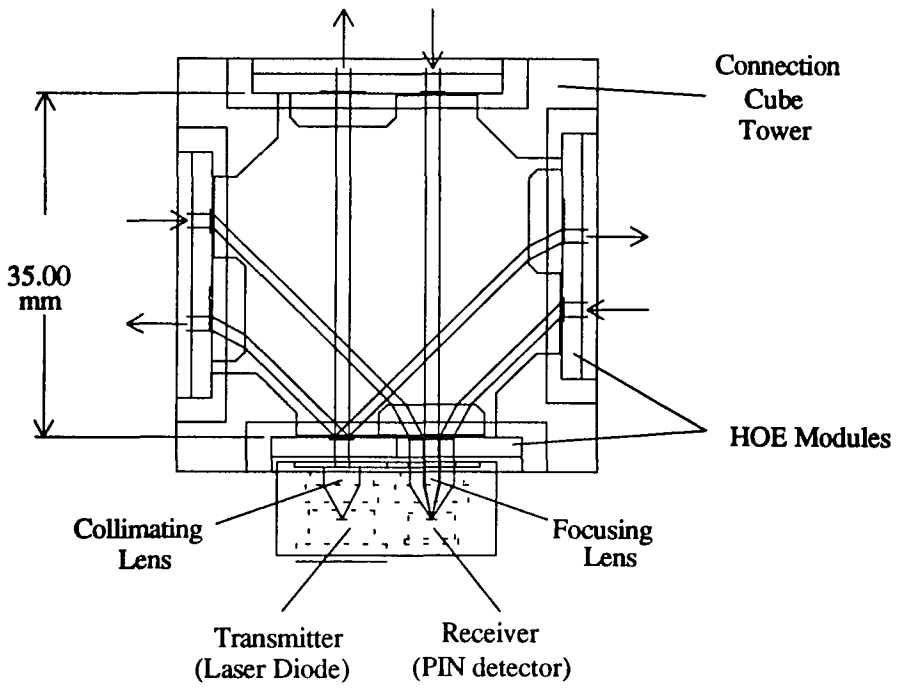

Figure 2.2 Connection Cube Optical Beam Path - Top View

The glass spacer produces the 1.5mm spacing between the receive beams with off-axis beams set at 45 degrees as shown in figure 2.3. Setting all off-axis beams at 45 degrees simplifies the recording process for the DCG holographic elements because both single and multiplexed planar gratings can then be produced with two recording beams at optimized angles with no rotation of the exposure fixture. Also, future development using a sinusoidal surface relief beamsplitter element would require equal off-axis beam angles.

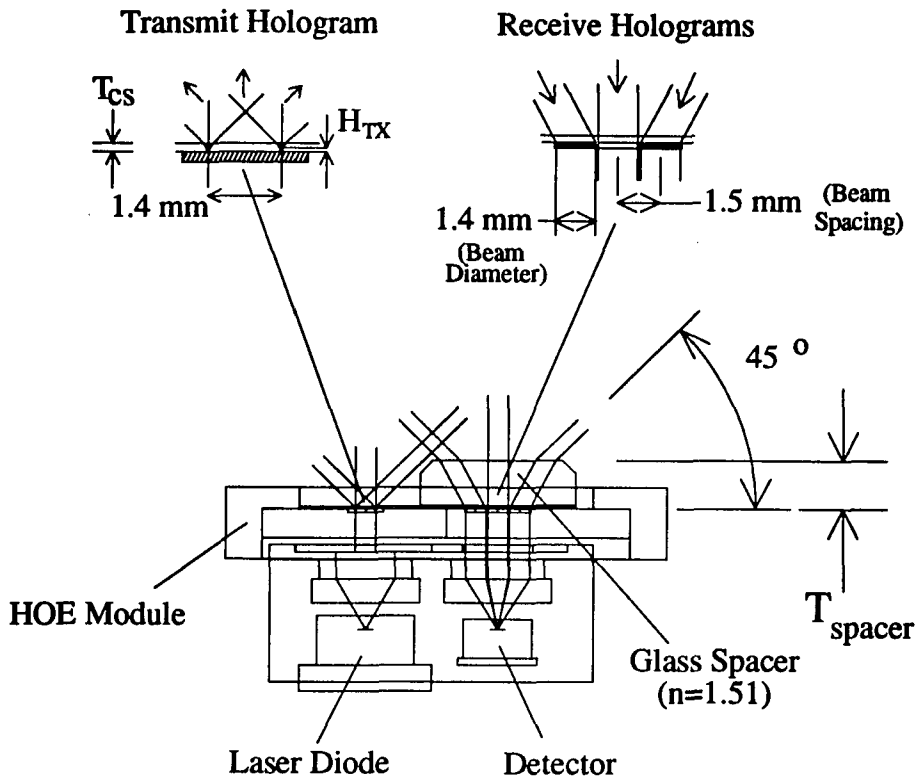

Figure 2.3 Beam Path Detail

To determine the necessary height of the glass spacer the geometry shown in figure 2.4 is analyzed. The thin cover glass used for sealing the transmit hologram places the effective center location for the transmit beams slightly above the hologram plane at height H_{TX}. To yield 45 degree off-axis beams, the apparent location of the detector for each off-axis beam must now be at the center of the receive HOE plane minus the offset height introduced by the cover glass (T_{cs}). The required glass spacer height to provide the desired lateral offset of the receive beam can be calculated using equation [2.3 and 2.6] for a glass of index n.

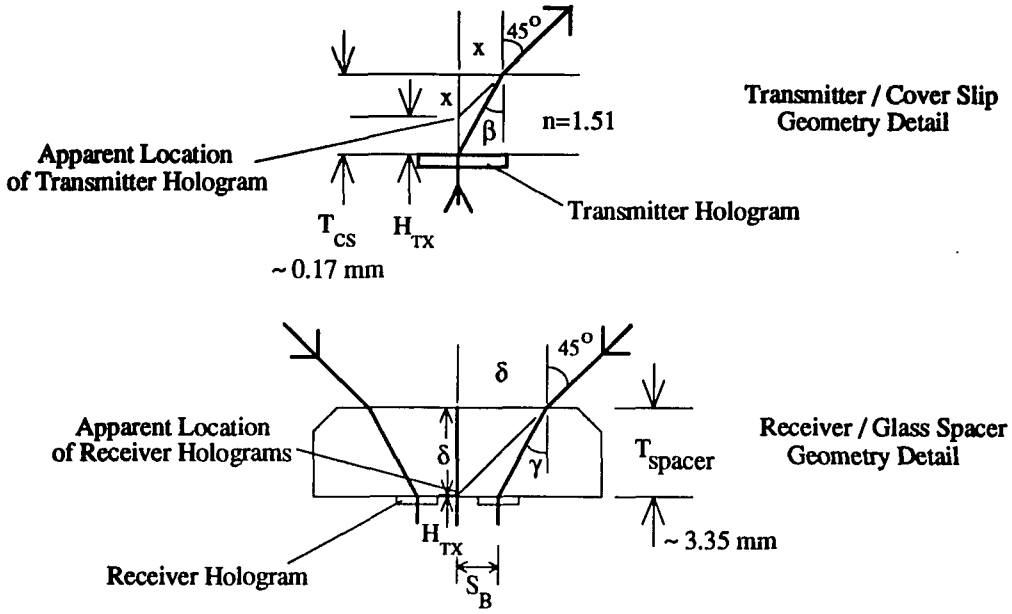

Figure 2.4 Glass Spacer Height Calculation Geometry

From figure 2.4 the relationship of the apparent transmitter location for a given cover glass height is:

[eqn 2.1] $$x = T_{CS} - H_{TX}.$$

Using Snell's law:

[eqn 2.2] $$\sin\beta = \frac{\sin 45^o}{n} = \frac{1}{n\sqrt{2}} = \frac{x}{\sqrt{T_{CS}^2 + x^2}}.$$

Equations 2.1 and 2.2 are combined to find the apparent transmitter location:

[eqn. 2.3] $$H_{TX} = T_{CS}\left[1 - 1/\sqrt{2n^2 - 1}\right].$$

Analyzing the glass spacer geometry yields:

[eqn 2.4] $$T_{spacer} = H_{TX} + \delta,$$

and:

[eqn 2.5] $$\sin\gamma = \frac{\sin 45^o}{n} = \frac{1}{n\sqrt{2}} = \frac{(\delta - S_B)}{\sqrt{T_{spacer}{}^2 + (\delta - S_B)^2}}.$$

The required glass spacer height to produce the beam spacing S_B can now be calculated:

[eqn. 2.6] $$T_{spacer} = H_{TX} + \left[\frac{S_B}{1 - \frac{1}{\sqrt{2n^2 - 1}}} \right].$$

The beam spacing (S_B) of 1.5mm was chosen to permit all 3 beams to fall in the aperture of the collimating lens. The 1.4mm beam diameter was chosen to provide adequate power from the apertured laser diode source while simulating beam diameters that would be useful in a board level free space interconnect system.

Margins from the transmit and receive beams to the glass spacer edges are required to prevent vignetting (figure 2.3). The clearance from the bevel edge for the transmit beam is 0.45 mm and the clearance for the receive beam from the bevel edge is 0.43 mm. The glass spacers were machined from a glass flat using a diamond tool on a milling machine with the optical surfaces of the flat protected during the machining process.

2.3 HOE (Holographic Optical Element) Module

The total HOE module is shown in figure 2.5 with all components. Prior to exposure, the DCG plate is cemented in the aluminum plateholder with epoxy. This subassembly is exposed and processed, and then the glass spacer and glass cover slip are mounted on the face of the HOE Module with UV cure cement. The detailed procedure for the HOE Module assembly and processing is discussed in chapter 4.

The finished HOE Module provides complete sealing of the DCG film against the

environment. An alignment reference to the connection cube is made by the edges and surface of the aluminum frame, while the E/O Module uses the guide pin holes for alignment. The hologram areas were extended in the vertical direction as shown in the figure to accommodate the potential for using linear arrays of detectors and sources in the electro-optic modules.

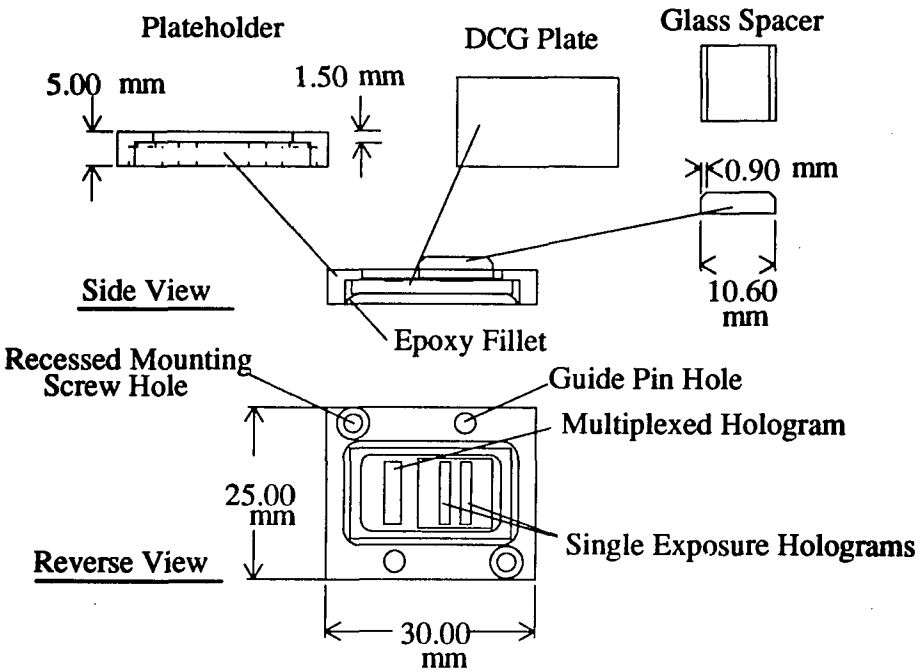

Figure 2.5 HOE Module Composite

2.4 Connection Cube Tower

The HOE Modules are held in alignment on the four sides of the Connection Cube tower shown in figure 2.6. The modules are held with mounting screws and aligned by edge and surface references as shown.

Using edge surfaces in the recess for referencing the position of the HOE Module

allowed precise measurement of the location of the surfaces during the milling operation with the available measuring instruments. Future versions of the connection cube should incorporate guide pins for all lateral alignment tasks.

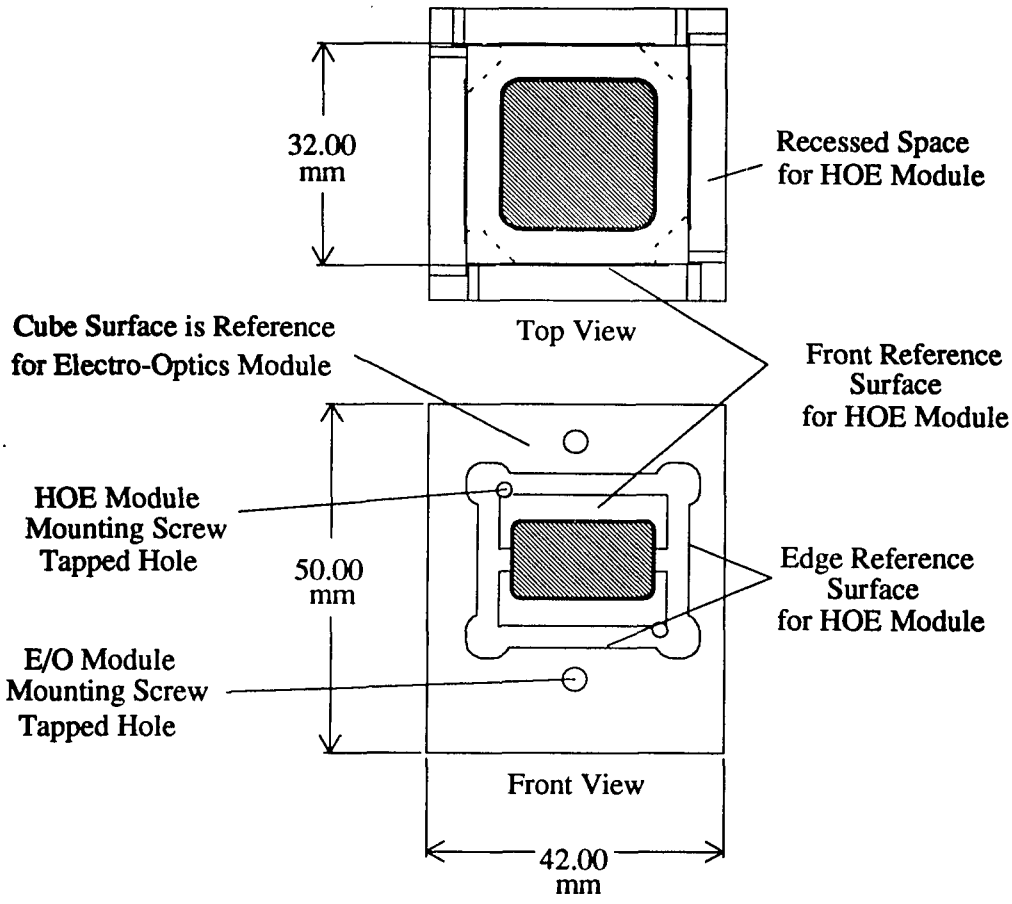

Figure 2.6 Connection Cube Tower

2.5 Electro-Optics Module

The laser diode, detector, and their respective collimating and focusing lenses are aligned and packaged in an Electro-Optics Module (E/O Module - figure 2.7) . This

module provides x-y alignment reference to the HOE plateholder via two alignment pins, while the flats on the module face provide a reference to the cube surface. The lenses are centered and held in place by lens caps (figure 2.8) that also provide a 1.4 mm aperture for the collimated source beam and a 4.8 mm aperture for the three parallel receive beams. Both the laser diode and detector are actively aligned and potted in place using thermally and electrically conductive silver epoxy.

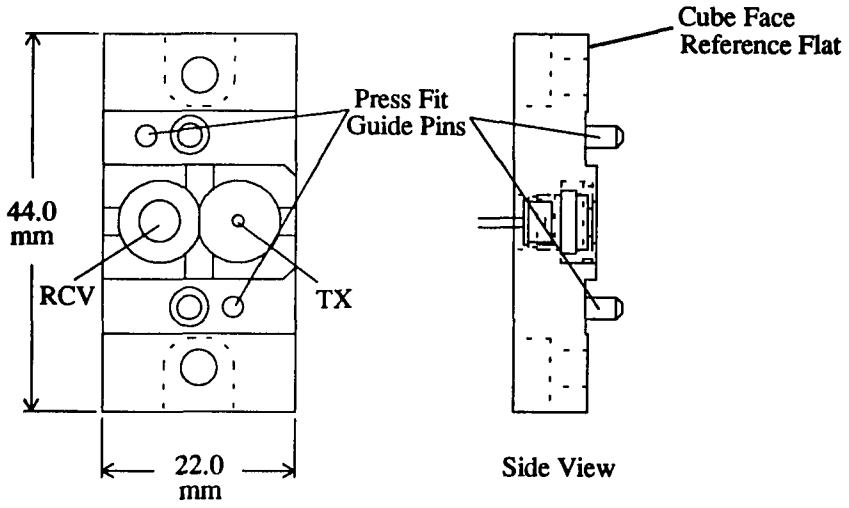

Figure 2.7 Electro-Optics Module

2.5.1 Lens Mounting

The plastic aspheric lenses are press fit into the machined aluminum lens caps that act as apertures (figure 2.8). The laser diode lens and detector lens assemblies are then mounted in their respective positions and the set screws on the side are tightened to hold the lens caps in place. As extra insurance against lens movement, a small drop of acrylic fingernail polish is put on the edge of the lens cap in the groove near the center of the holder. Portions of the lens caps were painted black to absorb stray light.

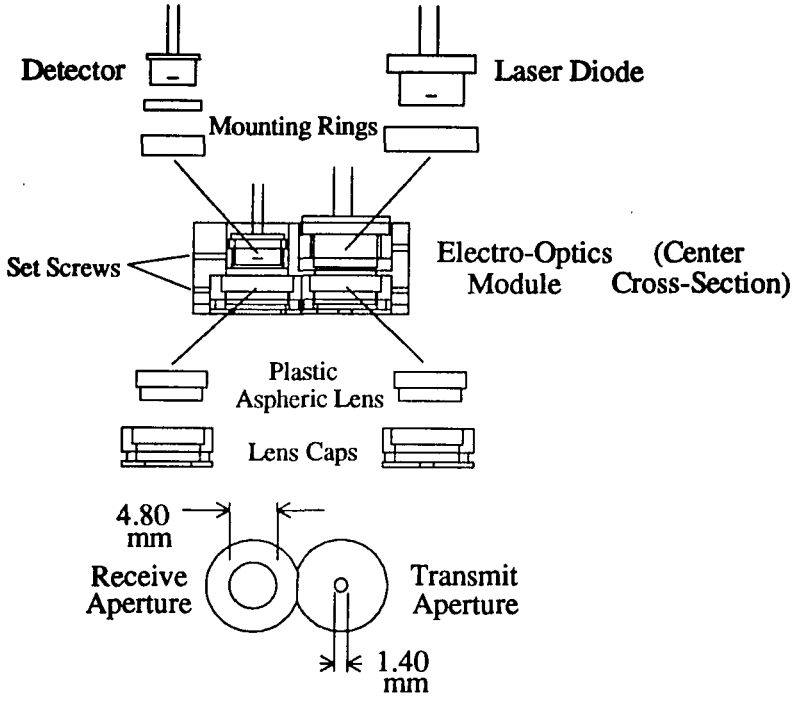

Figure 2.8 Electro-Optics Module Assembly Detail

2.5.2 Source / Detector Alignment

The laser diode source and detector are both actively aligned with respect to the plastic aspheric lenses using a three axis stage and alignment fixtures. Once aligned, a silver bearing epoxy is used to permanently fix the laser diode and detector. This silver bearing epoxy also provides electrical continuity to the cases of source and detector as well as a thermally conductive path for heat sinking the laser diode. The mounting rings allow for alignment of the laser diode and detector while reducing the amount of epoxy used. This reduces shifting during curing due to epoxy shrinkage.

2.5.2.1 Detector alignment

Alignment of the detector is achieved using the arrangement shown in figure 2.9. The alignment technique relies on a 670nm collimated laser diode adjusted normal to the fixture reference surface. The detector is underfilled at the optimal focus, so the boundaries of the optimal focus region are found by recording detector output vs. location in three axes. The detector is fixed in place by application of thermally and electrically conductive epoxy at the optimal focus location.

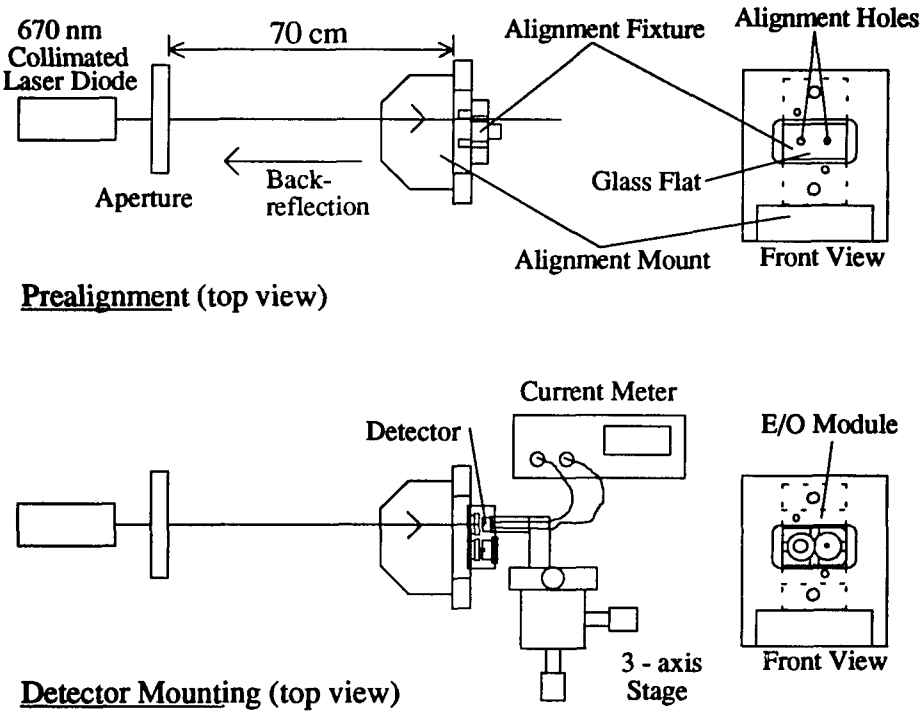

Figure 2.9 Detector Alignment and Mounting

Summary of Detector Alignment Procedure:

- Small mounting ring is epoxied to detector and allowed to cure.
- A 670 nm collimated laser diode is aligned normal to the fixture surface and coincident with the detector center reference.
- Electro-optics module is mounted on the fixture.
- Detector is mounted on a three axis stage and output current is monitored.
- Limits of the detector are found by adjusting the three axis stage and noting the micrometer measurements.
- The optimal center of the detector is calculated from the measurements.
- The large mounting ring is put in position using detector and the set screw is tightened.
- Epoxy is applied to the detector and the detector is readjusted to optimal focus.
- After curing, detector output is rechecked to ensure proper alignment.

2.5.2.1.1 Detector Alignment Data

Typical examples of the profile produced by translation of the detector in three axes through the optimum focus region are given in figure 2.10. Detector diameters were measured from the 90% power level on the data plots. Although the specified diameter of the detectors is 200 microns, all four detectors were closer to 170 microns +/-10 microns. Approximate error in selecting the horizontal and vertical center of the detector is approximately +/-10 microns. The optimum focus location is less precise as shown in figure 2.10, however, the relative insensitivity of focus causes this to be less important.

The asymmetry in the example plots of relative detector power are suspected to be due to variations in the photodiode active area or an obstructing bond wire.

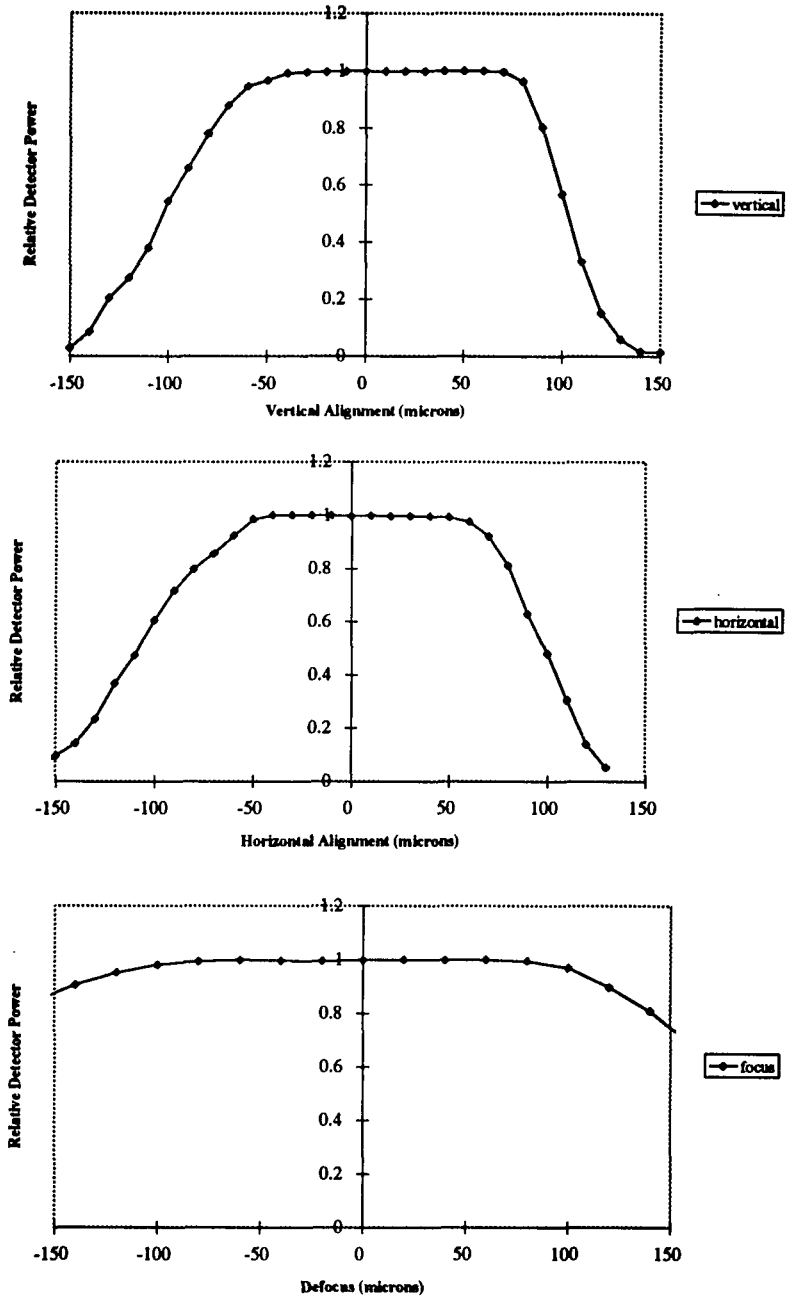

Figure 2.10 Detector Alignment Plots (E/O Module 4)

2.5.2.2 Source alignment

The laser diode is collimated and aligned in a manner similiar to the detector.

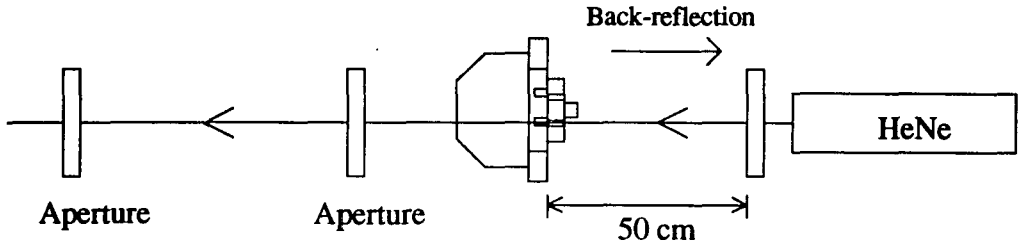

Preliminary Alignment (top view)

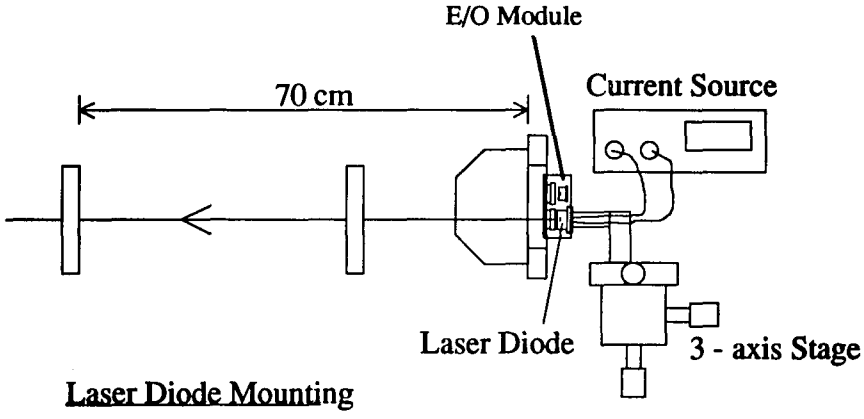

Laser Diode Mounting

Figure 2.11 Laser Diode Alignment and Mounting.

Summary of the Source Alignment Procedure:

- The HeNe beam is aligned normal to the reference surface on the fixture and aligned to the center reference hole. (figure 2.11)
- Apertures are aligned with the transmitted beam.
- Electro-optics module is mounted on the fixture.

- Laser diode holder mounted on the three-axis stage is aligned parallel to the HeNe beam.
- Laser diode is mounted and current is supplied to turn the laser diode on.
- The three axis stage is adjusted to produce a collimated beam coincident with the previously aligned apertures.
- Mounting ring for the laser diode is inserted and set in place by readjusting the laser diode to the collimation point and the set screw is tightened.
- Epoxy is applied around the laser diode and the laser diode is readjusted to the optimum collimation point and the epoxy is allowed to fully cure.
- Prior to removing the laser diode holder after epoxy cure, the alignment of the collimated beam is rechecked.

2.6 Electronics Module and Integrated System

The electronics enclosure shown in the system composite drawing (figure 2.12, 2.13, 2.14) is a simple machined aluminum housing to provide mounting of the printed circuit boards, EMI filtered power feeds, and SMA connectors for signal input and output. Grounding is improved over the aluminum case by the addition of a copper sheet that contacts the EMI filters, SMA connectors, and PC boards. Case ground is also the shield ground for the power lines. The E/O Module and the electronics module are assembled as independent modules and then mated using attachment bolts and by soldering the source and detector leads to the printed circuit boards.

The E/O Module with electronics and the HOE Module are mounted on the connection cube tower using screws. The clearance for the top screw on the E/O Module is limited because the second EMI filter was added as a fix to provide a second voltage to the laser transmitter electronics.

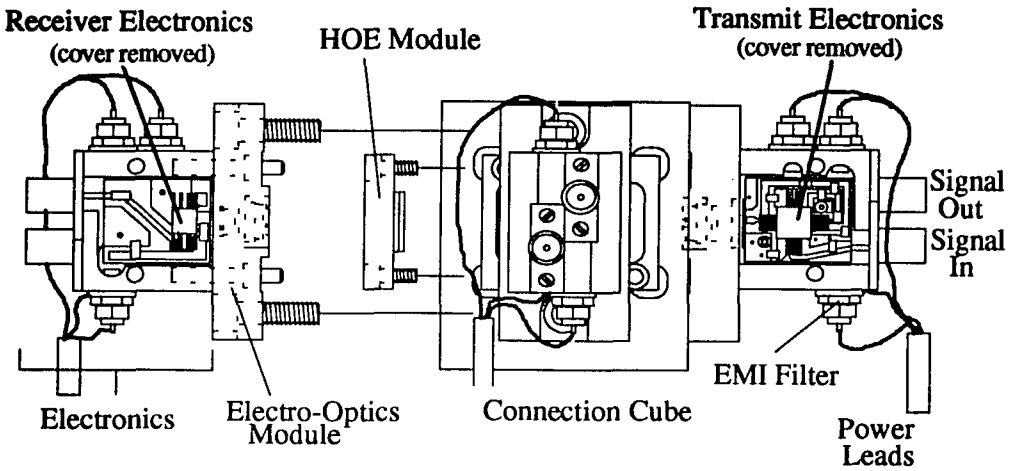

Figure 2.12 Integrated Connection Cube System - Side View

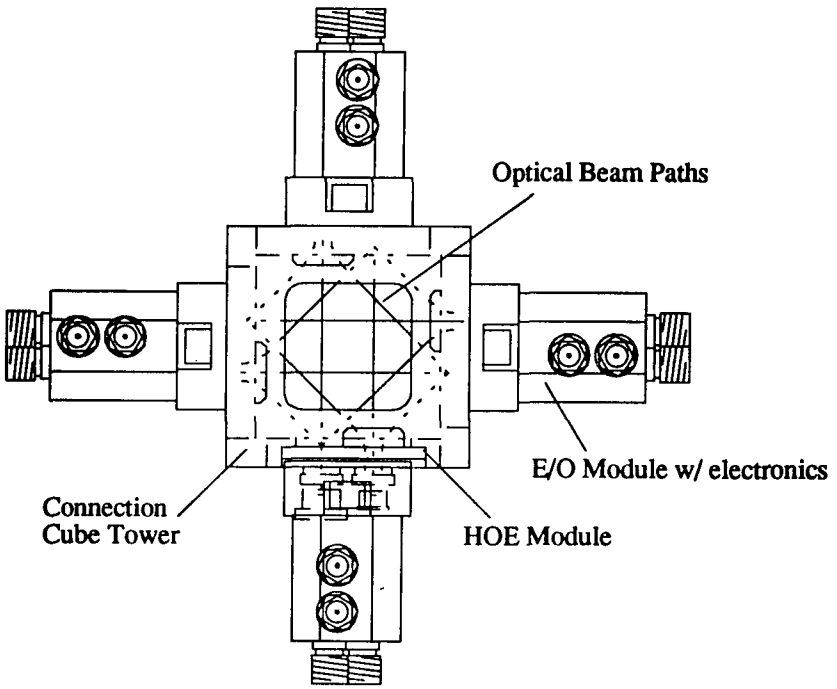

Figure 2.13 Integrated Connection Cube System - Top View

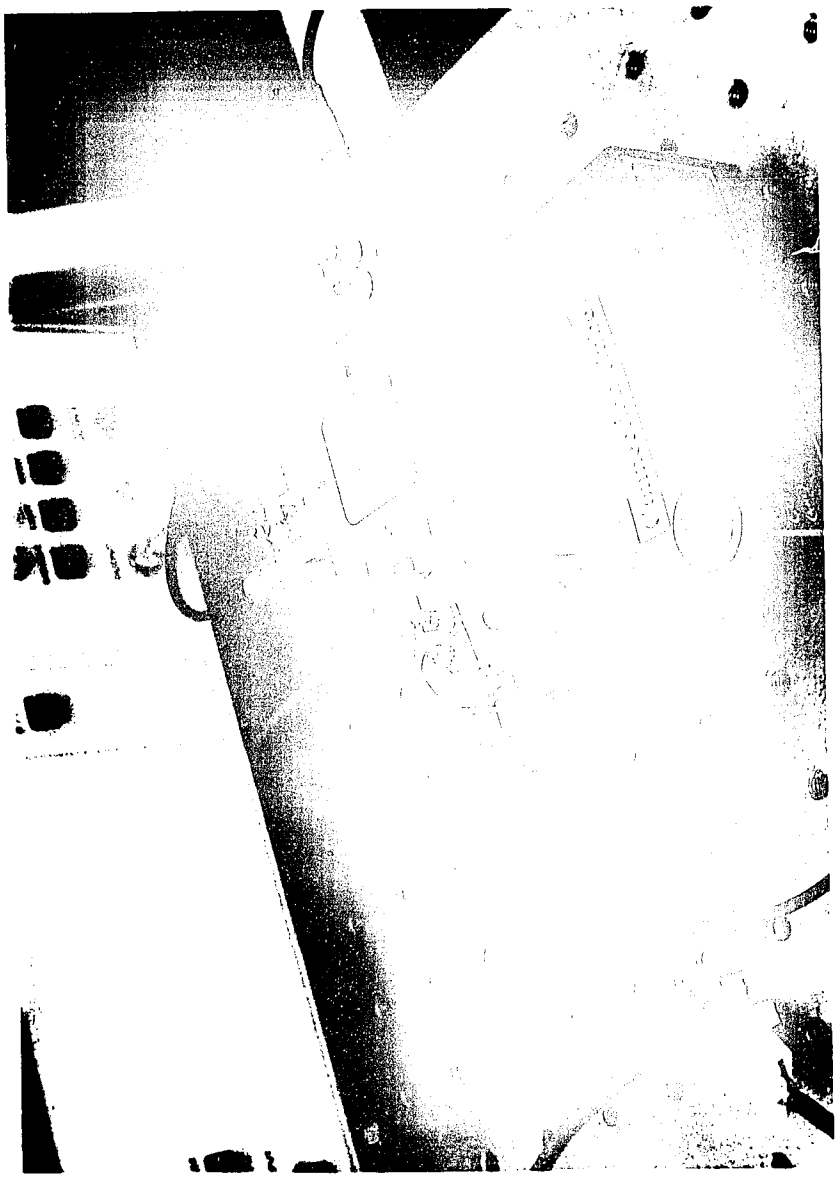

Figure 2.14 Photograph of the Completed Connection Cube System
(One E/O Module removed for clarity.)

Chapter 3
Volume Holographic Element Theory and Processing

The process of optimizing DCG holographic elements is an iterative process combining knowledge of processing effects with empirical data. In this chapter, the grating and volume hologram models, and processing induced effects necessary for describing the prototype connection cube holographic elements are discussed.

3.1 Diffraction Gratings

Diffraction gratings are capable of realizing optical functions such as beamsplitting and beam redirecting. Two fundamental categories for diffractive elements are thin gratings and volume gratings. Thin diffraction gratings, such as etched binary diffractive elements (see chapter 7), have grating features that are on the order of a wavelength in thickness. The phase front of a beam incident on a thin grating is modified at the plane of the grating causing diffraction. A volume grating, on the other hand, has significant thickness in the direction of propagation, and coupling from an incident beam to a diffracted order occurs through the thickness of the grating. A parameter that roughly defines the lower limit for the thickness of a volume grating is:[7]

[eqn. 3.1] $$Q = \frac{2\pi\lambda_o T}{n\Lambda^2} \quad , \qquad Q \geq 10 \text{ for a volume grating}$$

where λ_o=wavelength in air, T = thickness, n = average index in medium, Λ = fringe spacing (see figure 3.2).

3.2 Thin Grating Equation

The starting point for design and fabrication of a volume holographic element is the grating equation. In terms of grating period d_x the relation between an incident θ_1 and diffracted angle θ_2 is given by:[8]

[eqn. 3.2] $$d_x = \frac{m\lambda}{\sin\theta_2 - \sin\theta_1}.$$

where m=diffraction order and λ = wavelength in the medium. For optically recorded volume gratings in emulsions on rigid substrates, changes in the grating with processing do not change the grating spacing parallel to the plane of the substrate and the grating equation remains valid [9]; however, these changes do affect the Bragg angle. The angle of a diffracted beam measured normal to the suface depends only on the grating spacing d_x in the plane of the surface.

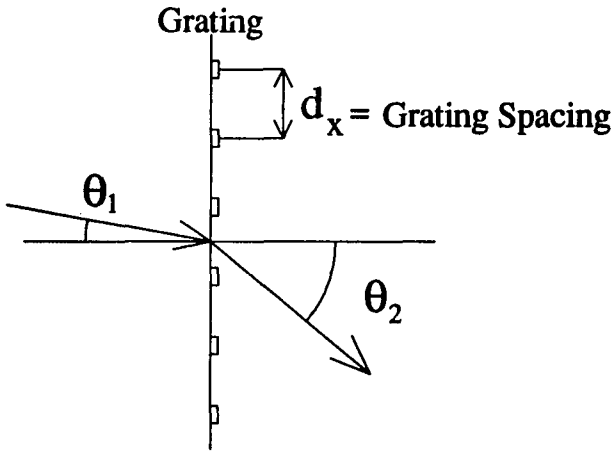

Figure 3.1 Plane Grating Geometry

The relationship between construction and reconstruction angles when the construction and reconstruction wavelengths differ is:

[eqn. 3.3] $$d_x = \frac{\lambda_c}{\sin\theta_{2c} - \sin\theta_{1c}} = \frac{\lambda_r}{\sin\theta_{2r} - \sin\theta_{1r}}.$$

Accuracy in producing the correct replay angle of an optically recorded grating is affected by the construction wavelength, reconstruction wavelength, and the recording angles. This issue is addressed in the alignment analysis (see chapter 6).

3.3 Bragg Angle Diffraction

Volume holographic gratings can theoretically diffract 100% energy into one diffracted order and are restricted in the angular range of high diffraction efficiency. Peak diffraction efficiency in a volume grating results when of a phase matching condition known as the Bragg condition is satisfied. This condition is given in equation 3.4[7] (figure 3.2) and can be defined as the angle at which the incident and diffracted beam produce closure with the grating vector $\vec{K}$ (figure 3.3).

[eqn 3.4] $$\sin\theta_B = \frac{\lambda_o}{2 \cdot n_{avg} \cdot \Lambda} \qquad \text{(Bragg condition).}$$

Snell's law ($n_{avg} \cdot \sin\theta_{1m} = \sin\theta_1$) is used to find beam angle within the medium. The input and output angles still obey the plane grating diffraction equation 3.2.

In figure 3.2, Λ is the distance between the grating planes, and the grating vector $\vec{K}$ is perpendicular to the grating planes at angle ϕ relative to the z axis and has a magnitude $2\pi/\Lambda$. Figure 3.3 shows the $\vec{K}$ vector closure condition with the incident beam propagation vector $\vec{\rho}$ and diffracted beam propagation vector $\vec{\sigma}$ having magnitudes $|\vec{\rho}| = |\vec{\sigma}| = \beta = 2\pi/\lambda$.

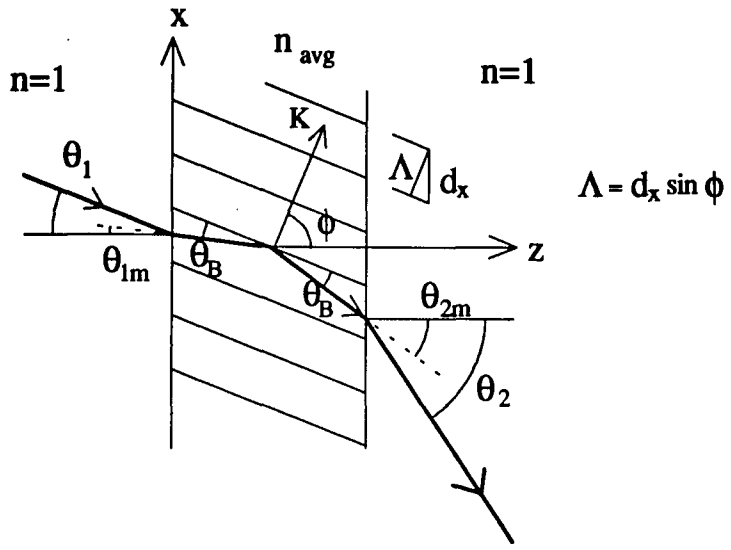

Figure 3.2 Bragg Angle Diffraction in a Volume Hologram

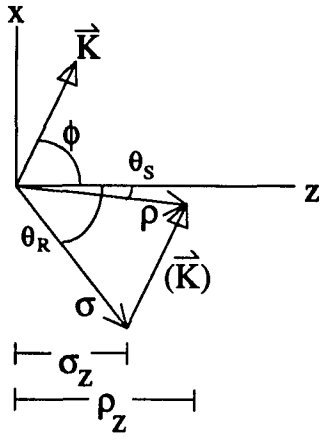

Figure 3.3 Grating Vector Geometry at Bragg Angle

3.4 Coupled Wave Theory for Single Volume Gratings.

The coupled wave analysis for volume gratings described in reference [10] gives good results for simple volume gratings. This approach allows intuitive evaluation of

effects on grating performance caused by variation in the holographic recording material during exposure and processing such as shrinkage, index change, fringe shear, and fringe bending.

Coupled wave analysis of grating diffraction is based on a description of energy coupled from an incoming reference wave **R** to an outgoing signal wave **S**. The primary simplifying assumption is that only the one reference wave and one diffracted order exist and strongly satisfies the Bragg condition. All other diffracted orders are assumed to violate the Bragg condition and are severely attenuated. This assumption limits the validity of the theory to "thick" gratings reconstructed at or near the Bragg angle. The second major assumption is that energy interchange between **R** and **S** is slow. This second assumption allows deletion of second order derivatives and boundary effects. Only the TE case is considered in this analysis because the laser diode sources are set to a polarization which corresponds to TE polarization. The geometry for diffraction in a volume hologram is shown in figure 3.4. In this figure the medium surrounding the hologram is assumed to be of the same average index.

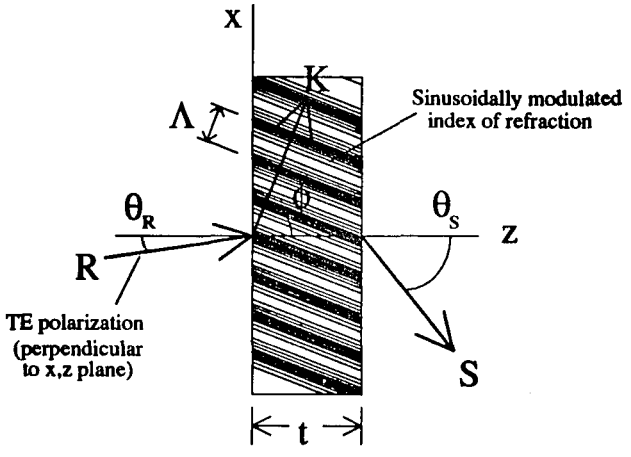

Figure 3.4 Volume Hologram Geometry

Coupled wave analysis for TE polarization begins with the scalar wave equation:

[eqn 3.5] $$\nabla^2 E + k^2 E = 0,$$

where $k^2 = \left(2\pi/\lambda_o\right)^2 \cdot \varepsilon$ and $E=E(x,z)$ is the complex amplitude of the y component of the electric field. For this analysis we will ignore absorption and assume the grating is created by a sinusoidally modulated dielectric constant. Using a unit vector $\vec{r}$ in the x,z plane:

[eqn. 3.6] $$\varepsilon = \varepsilon_o + \varepsilon_1 \cos\left(\vec{K}\cdot\vec{r}\right),$$

where $$\vec{r} = \begin{vmatrix} x \\ z \end{vmatrix}, \qquad \vec{K} = K\begin{vmatrix} \sin\phi \\ \cos\phi \end{vmatrix}, \qquad \text{and } K = \frac{2\pi}{\Lambda}.$$

Average index is defined as $n_o = \sqrt{\varepsilon_o}$ and index modulation is defined as $n_1 = \varepsilon_1 / 2\sqrt{\varepsilon_o}$.

When the index modulation is much less than the average index ($n_1 << n_0$), the propagation constant can be written as:

[eqn 3.7] $$k^2 = \beta^2 + 2\kappa\beta\left(e^{j\vec{K}\cdot\vec{r}} + e^{-j\vec{K}\cdot\vec{r}}\right) = \beta^2 + 4\kappa\beta\cos\left(\vec{K}\cdot\vec{r}\right),$$

where $\beta = 2\pi\cdot n_o/\lambda_o$ and $\kappa = \pi\cdot n_1/\lambda_o$.

The electric field in the grating for the incident reference beam of complex amplitude *R(z)* and one propagating order (signal beam) of complex amplitude *S(z)* is:

[eqn 3.8] $$E = R(z)\cdot e^{-j\vec{\rho}\cdot\vec{r}} + S(z)\cdot e^{-j\vec{\sigma}\cdot\vec{r}}.$$

The vectors $\vec{\sigma}$ and $\vec{\rho}$ are related to the grating vector $\vec{K}$ by (figure 3.3):

[eqn 3.9] $$\vec{\sigma} = \vec{\rho} - \vec{K}, \quad \text{where } |\vec{\sigma}| = |\vec{\rho}| = {2\pi \cdot n_o}/{\lambda_o} \text{ at Bragg angle.}$$

The coupled wave equations are derived by inserting the expression for the total electric field and the propagation constant into the scalar wave equation with the relationship of the vectors $\vec{\sigma}$ and $\vec{\rho}$ given by equation 3.9 The second order derivatives are then dropped under the assumption of slow energy interchange, resulting in equations 3.10 a and b.

[eqn 3.10 a] $$\frac{dR(z)}{dz} = -j\frac{\kappa}{c_R}S$$ and [eqn 3.10 b] $$\frac{dS(z)}{dz} = -j\frac{\vartheta}{c_S}S - j\frac{\kappa}{c_S}R;$$

where $$c_R = \rho_z = \cos\theta_R, \quad c_S = \sigma_z = \cos\theta_S, \quad \text{and} \quad \vartheta = \frac{\beta^2 - \sigma^2}{2\beta}.$$

The term ϑ is known as the dephasing factor. This factor causes a reduction in efficiency for the modeled volume grating as the input angle varies from the Bragg angle. The terms c_R and c_S are the z components of the reference and signal wave vectors.

When the boundary conditions $R(0)$=1 and $S(0)$=0 are applied to equation 3.10 the diffracted amplitude S is described by:

[eqn 3.11] $$S = -j\sqrt{\frac{c_R}{c_S}} \cdot e^{-j\xi} \cdot \frac{\sin\sqrt{\upsilon^2 - \xi^2}}{\sqrt{1 - \xi^2/\upsilon^2}},$$

where $$\upsilon = {\pi n_1 t}/{\lambda\sqrt{c_R c_S}}, \quad \xi = {\vartheta \cdot t}/{2c_S}, \quad \text{and t = the grating thickness.}$$

The final result for this analysis is the diffraction efficiency which is given by:

[eqn 3.12] $$\eta = \frac{|c_S|}{c_R} \cdot S \cdot S^* = \frac{\sin^2 \sqrt{\upsilon^2 + \xi^2}}{\left(1 + \xi^2/\upsilon^2\right)}.$$

This expression is used in chapter 4 to model diffraction efficiency vs. input beam angle for the single exposure gratings.

3.5 Multiplexed Grating Model

The extension of coupled wave analysis for TE polarization to incoherently exposed multiplexed gratings is relatively straightforward [11,12]. The multiplexed gratings to be analyzed are the simplest case for a multiplexed grating in that there are only two superimposed gratings and the gratings are not strongly coupled. Cross coupling between the diffracted +/- 45 degree beams is negligible and will be neglected.

The index modulation and the propagation constant in a multiplexed grating can be expanded for N gratings from the single grating expressions:

[eqn 3.13] $$n = n_O + \sum_{i=1}^{N} n_i \cos(\vec{K}_i \cdot \vec{r}), \qquad \text{and}$$

[eqn 3.14] $$k^2 = \beta^2 + 4\beta \sum_{i=1}^{N} \kappa_i \cos(\vec{K}_i \cdot \vec{r}), \qquad \text{where } \kappa_i = {\pi n_i}/{\lambda_o}.$$

Similiar to equation 3.8, the total E field for multiple (N) gratings can be written:

[eqn 3.15] $$E = R(z)e^{-j\vec{\rho}\cdot\vec{r}} + \sum_{i=1}^{N} S_i(z)e^{-j\vec{\sigma}_i\cdot\vec{r}}.$$

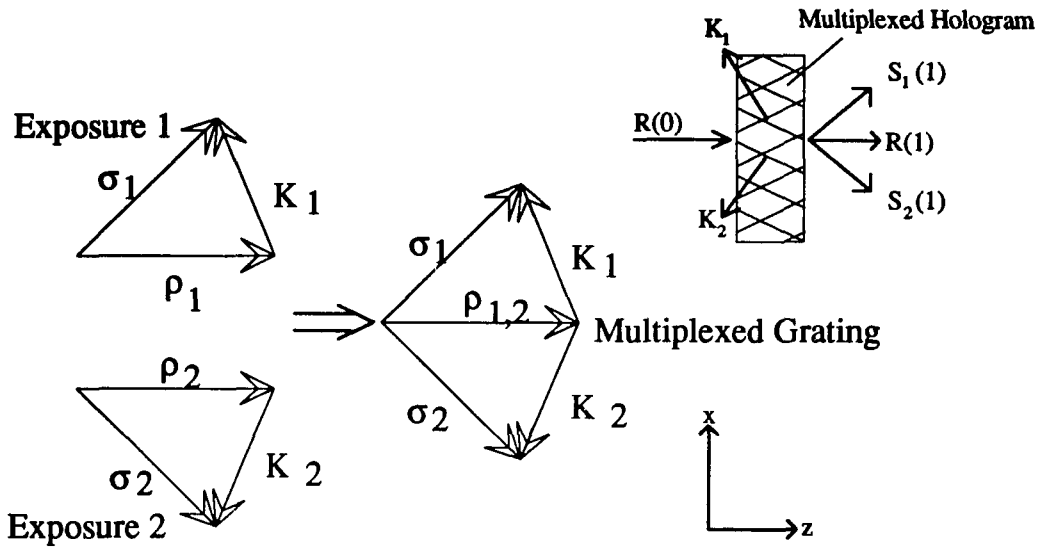

Figure 3.5 Incoherently Exposed -Multiplexed Grating Vectors

Similiar to equation 3.10, the coupled wave equations can be found by inserting equation 3.14 and 3.15 into the scalar wave equation 3.5. Using the same assumption of slow energy exchange and retaining only one diffracted order for each grating, the coupled wave equations written in matrix form are:

[eqn 3.16]
$$\frac{\mathrm{d}}{\mathrm{d}z}\overline{RS}(z) = -j\overline{M}\cdot\overline{RS}(z).$$

With only two superimposed gratings and cross-coupling neglected, the matrices $\overline{RS}(z)$ and $\overline{M}$ are:

$$\overline{RS}(z) = \begin{bmatrix} R(z) \\ S_1(z) \\ S_2(z) \end{bmatrix} \quad \text{and} \quad \overline{M} = \begin{bmatrix} 0 & \frac{\kappa_1}{c_R} & \frac{\kappa_2}{c_R} \\ \frac{\kappa_1}{c_{S_1}} & \frac{\vartheta_1}{c_{S_1}} & 0 \\ \frac{\kappa_2}{c_{S_2}} & 0 & \frac{\vartheta_2}{c_{S_2}} \end{bmatrix},$$

where $c_R = \frac{\rho_z}{\beta}$ $c_{S_1} = \frac{\sigma_1 z}{\beta}$ $c_{S_2} = \frac{\sigma_2 z}{\beta}$,

and $\vartheta_1 = \frac{\beta^2 - \sigma_1^2}{2\beta}$ $\vartheta_2 = \frac{\beta^2 - \sigma_2^2}{2\beta}$,

and $\kappa_1 = \frac{\pi \cdot n_1}{\lambda_o}$ $\kappa_2 = \frac{\pi \cdot n_2}{\lambda_o}$.

The matrix equation 3.16 can be solved by:[13]

[eqn 3.17] $$\overline{RS}(z) = \overline{W} \cdot \overline{\lambda(z)} \cdot \overline{C},$$

where $\overline{\lambda(z)}$ is a matrix formed from the eignvalues $\lambda_{i,i}$ of $\overline{M}$

[eqn 3.18] $$\overline{\lambda(z)} = \begin{bmatrix} e^{-j\lambda_{1,1} \cdot z} & 0 & 0 \\ 0 & e^{-j\lambda_{2,2} \cdot z} & 0 \\ 0 & 0 & e^{-j\lambda_{3,3} \cdot z} \end{bmatrix},$$

and $\overline{W}$ = the matrix of eignvectors of $\overline{M}$. $\overline{C}$ is a matrix of constants determined by boundary conditions. In this case the initial conditions at the grating input are:

[eqn 3.19] $$\begin{bmatrix} R(0) \\ S_1(0) \\ S_2(0) \end{bmatrix} = \begin{bmatrix} 1 \\ 0 \\ 0 \end{bmatrix}.$$

The $\overline{C}$ matrix now can be found from equation 3.17 by inverting the $\overline{W}$ matrix and applying the condition z = 0 to the eigenvalue matrix $\overline{\lambda(z)}$.

[eqn 3.20] $$\overline{C} = \left(\overline{W}^{-1}\right) \cdot \begin{bmatrix} 1 \\ 0 \\ 0 \end{bmatrix}.$$

The resulting $R(t)$, $S_1(t)$, and $S_2(t)$ from equation 3.17 (t = hologram thickness) are the output beam efficiencies. These beam efficiencies are used to model the HOE Module multiplexed gratings in chapter 4.

3.6 Mechanism of Hologram Formation in Dichromated Gelatin (DCG)

Dichromated Gelatin (DCG) is a mixture of gelatin and ammonium dichromate [$(NH_4)_2Cr_2O_7$]. Of the large number of media available for optically recorded holograms[14], DCG films excel in producing high efficiency, high optical quality holograms. Photosensitive films are formed from spinning and drying an aqueous solution of gelatin and ammonium dichromate onto glass substrates.[15] Holograms are formed in the DCG film by the interference of coherent light beams that produce areas of high and low exposure intensity corresponding to interference fringes. Development of the DCG film converts these areas of high and low exposure to an index modulation that forms the hologram.

Holograms are formed in DCG film by a complex process which is not thoroughly understood. The sensitizing ammonium dichromate provides Cr^{6+} chromium ions when it is dissolved in the gelatin, and these Cr^{6+} ions produce Cr^{3+} ions by light absorption. The Cr^{3+} ions then produce crosslinking between the complex chains of molecules present in the gelatin. This crosslinking modifies the hardness of the gelatin and produces index modulation after development.[16,17]

The complex process of crosslinking and film hardening is dependent on the pH in the film and therefore it is dependent on the humidity conditions experienced by the film after spinning and during exposure[15,18]. Experimental data on the effects of humidity curing on film swelling and film sensitivity are presented in section 3.9.

3.7 DCG Film Plate Preparation and Processing

The Dichromated Gelatin films used are prepared in the laboratory using the following optimized procedure.[15]

3.7.1 DCG Film Plate Preparation

A. Plate cleaning procedure

1. Clean 10 x 12.5 cm glass plates with soap.
2. Boil cleaned plates in 10% ammonia solution.
3. Ultrasonic clean plates 5 minutes (DI water / soap).
4. Rinse plates in DI water.
5. Bake plates at 75 ^{o}C for 15 minutes.

B. Film Spinning procedure

1. Mix 30 gm Gelatin and 250 ml DI water and let gelatin absorb water for 20 minutes.
2. Place mixture in 60 ^{o}C hot water bath and mix in 10 gm Ammonium Dichromate.
3. Warm glass plates in oven.
4. Filter DCG mixture and stabilize temperature (40 ^{o}C)
5. Apply DCG mixture uniformly to glass plate on chuck.
6. Spin at 80 rpm for 3 minutes with hot air fan on.
7. Bake plates at 55 ^{o}C for 20 minutes.
8. Store plates in humidity chamber for 24 hours (50 to 60 % relative humidity).

3.7.2 DCG Film Processing

The exposed plates are developed using immersion in a standard photographic fixing solution with a rapid dehydration process using isopropyl alcohol and a final bake.

1. Agitate plates in Kodak rapid fixer (100 ml part A,
   13 ml part B, 2 ml Photoflo + DI water to make 400ml) for 3 min.
2. Agitate plates in DI water 30 seconds.
3. Dehydration - Agitate plates in
   a. 50% isopropyl at 65 ^{O}C for 30 seconds.
   b. 1st bath 100% iso. at 65 ^{O}C for 30 seconds.
   c. 2nd bath 100% iso. at 65 ^{O}C for 30 seconds.
4. Bake plates at 75 ^{O}C for 20 minutes

3.8 Processing Effects

An empirical approach to design and fabrication of DCG holographic elements is necessary because of the large number of process variables in producing DCG holographic elements. The design process for the prototype HOE modules is seriously impacted by processing changes that induce Bragg angle shifts because the large diffracted beam angle (45 degrees) and the wavelength shift from construction to reconstruction require large offsets in the exposure beam angles with respect to the hologram normal. Processing induced changes that can cause significant Bragg angle shift in DCG volume holograms include average index change and emulsion swelling.

3.8.1 Average Index Change

Average index in exposed and processed DCG holograms is different from that of the unprocessed film. This average index change introduces a change in the Bragg angle

from the exposure condition. Measurements of average index in an index modulated medium or a processed film is a difficult task, but recent work[19] indicates that the unprocessed film has an index of about 1.58 while the exposed and processed film has a reduced index of about 1.46. With the exposure angles and wavelength given in chapter 4 for the prototype HOE modules, this index change alone would produce a Bragg angle shift of 2.3 degrees for reconstruction at 675nm. The direction of the Bragg angle shift for the given index change is the same as that for swelling in the emulsion.

3.8.2 Emulsion Thickness Change

Wet processed holographic materials commonly have an emulsion thickness change from exposure to final hologram[20]. The net change for the DCG process used here is typically in the direction of swelling. The change in the fringe plane angles and the grating vector is illustrated in figure 3.6. Compensation of this Bragg angle shift during exposure requires increasing beam angles with respect to the hologram normal.

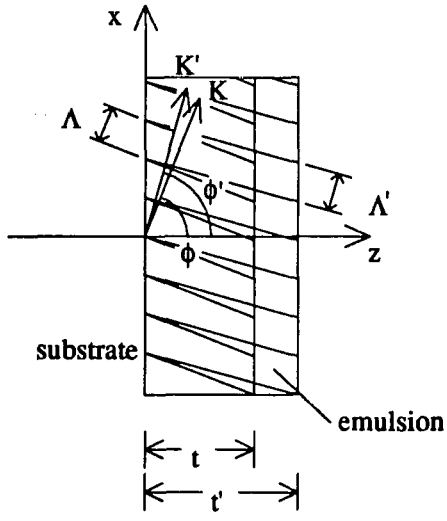

Figure 3.6 Grating Vector Rotation Due to Emulsion Swelling

The rotation in the grating vector and the change in vector magnitude can be calculated from the relations:

[eqn. 3.21] $$\frac{t'}{t} = 1 + \Delta t = \frac{\tan\phi'}{\tan\phi},$$

where t = original thickness and t' = post process thickness, and:

[eqn. 3.22] $$\frac{\Lambda'}{\Lambda} = \frac{\sin\phi'}{\sin\phi} \quad , \qquad \text{and} \qquad |K'| = \frac{2\pi}{\Lambda'}.$$

3.9 Humidity Curing of DCG Film

Controlling Bragg angle shifts in high fringe slant gratings is important and humidity curing is a key film process parameter providing that control. Several factors can affect the severity of swelling in DCG films such as ammonium dichromate concentration, film thickness, and relative humidity during curing[15,17,18]. For the optimized process used, the ammonium dichromate concentration and the film thickness are determined, leaving humidity curing as the key process variable. Humidity curing of spun and baked DCG films in a relative humidty above 50% produces reduction in post process emulsion swelling. The mechanism behind this reduction in swelling appears to be a dark reaction caused by the ammonium dichromate producing "hardening" in the film. A reduction in the pH of the film is associated with this dark reaction. An additional consequence of this change in the film is a reduction in the film sensitivity.

As a test, several DCG test plates were produced and humidity cured for varying lengths of time. All plates were spin coated and baked together. Uncured plates were placed directly in a light tight storage box at ambient relative humidity (20% to 25%) and

room temperature. The humidity cured plates were placed in a humidity box using calcium chloride and water to stabilize relative humidity in the 55% to 65% range at room temperature. Each humidity cured plate is transferred to the ambient storage box as it reached the appropriate cure time. A span of 48 hours between the removal of the last humidity cured plate and subsequent exposure was allowed to stabilize all plates to ambient conditions.

The 514.5nm line of the Argon Ion Laser was used to expose plates with 4 humidity cure times (0, 24, 48, 80 hours) at 3 different exposure conditions (ϕ = 70.8, 73.5, 76.4 degrees) for several exposure energies (10 to 140 mJ/cm2). Direct thickness measurements were made of the unprocessed plates and the exposed and processed plates using a Tencor Alpha-Step 200 profilometer.

3.9.1 Effect of Humidity Curing on Bragg Angle Shift

The measured Bragg angle shift vs. humidity cure time for the different fringe plane angles shown in figure 3.7 demonstrates clear reduction in shift for increasing cure time. The cause for the Bragg angle shift is revealed in figure 3.8 with the processing induced swelling. Thickness in the unprocessed plates is nearly identical, attesting to process control in the spin coating process. Swelling in the exposed and processed plates is large with less humidity curing and tapers off for longer curing time.

The coupled wave model was used to derive effective thickness and swell factor that would produce the Bragg shift seen in figure 3.7. The modeling results are compared to measured values in Table 3.1. The swell factor was defined as the post-processed film thickness divided by the film thickness during exposure. Pre-process film average thickness was set at 1.58 while the post process index used was 1.47.

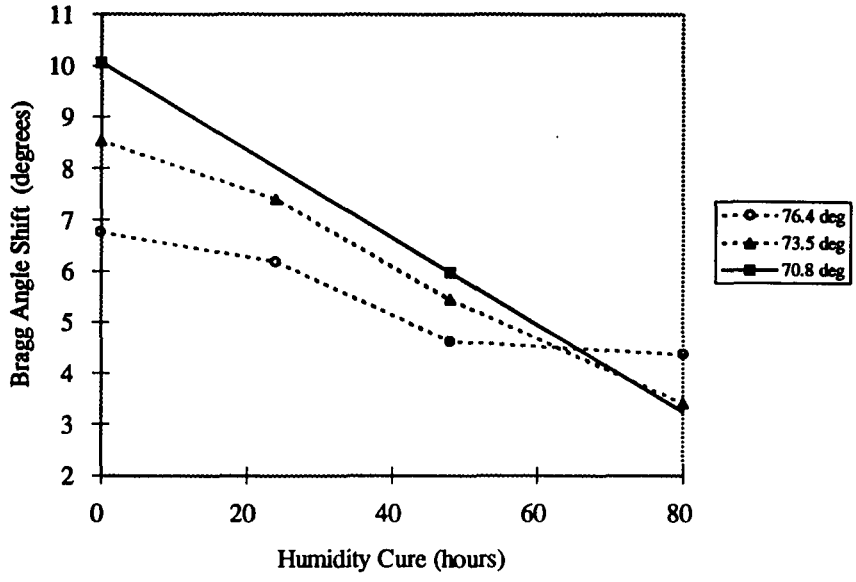

Figure 3.7 Bragg Angle Shift vs. Humidity Cure Time

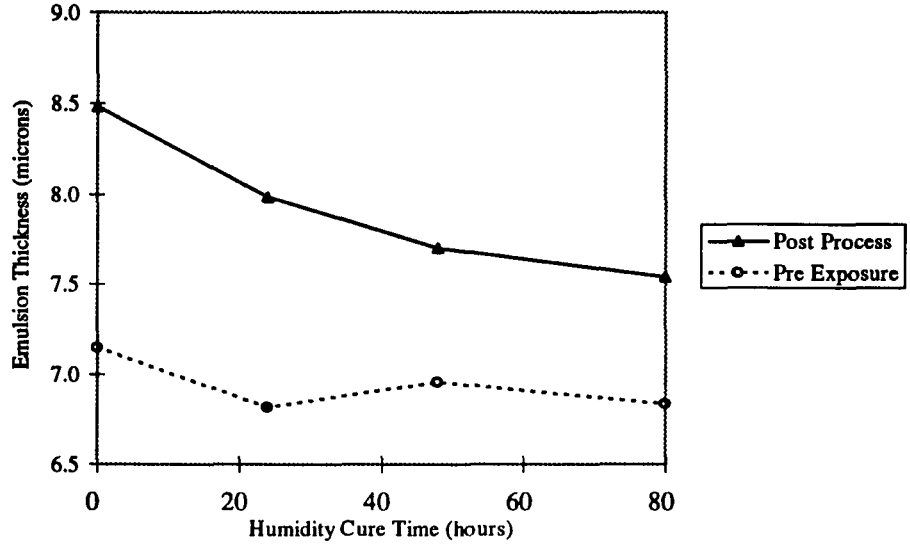

Figure 3.8 Emulsion Thickness Change vs. Humidity Cure

Table 3.1 Comparison of Measured Swell and Thickness to Model Swell and Thickness

	Measured Swell Factor	Measured Thickness	Model Swell Factor	Model Thickness
0 hour cure	1.19	8.48 μm	1.38	7.3 μm
24 hour cure	1.17	7.98 μm	1.33	7.4 μm
48 hour cure	1.11	7.70 μm	1.14	7.0 μm
80 hour cure	1.10	7.54 μm	1.08	7.0 μm

Two things are noted from this data; first, the swell required to produce the observed Bragg shift is much larger than the uniform swell measured in the emulsion, and second, the model thickness is less than the measured thickness. These two facts point to the possibility that the hologram is not uniform throught the thickness of the film and the swelling is acting disproportionately on a hologram that is effectively thinner than the total measured film thickness. This reduced effective hologram thickness might be explained by the exponential absorption of the exposure beams as they propagate through the film and/or by the non-uniform effect of wet processing that has a greater effect on the outside of the emulsion than on the side close to the substrate.

3.9.2 Effect of Humidity Curing on Exposure Sensitivity and Diffraction Efficiency

Exposure sensitivity vs. diffraction efficiency for increasing humidity cure time is shown in figure 3.9. The tradeoff between sensitivity and diffraction efficiency is important because it is easier to obtain a specific diffraction efficiency for a multiplexed element if the slope of the efficiency vs. exposure curve is not steep; however, too much humidity curing may reduce total efficiency of the element.

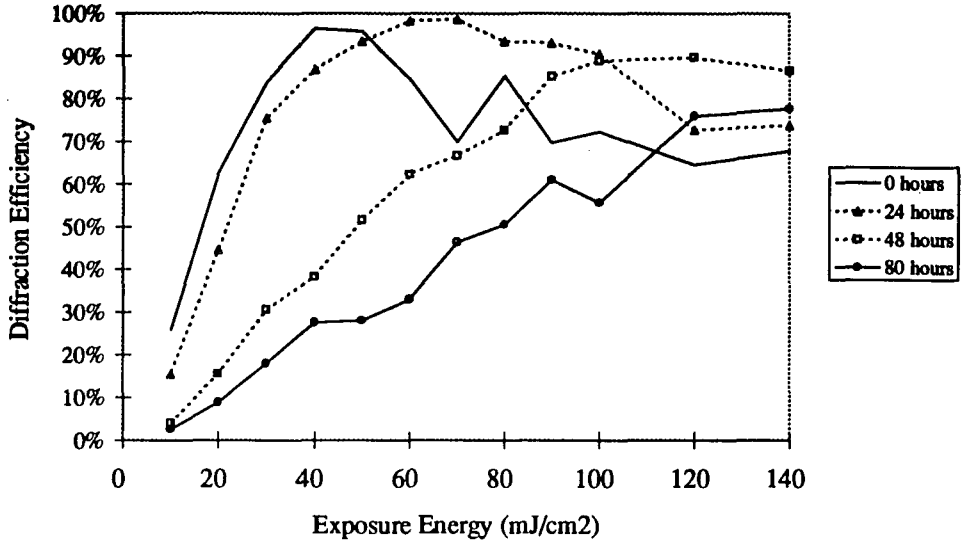

Figure 3.9 Efficiency vs. Exposure Energy for different Humidity Curing Time (compensated for Fresnel reflection)

3.10 Bragg Angle Shift Variation with Exposure

Differences in the processing induced shrinkage of exposed and unexposed hologram materials can cause Bragg angle shifts that are dependent on exposure. Differential shrinkage between exposed and unexposed areas in DCG holographic materials exists to some degree and expresses itself as relief patterns on the surface of the hologram[21]. If Bragg angle shift is dependent on exposure then both the hologram efficiency and Bragg angle shift must be simultaneouly optimized with respect to exposure.

Figure 3.10 shows the measured variation in Bragg angle shift for a broad exposure range. This data is consistent with data in reference [12] for more highly slanted gratings. The graph includes holograms on DCG substrates that were humidity cured for

different lengths of time. Although there is some variation with exposure, the maximum amount of variation is small compared to the Bragg angle shifts induced by emulsion swelling. It is also evident that humidity curing has little impact on the variation. The important consequence of small Bragg angle shift variation with exposure is that Bragg shift compensation and diffraction efficiency optimization can be carried out independently, simplifying holographic element design.

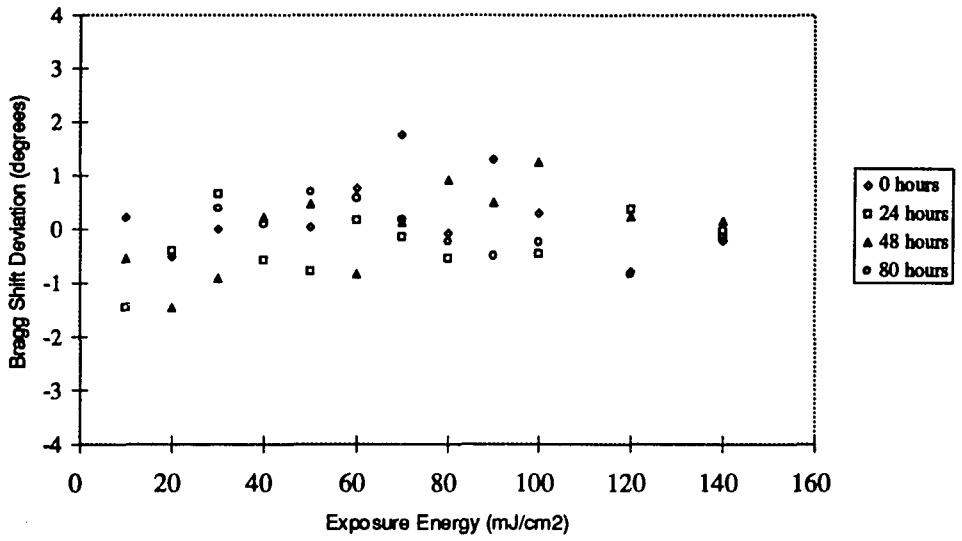

Figure 3.10 Bragg Angle Deviation vs. Exposure Energy for Humidity Cured Plates

Chapter 4
Holographic Optical Element Design Process and Module Fabrication

The volume hologram models and processing effects presented in the previous chapter are now applied to the task of fabricating the HOE Modules. An iterative design procedure for producing efficient holographic elements is developed and data from the final HOE Modules is presented.

4.1 Holographic Design Process

The large number of variables introduced into the hologram fabrication process by film fabrication, humidity curing, and processing induced effects makes some measure of empirical optimization necessary. The flowchart given in figure 4.1 details a procedure for producing the simple holographic elements for the HOE Modules. The purpose of the optimization procedure is to bring the angle of peak diffraction efficiency (Bragg angle) into coincidence with the desired replay angle, and to find the exposure energy that produces the optimum efficiency. The replay angles themselves do not require optimization because they are determined only by the grating period d_x and are thus determined in the hologram by the construction angles and the construction wavelength, both of which are well known quantities (see chapter 6).

The design process begins with the specification of the desired final holographic element. The optimum reconstruction wavelength (675nm) and the desired replay angles (0,+/-45 deg) are used to calculate the necessary grating period d_x in the plane of the hologram. This grating period does not change in the optimization process. The fringe

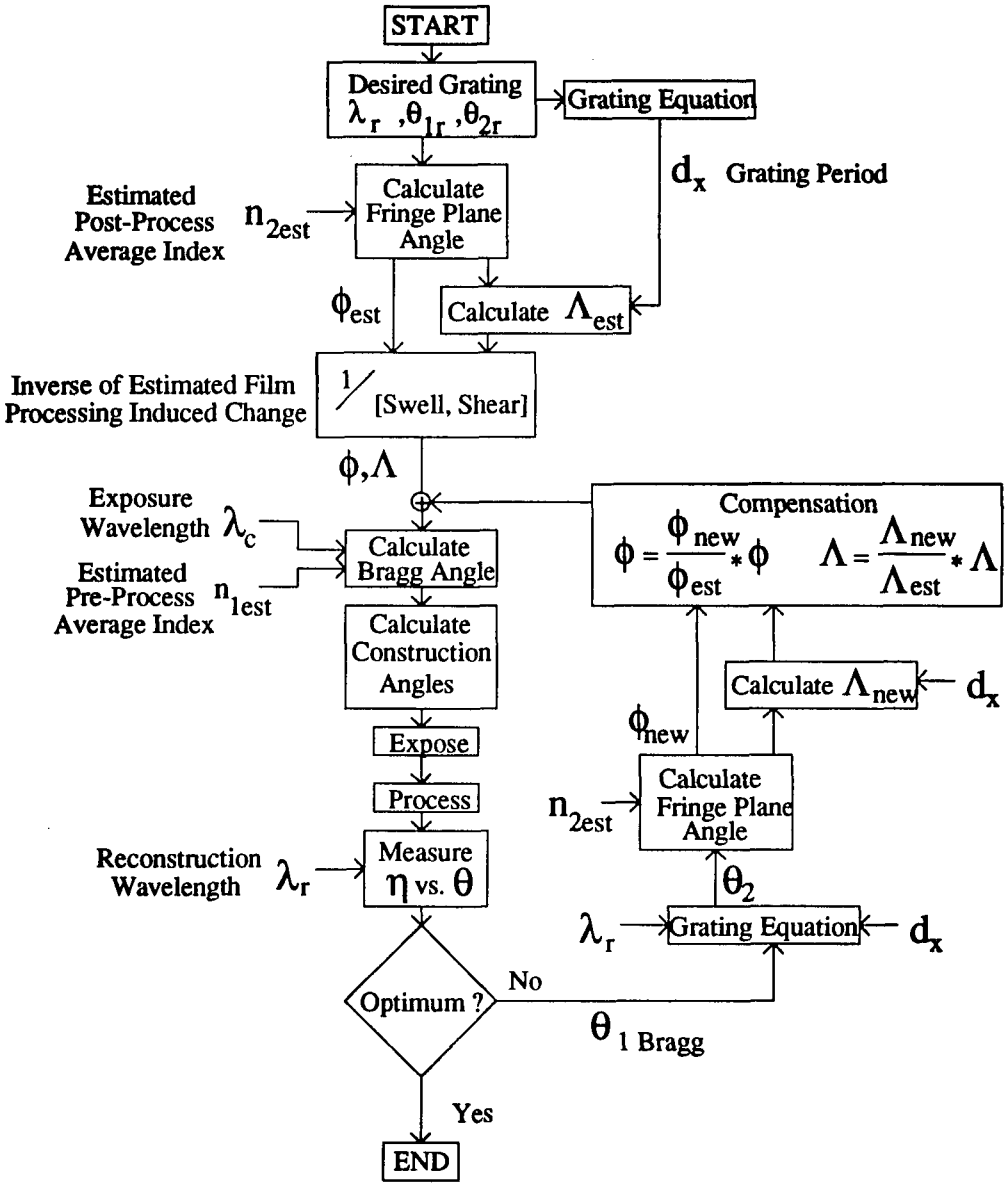

Figure 4.1 Holographic Element Optimization Process

plane angles desired in the final hologram are then calculated using an estimate of the final post-processed average index. Both the pre-process (exposure) and the post processed (final) average refractive indices are estimated based on accepted values[19] and the same values are used throughout the optimization process. The expected processing induced changes based on knowledge of the film parameters are inverted and applied to the calculated fringe plane spacing and fringe plane angle. The index during exposure and the exposure wavelength are then used to calculate appropriate construction angles and the hologram is exposed. After processing, the measured Bragg angle is used to recalculate new fringe plane angles and fringe plane spacing which are used as compensation factors for a new exposure. Better characterisation of the initial film parameters reduces the amount of effort required to produce optimized holographic elements.

Compensating Bragg angle shifts due to swelling typically requires adjustment to higher construction beam angles during exposure. This angle increase makes the fabrication of the highly slanted gratings used in the HOE Module more difficult to fabricate because of the angular limitations of the aperture masking method used.

4.2 HOE Module

The HOE Module design is presented in chapter 2 (figure 2.3). There are several steps in the fabrication of the module:

1. Epoxy unexposed DCG plate in aluminum frame
2. Expose and Process module assembly
3. Cement thin cover glass on film side
4. Cement Glass Spacer on film side using fixture

4.2.1 HOE Exposure Arrangement

The exposure arrangement for the HOE module is shown in figure 4.2. Two special exposure components were fabricated; the exposure mask figure 4.3 and the exposure stand fixture figure 4.4. The exposure mask permits sequential exposure of each hologram and provides accurate masking for the clear 1.5 mm center space on the receive side of the HOE module. The exposure mask and exposure stand are fabricated for correct masking at the beam angles used and to permit flipping the HOE module in the exposure stand as required to record all holograms.

Exposure Sequence

- Angles in the exposure arrangement are optimized using an iterative procedure.
- Mount exposure mask on the HOE module to be exposed.
- Mount HOE module with mask in exposure stand.
- Uncover multiplexed hologram area / expose / re-cover
- Uncover first single hologram area / expose / re-cover
- Flip HOE module
- Uncover multiplexed hologram area / expose / recover
- Uncover second single hologram area / expose
- Remove mask from HOE module and process.

4.2.2 Glass Spacer and Cover Glass Assembly

After developing and processing the HOE module the thin glass cover slip is cemented in place using UV cured cement (Norland 61). This cover slip completes the encapsulation of the DCG hologram film to prevent changes in the HOE characteristics due to environment.[22] The glass spacer is then cemented in place with the same UV

cure cement using the fixture shown in figure 4.5. The UV curing cement fills the small space left between the cover slip and the glass spacer. The UV source illuminates the back side of the DCG plate.

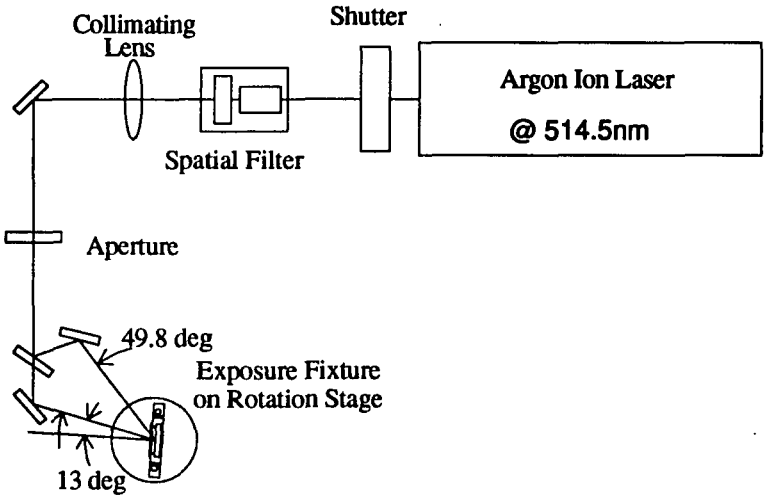

Figure 4.2 Exposure Arrangement

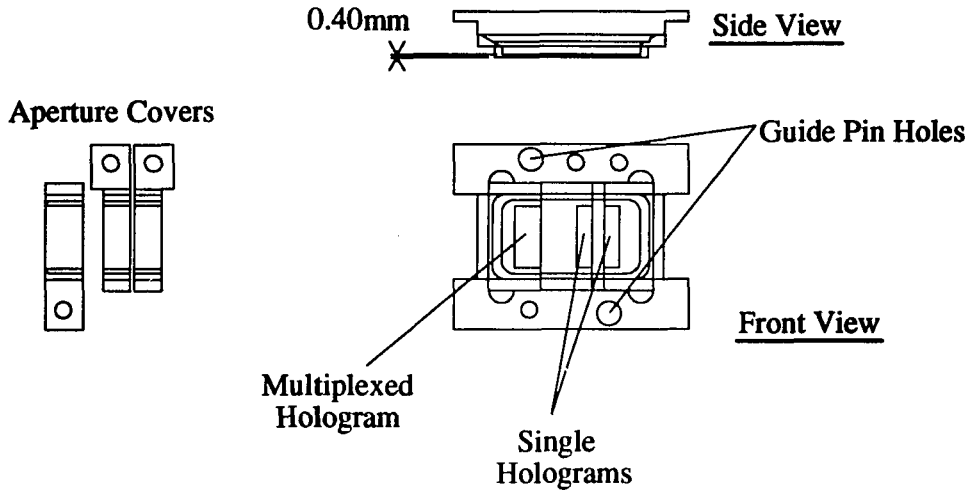

Figure 4.3 Exposure Mask

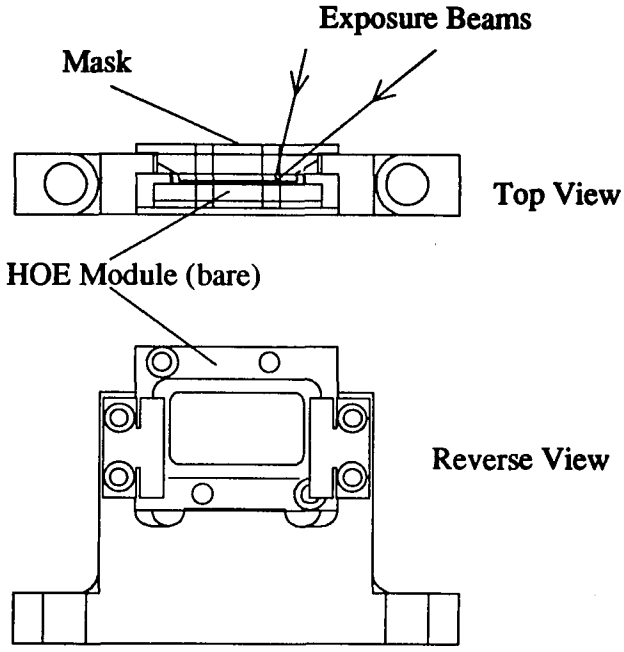

Figure 4.4 Exposure Stand

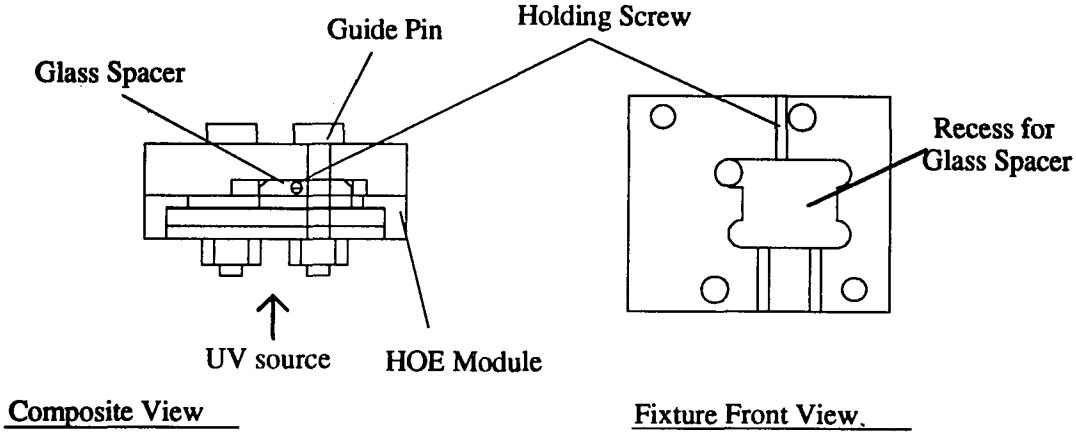

Figure 4.5 Glass Spacer Assembly Fixture

4.3 HOE Module Grating Measurements

Diffraction efficiency vs. angle measurements were made for the single and multiplexed gratings on the HOE Modules prior to mounting the cover glass. Measurements were made using an E/O Module source with the sign conventions shown in figures 4.6 and 4.9. The diffraction efficiencies in all the plots are compensated for fresnel reflection from the substrate glass (near normal) and for reflection from the front hologram/air interface (high angle incidence).

The large residual Bragg shift of 2 degrees was the result of a mistake in selection of a plate for optimization prior to exposure. The plate was mistakenly chosen from a different batch than the plates used in the modules. This small mistake and the resulting Bragg shift is useful, however, to demonstrate properties of the holograms and the exposure process. Many prior exposures were made to demonstrate the validity of the optimization procedure previously discussed.

4.3.1 Single Grating Measurements

Diffraction efficiency plots from the outside and inside single gratings are shown in figure 4.7 and 4.8. The designation of the gratings as inside and outside refers to their relationship to the edge of the HOE Module (reference figure 2.3). Only two of the inside grating plots are shown for clarity in comparing the curve fit lines from the model to the actual data and the range limitation on the outside gratings was due to mechanical constraints. The sign convention on the input beam angle was chosen to make comparison of the inside and outside grating consistent with their exposure condition and fringe plane angles. The single gratings are curve fit using the single grating coupled wave model presented in chapter 3 and the resulting parameters are given in table4.1.

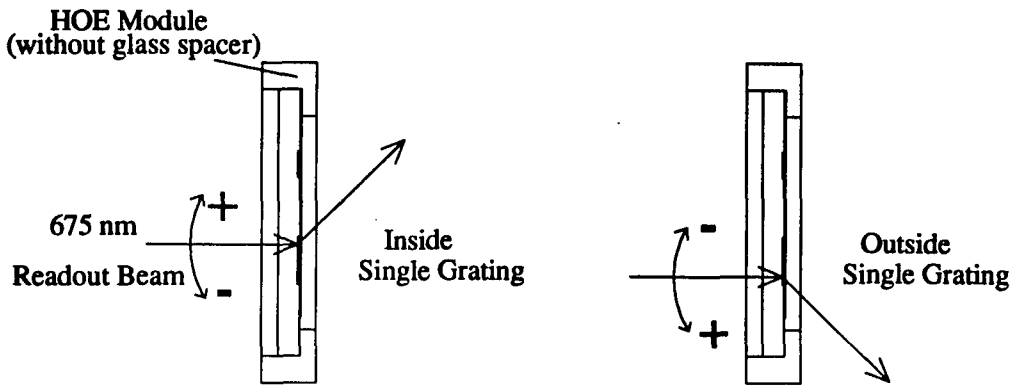

Figure 4.6 Inside and Outside Single Grating Readout Geometry

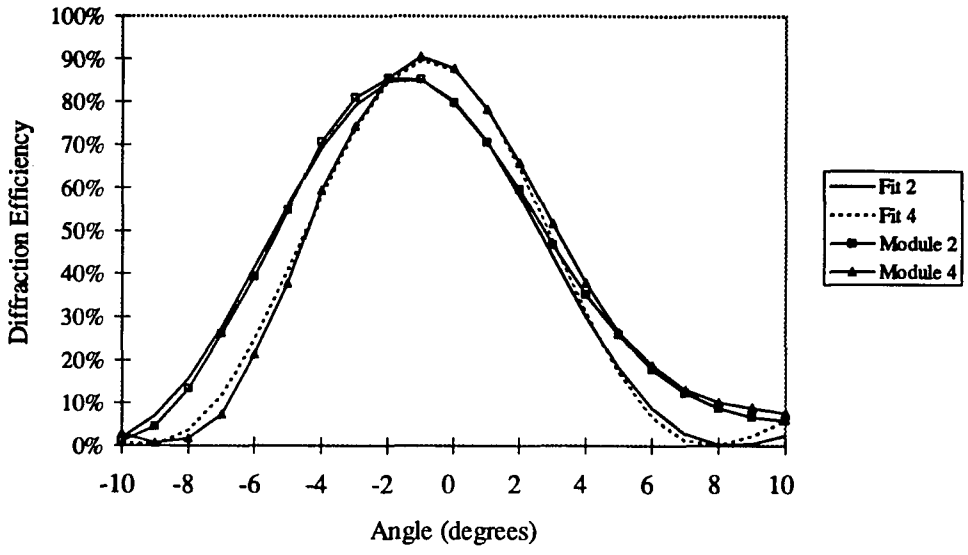

Figure 4.7 Inside Single Grating Curve Fit

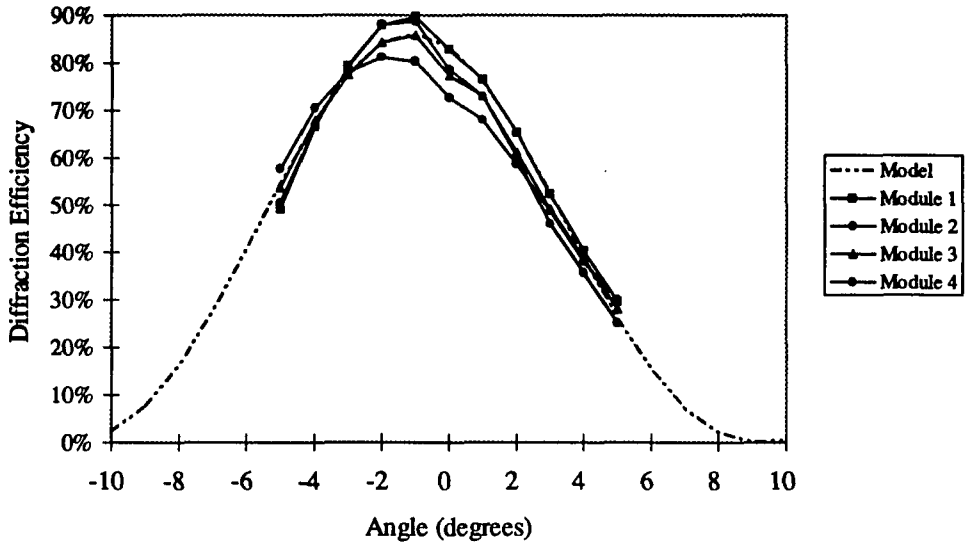

Figure 4.8 Outside Single Grating Curve Fit

Table 4.1 Single Grating Curve Fit Parameters

Recording index = 1.58	Post-process index = 1.46		
	Model Final Thickness (microns)	Swelling Factor	Model Index Modulation
Module 1 Inside Grating	6.1	1.2	.04
Module 2 Inside Grating	6.1	1.2	.04
Module 3 Inside Grating	6.7	1.27	.038
Module 4 Inside Grating	6.6	1.25	.038
Outside Gratings	5.7	1.22	.055

These model thickness measurements can be compared to a pre-process thickness of 8.1 μm. The post-process thickness (not measured) is probably on the order of 8.9 μm based on the test measurements presented in the humidity cure data. This demonstrates the discrepancy between measured thickness and effective thickness discussed in the previous chapter.

4.3.2 Multiplexed Grating Measurements

Data from all four multiplexed gratings (compensated for fresnel reflection) are shown in figures 4.11, 4.12, 4.13, and 4.14. It is evident that there is a large amount of variation in diffraction efficiency for each beam. This can be traced primarily to large (10 to 15%) beam power fluctuations (coupled with short exposure time) in the Argon Ion laser used for these exposures. Exposures for the humidity cure experiments were made with a more stable laser and more consistent results were achieved.

All the multiplexed gratings are curve fit using the multiple coupled wave model presented in chapter 3. The curve for an ideal multiplexed grating is given in figure 4.10. For this ideal case all Bragg angles are aligned with the ideal input angle at 0 deg. and the off-axis beams are stronger than the zero order to overcome the larger fresnel reflection they will experience along the off-axis beam paths. Module 4 measurements (figure 4.11) were made over a large angle and the same "tail" seen in the single gratings is seen on both the off -axis beams.

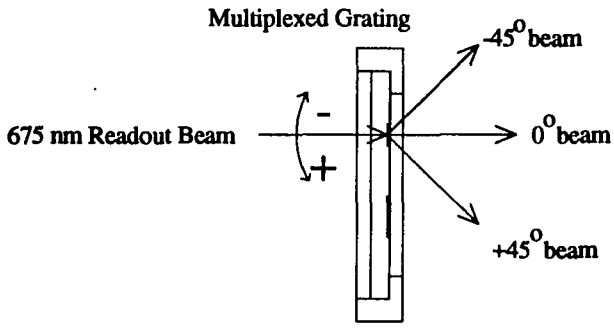

Figure 4.9 Multiplexed Grating Readout Geometry

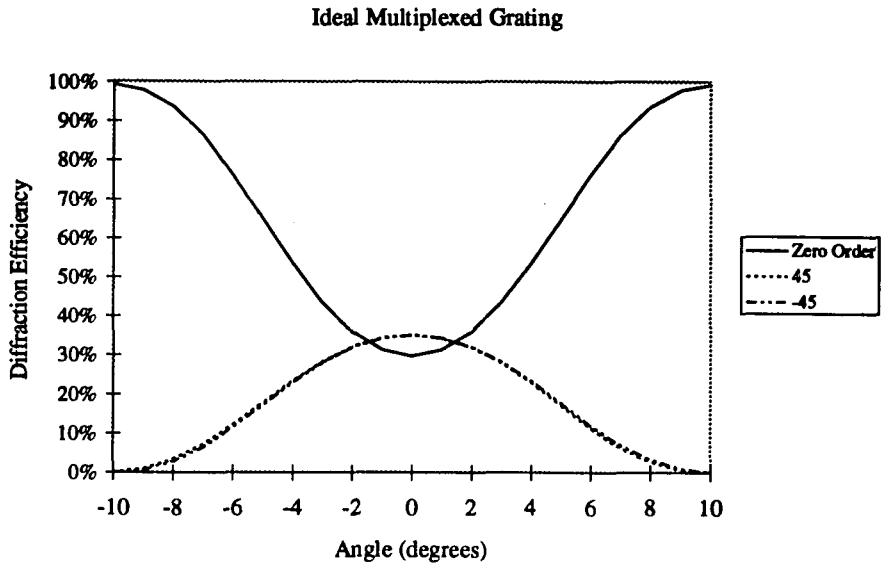

Figure 4.10 Ideal Multiplexed HOE Module Characteristic

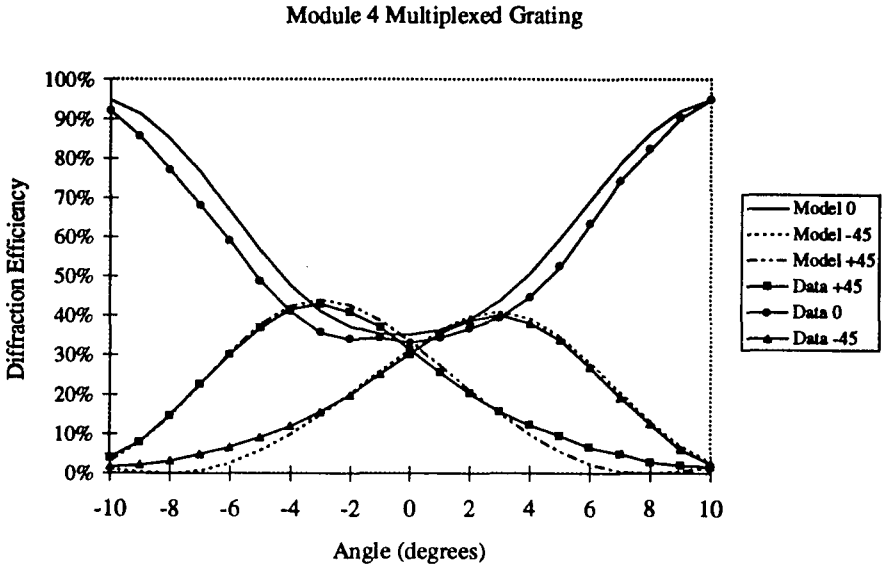

Figure 4.11 HOE Module 4 - Full width Mesurement

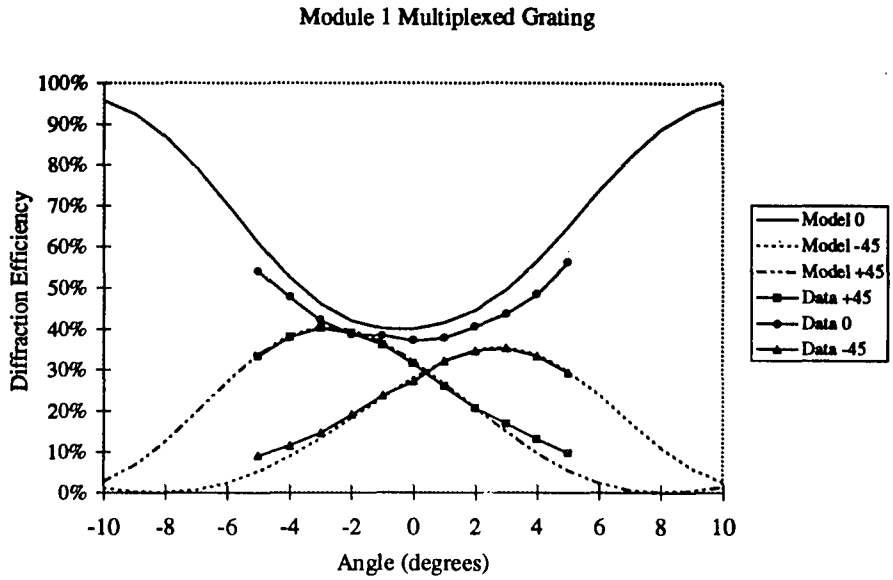

Figures 4.12 HOE Module 1 - Measured Data and Curve Fit

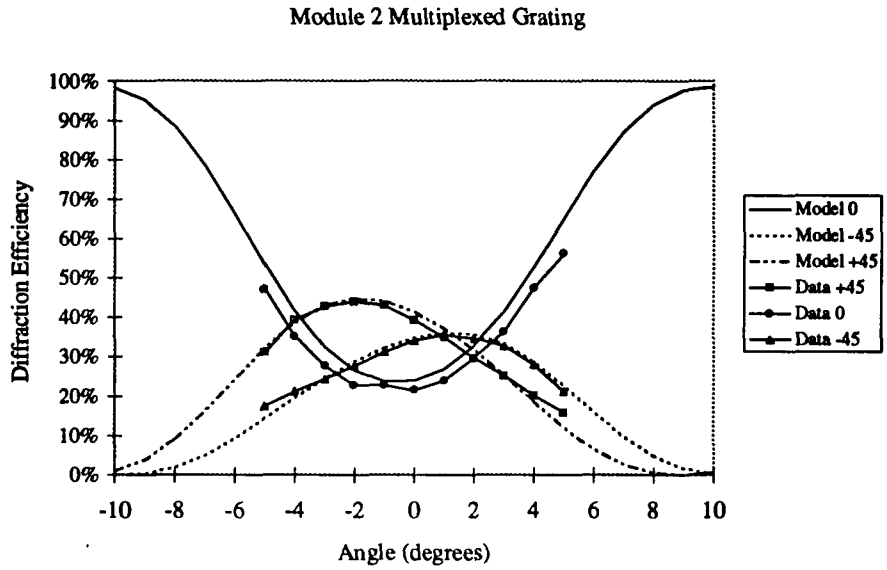

Figures 4.13 HOE Module 2 - Measured Data and Curve Fit

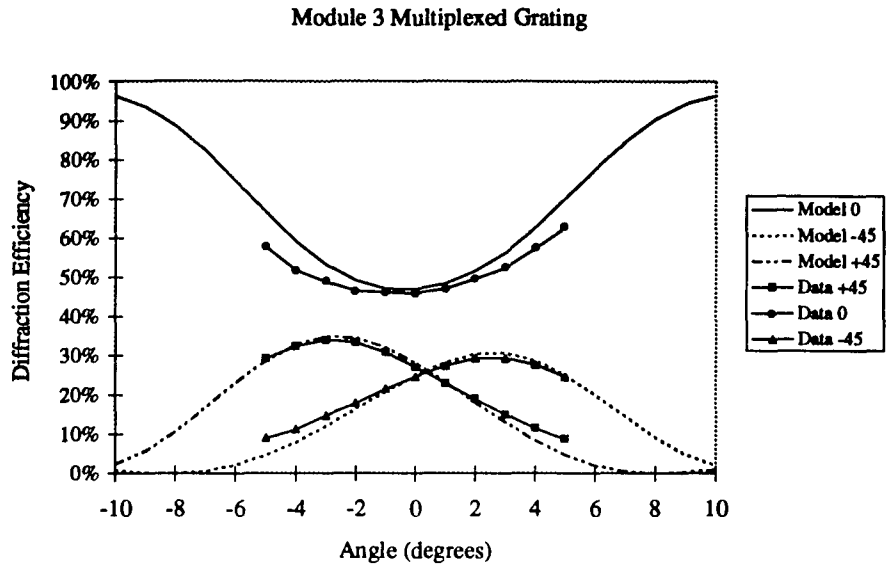

Figures 4.14 HOE Module 3 - Measured Data and Curve Fit

Table 4.2 Multiplexed Grating Curve Fit Parameters

Module	Beam	Input Bragg Angle	Model Index Modulation	Model Film Thickness	Average Index
1	-45	2.2	.0219	6.8	1.47
	+45	-2.3	.0228	"	"
2	-45	2.15	.02	"	"
	+45	-2.2	.0215	"	"
3	-45	0.6	.0215	"	"
	+45	-1.3	.024	"	"
4	-45	2.1	.0182	"	"
	+45	-2.2	.0195	"	"
Ideal	+/-45	0	.0208	"	"

The curve fit parameters are interesting in two respects. First the model index modulation is .021 +/- 15% approximately and this roughly corresponds to twice the power fluctuations in the laser output power. When the efficiency variations in the multiplexed gratings are compared to the single gratings, it is evident that consistency in

the diffraction efficiency of the multiplexed elements requires much greater control over exposure energy. The second interesting result is the consistency of the Bragg shift between the multiplexed grating and the single gratings. This demonstrates that the Bragg shifts are not caused by any anisotropic lateral film stress and that the magnitude of the Bragg shift is not modified by the existence of two gratings in the same volume.

The previously mentioned "tail" or deviation of the actual diffraction efficiency curves from the model curves is a possible indicator of fringe bending[23]. One interesting aspect of this is that the tail is identical for both sides of the multiplexed grating +/- 45 degree beams. This would indicate that the fringe bending is not due to the release of lateral stress as suggested in reference [23]. Figure 4.15 shows the effect of lateral stress on fringe bending vs. the effect of non-uniform swelling of the emulsion.

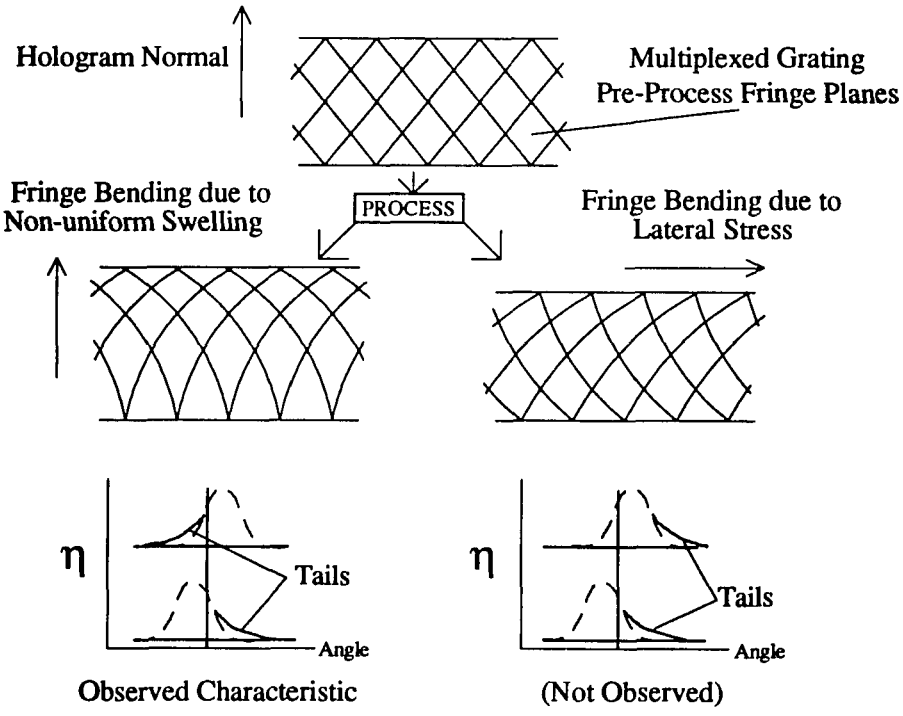

Figure 4.15 Fringe Bending Characteristics for Multiplexed Gratings

Chapter 5
Electro-Optics and Electronics

Electronic and electro-optic components selected for the implementation of one channel in the connection cube structure were limited to common commercially available components. Although more emphasis is placed on design and development of the holographic elements and the optical pathway, it is also important to demonstrate high speed data transfer through the system which is the primary function of the free space interconnect system.

5.1 Laser Diode Characterization

The 670nm laser diodes selected for the system (Toshiba TOLD 9211) are index guided InGaAlP devices designed for applications such as bar code scanners, laser printers, and measurement systems. Index guided laser diodes exhibit very little astigmatism as compared to gain guided devices and this is important for collimated beam applications using simple optics[24]. The choice of a visible laser diode instead of an infrared laser diode provides two advantages for the prototype system: first, the smaller construction / reconstruction wavelength difference reduces exposure angles; and second, system alignment and demonstration are simplified.

The consistency of the operating characteristics of the laser diodes selected for the prototype system is important. The laser diodes were screened for operating wavelength in the drive current region of interest (32mA to 45mA) and the four laser diodes closest to 675nm were selected.

Table 5.1 Measured Laser Diode Wavelengths from Available Diodes.

Laser Diode #	Wavelength @ 42mA	E/O Module
1	674.6	1
3	674.3	3
4	675.7	4
5	676.5	
6	677.0	
7	676.3	2
8	676.8	

*LD #2 was burned out

The output optical power vs. input current was measured for the four selected diodes in order to determine optimum modulation and bias current (figure 5.1). The diodes are consistent in this operating characteristic.

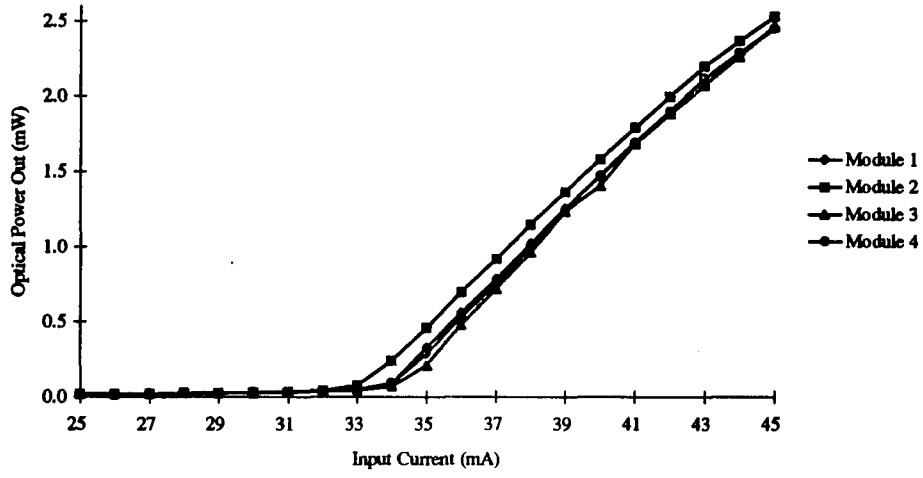

Figure 5.1 Laser Diode Optical Power Output vs. Input Current

A low frequency model of a laser diode is shown in figure 5.2. The voltage across the ideal diode is related to the band gap in the semiconductor which also determines the

wavelength of the device. The relationship between the ideal diode band gap energy (in eV) and the wavelength is the familiar equation: [eqn 5.1] $E = hc/\lambda$ or $E = 1242(eV \cdot nm)/\lambda(nm)$.[25] When the band gap energy is converted to potential voltage this relationship predicts an ideal diode voltage of 1.84V for 675nm wavelength. The plot of device voltage vs. input current shown in figure 5.2 also indicates that the series resistance in the model diode should be 16 ohms. The plot shows the diode model is very consistent with real diode behavior.

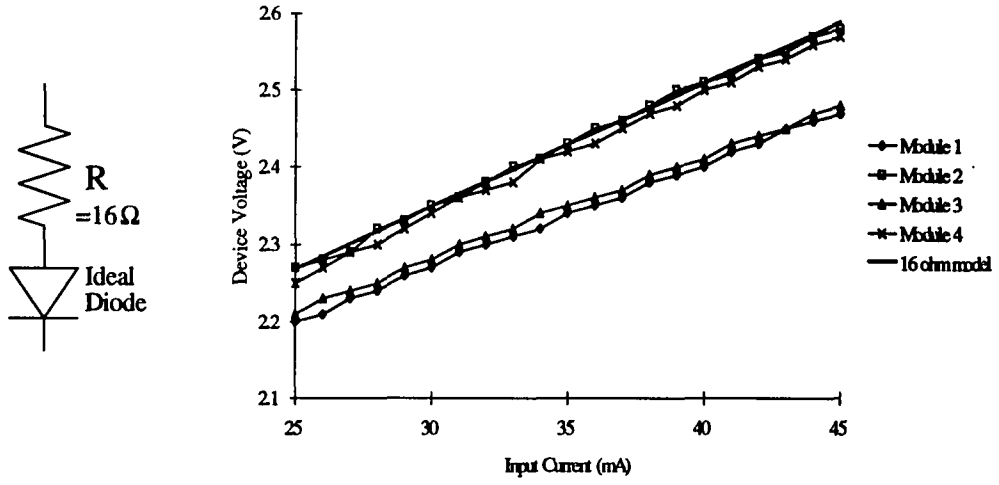

Figure 5.2 Low Frequency Laser Diode Model and Device Voltage vs. Current

The physical beam parameters of the laser diode are shown with the laser diode package in figure 5.3a. The elliptical beam has a polarization oriented along the short axis of the ellipse. The polarization ratio at 2 mW is about 200:1. The beam power vs. angle of a typical laser diode was measured and is shown in figure 5.3b. Residual astigmatism for the index guided device is small and it is possible to produce highly collimated beams using a simple aspheric lens.

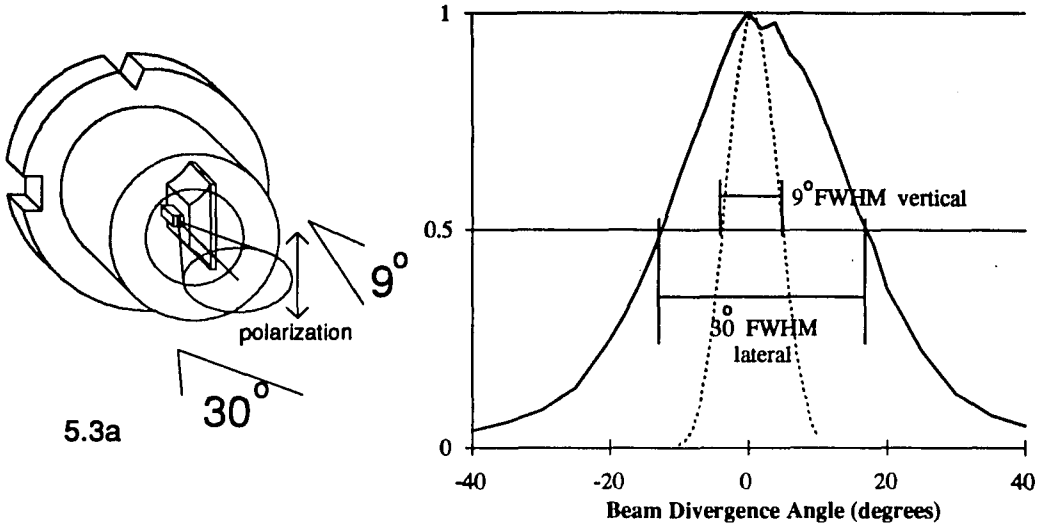

Figure 5.3 a,b TOLD 9211 Package w/ Polarization, Beam Orientation, and Divergence

The laser diodes are ideally single mode with dc current input. Typical dc drive current behavior of the laser diode spectrum over the current range of interest was measured using a scanning monochrometer (Jarrell Ash model 82020). This monochrometer has 0.015 nm resolution and is calibrated to 0.02nm wavelength accuracy for the wavelength range from 301.9 nm to 579.1 nm (mercury lines) and at 632.8nm (HeNe). The spectrum from module 3 is shown in figure 5.4. The broad spectrum near threshold is shown in the plot with 36 ma drive current. Mode hopping is also demonstrated between the 39ma and 42ma plots.

The behavior of laser diodes with modulation is a result of transient conditions existing in the laser diode[26]. Suppression of longitudinal side modes is not complete during modulation, and as the modulation speed increases, the laser no longer emits in a single mode. The laser diode in E/O Module 4 was modulated with a high frequency square wave input to the laser driver circuit (see section 5.2) and this caused the spectral broadening displayed in figure 5.5.

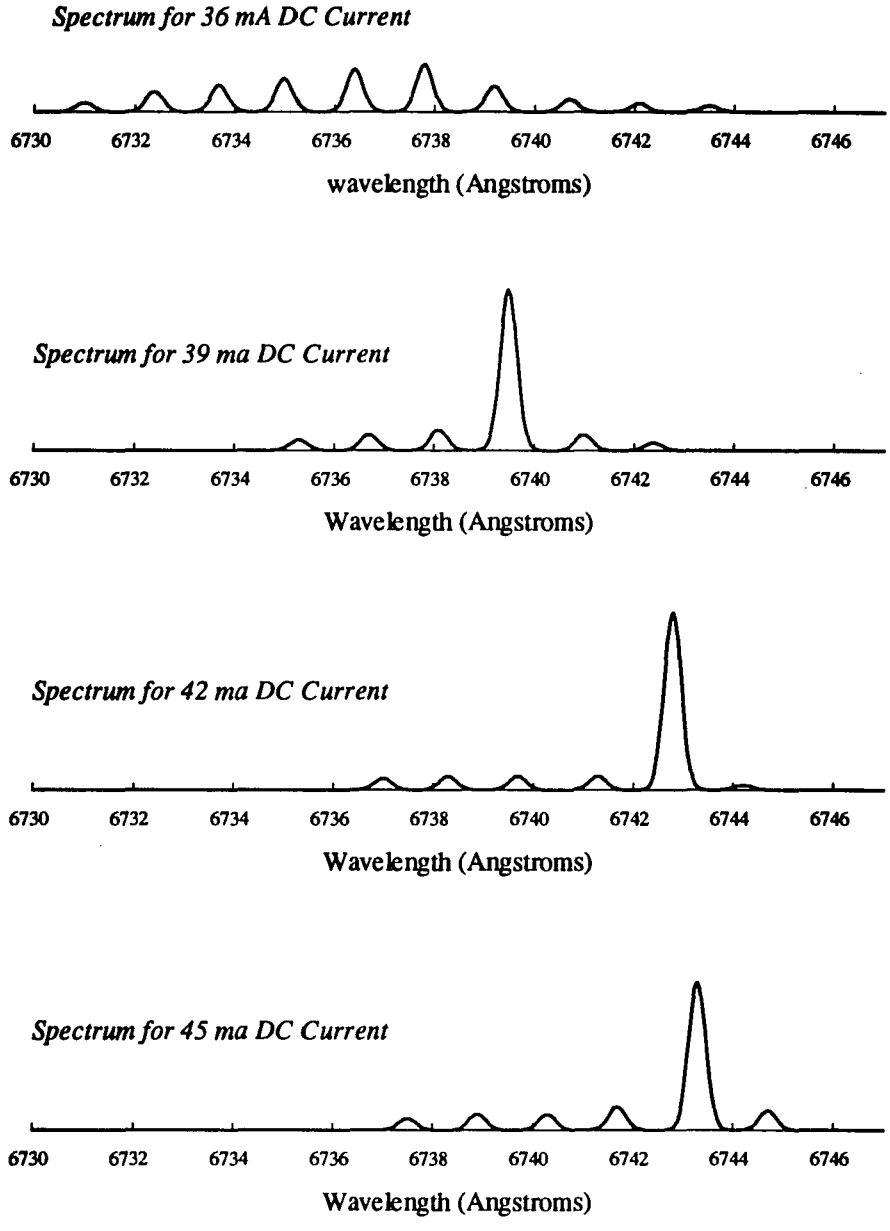

Figure 5.4 DC Current Laser Diode Spectra (E/O Module 3)

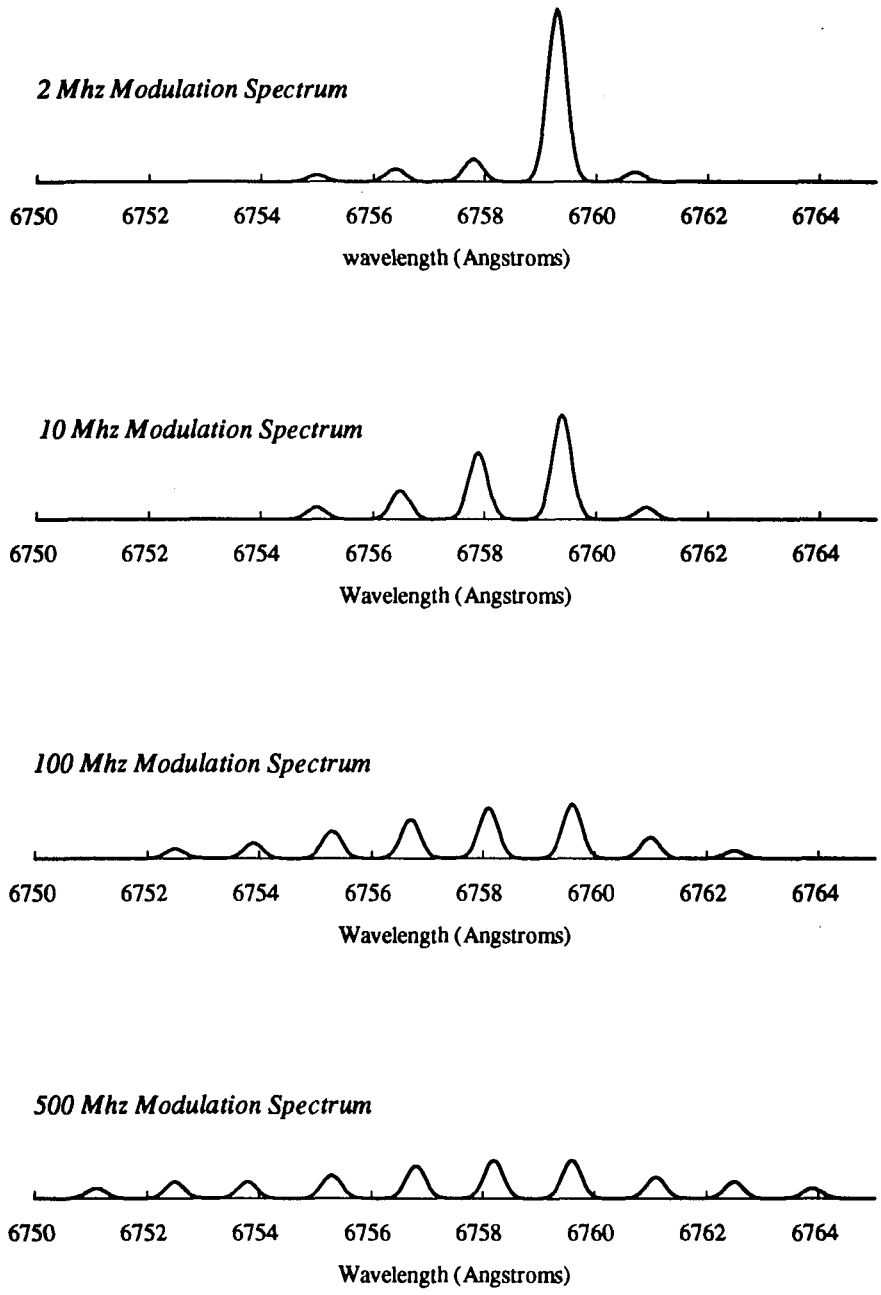

Figure 5.5 Laser Diode Spectrum with Modulation (E/O Module 4)

5.2 Laser Driver Electronics

Sony laser driver circuit CXB1108AQ was used for the transmitter electronics. This bipolar silicon integrated circuit is designed for high speed (2.0 Gbps NRZ) with ECL compatible inputs. The circuit and PC board are shown in figures 5.6 and 5.7.

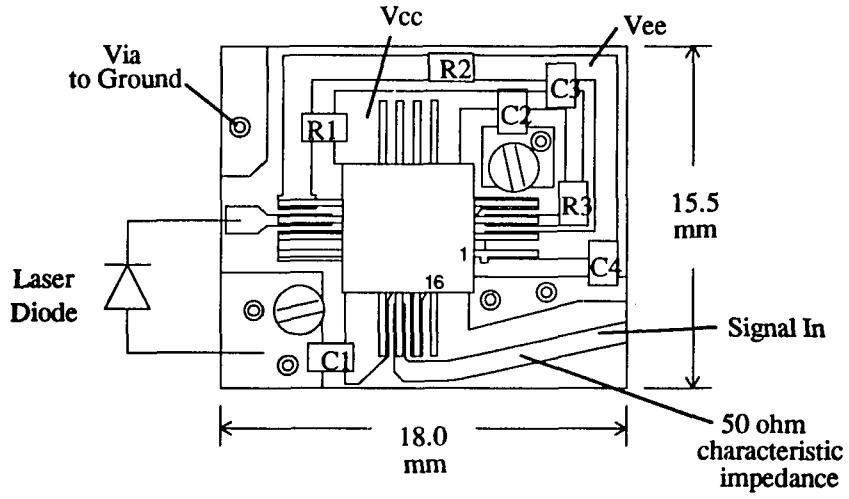

Figure 5.6 Laser Driver Electronics PC Board

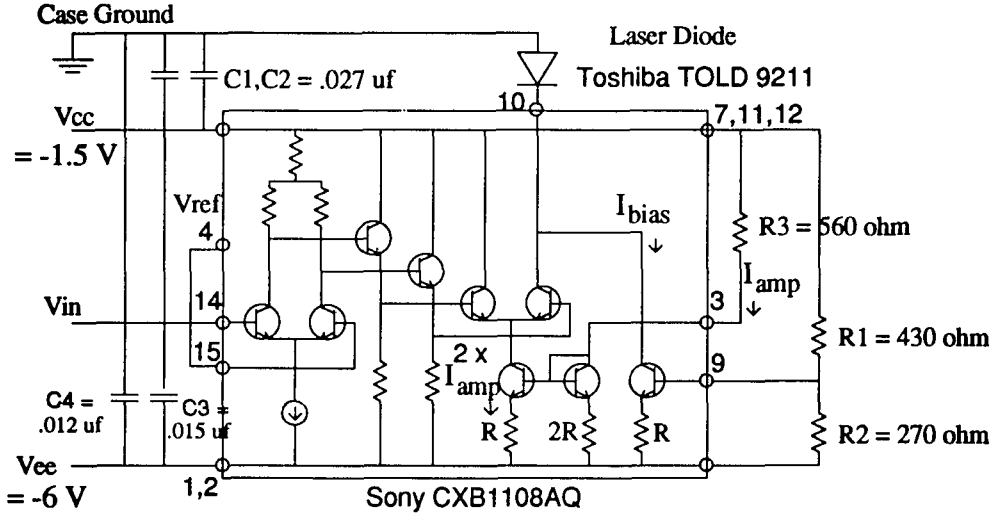

Figure 5.7 Laser Driver Electronics Schematic

A major modification to the intended operation of the circuit was required in order to provide the high operating voltage to the visible laser diode. The most positive voltage to the circuit (Vcc) is set to -1.5 V below the laser diode anode and the negative voltage (Vee) is at -6 V. This was required to use the laser driver which was designed for longer wavelength laser diodes having lower operating voltage. Although final operation of the circuit was satisfactory, the floating of the laser driver circuitry introduces noise through power supply fluctuations and does not allow good grounding. Signal ground is provided through capacitors C1, C2.

The single ended input to the input differential amplifier stage is created by connecting the second input (pin 15) to a reference voltage (pin 4). A bias current keeps the laser diode at the knee of the input current vs. optical power out curve (figure 5.1) and this bias current is labset by two resistors (R1, R2) which provide a voltage level at pin 9 . The amplitude of the modulated signal current from the output differential amplifier stage is set by resistor R3 which feeds current to a 2 to 1 current source supplying the output amplifier stage. Modulation current amplitude is twice the current in labset resistor R3.

5.2.1. Laser Driver Lab-set

Actual implementation of a system using similar laser driver circuits is simpler and cheaper if little or no lab setting and tweaking is required to produce correct bias and modulation currents for a mating laser diode. A test circuit board was assembled and mated to two dummy loads to select bias and modulation current labset resistor values. One dummy load (71 ohm) was selected to produce the operating resistance of a typical TOLD 9211 laser diode near the knee of the optical power vs. current curve while a second dummy load of 57 ohm was used simulate operation at 45 mA. Potentiometers in the place of R1 and R3 were used to set the bias current to 33 mA and the modulation

current to 44mA. Resistor values in the range of 430 (+/-3% measured) were used for R1 in the four module boards and available resistors in the range of 560 were used for R3. The resistor values resulted in a peak modulation current of almost 45mA and a bias current near 33mA. After mating three of the laser driver boards to laser diodes, optical power output with and with/out modulation was measured and is shown in table 5.2. The data shows consistency between modules without the need for individual labset. The higher output under modulation for module 2 is consistent with the optical power vs. input current curve in figure 5.1.

Table 5.2 Optical Power Output with and without Signal Input.

Module	No Modulation	Modulation (10 Mhz)
1	30 μW	1290 μW
2	48 μW	1420 μW
4	31 μW	1290 μW

*Module 3 was not connected to provide a raw E/O Module for test purposes.

Measurement of the average output optical power of one module over the full modulation frequency range (figure 5.8) indicates no clear drop off in frequency and possibly some gain peaking[25]. This implies that the source is not bandwidth limited over the modulation range that can be provided by the available signal source (HP 8131A 500Mhz Pulse Generator)

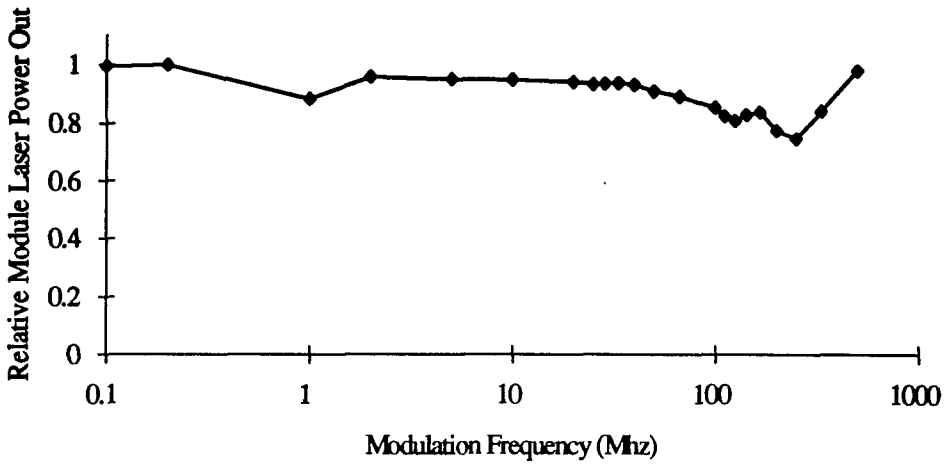

Figure 5.8 Laser Diode Optical Power Out vs Modulation Frequency (E/O Module 4)

5.3 Detector Characteristics

The detector used is a PIN diode (UDT PIN-HS008) designed for high speed operation. The quoted 1pf capacitance of this detector is on the margin for high speed operation with the transimpedance amplifier used. The real lateral extent of the detectors can be found from the data taken during alignment and potting of the detectors (see chapter 2). The data indicates detector diameters of between 160 and 180 micron as compared to the 200 micron diameter given in the detector data sheet.

The measured dc responsivity of one sample detector is 0.42 μA/μW using an HP8152A Optical Average Power Meter as the reference.

5.4 Transimpedance Amplifier

The receive electronics was limited to a transimpedance amplifier (HP ITA - 06318). The circuit implementation and PC board configuration are given in figure 5.10. This transimpedance amplifier is designed for typical data rates of 1.5 Gb/s NRZ.

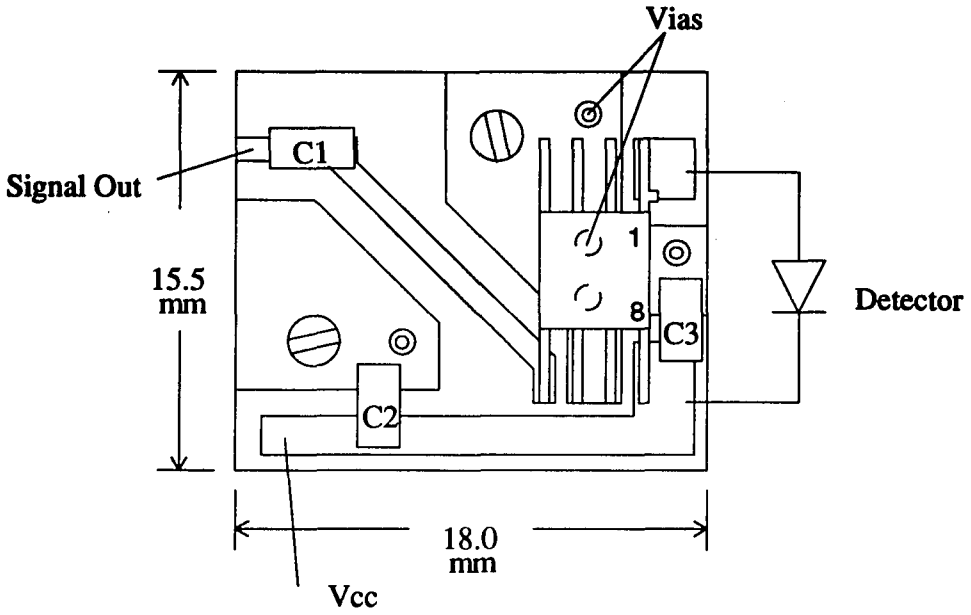

Figure 5.9 Detector Electronics PC Board

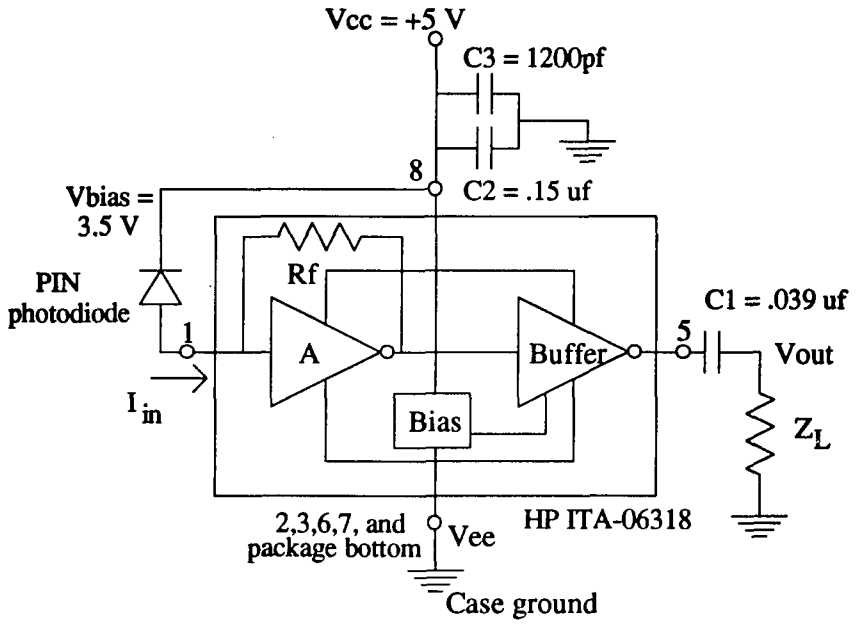

Figure 5.10 Detector Electronics Schematic

The transimpedance amplifier is a good choice for short distance interconnects that require wide bandwidth and high dynamic range and are not sensitivity limited (low detected optical power)[27]. The HP ITA-06318 is a fully packaged transimpedance amplifier with a transimpedance gain in the range of 2200 to 2800 ohms (flat to 1 GHz). The input current limit for no distortion on this amplifier is 450 μA. The modulation current in the laser driver circuit was set to keep the received optical power just below this threshold for three-way split beams.

5.5 Printed Circuit Board Design and Fabrication

The packaged dimensions of the printed circuit and electronics are less than 1/6 wavelength for the highest design electrical frequency of 500 MHz and thus can be viewed as a lumped circuit, however, trace widths on the input and output signal lines were made to produce 50 ohm characteristic impedance. The PC Boards were fabricated from RT/duroid 6006 microwave laminates (Roger Corp., Chandler, AZ). The 6006 laminate is a ceramic-PTFE composite with a uniform dielectric constant for the fabrication of precisely impedance matched microwave and electronic circuits. The trace width for a 50 ohm characteristic impedance line at 500 Mhz is taken from tables calculated by the company using measured laminate characteristics. The laminate used is a 0.64 mm (.025 inch) thick dielectric with 0.034 mm (1.34 mil) thick copper foil and an effective dielectric constant of 4.307 yielding a 50 ohm trace width of 0.90 mm (0.0355 mil).

The PC board patterns were made on 35 mm high constrast black and white negatives (Agfa Ortho). The negatives were produced by photographically scaling the image of a 10 to 1 pattern using a 35mm camera. The PC laminates were coated with standard photoresist and exposed to UV through the negative film patterns. The developed laminates were then etched with ferric chloride and the resulting printed circuit

board was tinned in a tin salt solution. Ground vias were formed by insertion of copper eyelets (manufactured by International Eyelets, Inc.) in drilled thru-holes.

5.6 Electromagnetic Interference (EMI) Filter

The power supply leads for both the transmit and receive electronics were carried into the electronics enclosure via low pass EMI filters in order to elminate any high frequency power supply noise. The filters are characterised by 20 dB loss at 10 Mhz and 70 dB at 1 Ghz. The filters use a capacitive path to ground to filter out unwanted high frequency components and thus do not introduce a large amount of inductance in the power supply path.

5.7 Output Signal and System Bandwidth

Single pole roll-off in the receiver output voltage is seen in figure 5.12. Since no rolloff was seen in the power of the transmit beam, it is likely that the primary source for the system bandwidth limit is in the receiver. A simplified high frequency model for the detector and transimpedance amplifier is shown in figure 5.11[27]. In this model, the most likely limiting factor is the junction capacitance of the PIN detector (C_{in}).

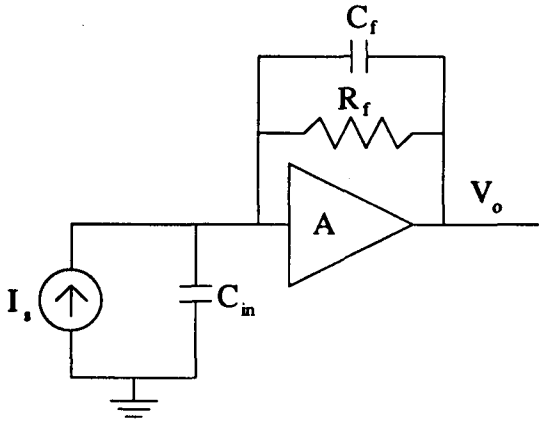

Figure 5.11 Transimpedance electrical model

For $C_{in} >> C_f$ and $A >> 1$ the transfer equation for this circuit is given by:

[eqn 5.3]
$$\frac{V_o(\omega)}{I_s} = \frac{R_f}{1 + j\omega R_f\left(C_f + {}^{C_{in}}\!/_{A}\right)}$$

C_f, C_{in}, and A are not directly known, but a curve fit to the receiver output voltage vs. frequency using a R_f value of 2500 yields $(C_f + C_{in}/A) = 0.2$ pf. The system bandwidth can be calculated from $f_{3dB} = {}^{1}\!/_{2\pi R_f(C_f + C_{in}/A)}$ =320Mhz. For NRZ data transmission this bandwidth provides data rates up to 2 x f_{3dB} = 640 Mb/s.[28]

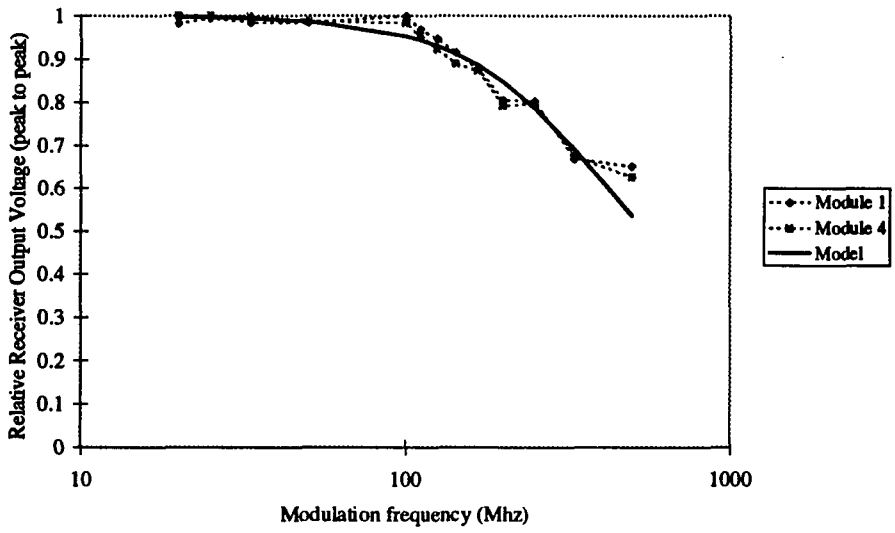

Figure 5.12 System Response - Receiver Output vs. Modulation Frequency

Two receiver output signals from modules 1 and 4 are shown in figure 5.11. The input to the system is a 500 Mhz modulated signal to module 2. The low noise received waveforms show the uniformity of the signals from two separate modules. The small

amount of signal skew is mostly due to differences in the output cabling and measurement channels as discussed in section 5.6.

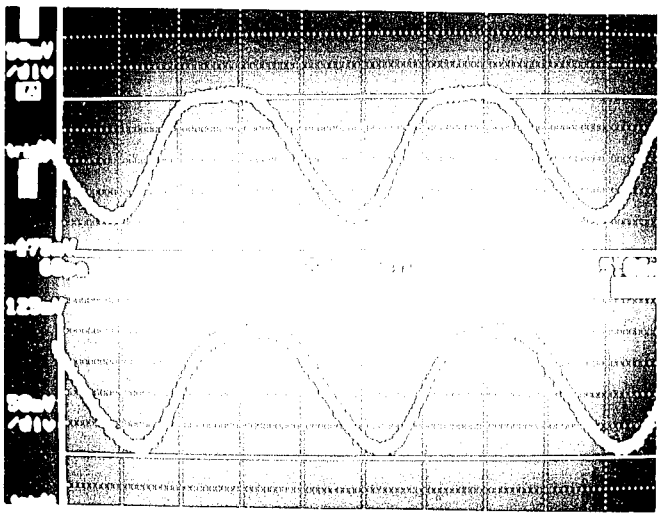

Figure 5.13 E/O Module 1 and 4 Receiver Output w/ 500 Mhz Signal from Module 2.

5.8 Signal Skew Measurements

Measurements were made of signal skew in each signal path using one transmitter module (E/O Module 2) and two receiver modules (E/O Modules 1 and 4). Twelve measurements were made using the test setup shown in figure 5.14. Each combination of cabling, module, and beam path was measured in order to separate signal skews contributed by the cables and oscilloscope from relative signal skew between the receive electronics in the two modules and the signal skew in each beam path. The resulting measured beam path skews and the difference between the electronic propagation delays in the receiver E/O Modules are given in Table 5.3 and compared to calculated propagation delay differences based on connection cube geometry.

Table 5.3 Skew Measurements

Skew source	Measured Skew	Calculated
E/O Module 1 delay - E/O Module 4 delay	31 ps	0 ps
Through Beam delay - Short Leg delay	84 ps	53 ps
Long Leg delay - Short Leg delay	34 ps	42 ps
Through Beam delay -Long Leg delay	49 ps	11 ps
Measurement Channel Skew	244 ps	

It is evident from the measurements that the skew due to the cables and measuring instruments (244 ps) was large relative to the inherent skews and introduced large error into the measurement. An important result is that the differential skew in the electronics (E/O Module 1 - E/O Module 4 = 31 ps) is small and on the same order as the inherent channel skew due to propagation delay.

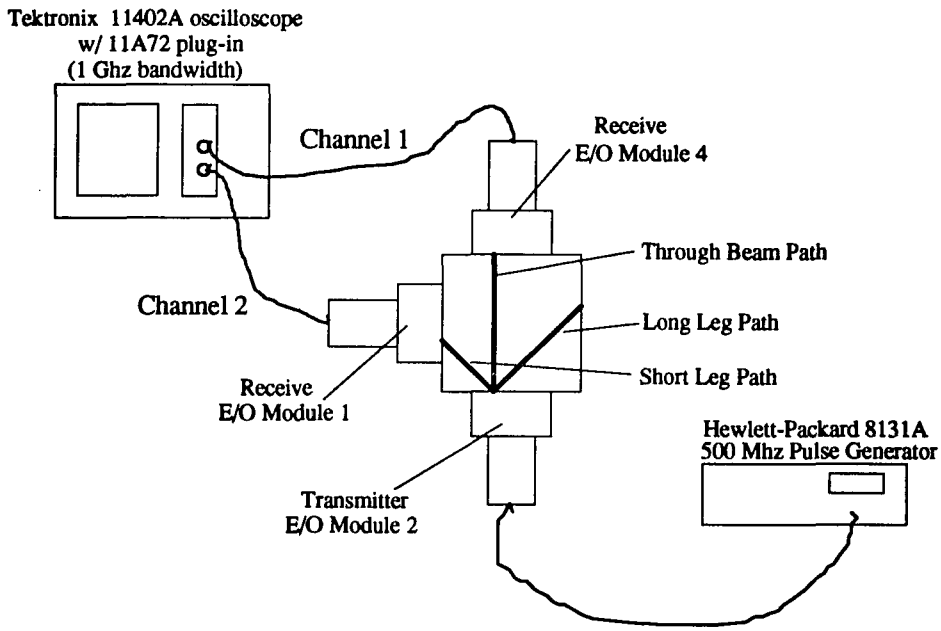

Figure 5.14 Skew Measurement Test

Chapter 6
Alignment Analysis

Evaluation of the optical performance of the connection cube system requires the analysis of fabrication tolerances, material properties, and electro-optic device effects. This analysis is assisted by the use of an optical design program (ZEMAX). Models of the optical beam paths are reproduced in the optical design program and the effect of specific variations that represent alignment errors, etc. are introduced. To simplify the analysis, some fabrication errors and variations with identical effects on the optical beam are collected and considered as a single variable.

6.1 Mechanical Alignment Analysis

The contribution of fabrication error to misalignment must begin by estimation of fabrication error in each component. An error budget can then be computed and used with ZEMAX to estimate optical performance. Misalignments will be analyzed primarily in the horizontal plane because this is the direction most affected by misalignment, electro-optic effects, and off-axis lens effects. Vertical misalignments are shown to be small by comparison.

6.1.1 Machining Errors

The fundamental limit on fabrication error is set by errors in the machining equipment and the limits of the measurement tools and techniques. The resolution of the machining equipment used (mill and lathe) is 0.01 mm while the measurement instruments have a minimum resolution of 0.0025 mm. The estimated best accuracy based on

experience with these tools is +/-0.010mm to +/-0.015 mm. The real accuracy in production of various components is dependent on the particular method of fabrication and measurement for that component and is estimated in the following analysis.

6.1.1.1 Connection Cube Tower.

There are many important considerations for fabrication errors in the tower (figure 6.1): the lateral and vertical location of the HOE module edge reference, the cube face location, the HOE module face reference, and the angle error in the cube face. All linear measurements were made with precision micrometers while the cube face right angle was checked with both a machinist's square and an angle plate. The cube width in both directions was carefully matched to within +/-0.01mm and the HOE module face reference is within +/-0.01mm measured face to face. The HOE module edge references measured relative to the cube face are accurate to within +/-0.015mm. The cube face angles are within approximately (0.02mm/35mm) radian or +/-0.033 degree.

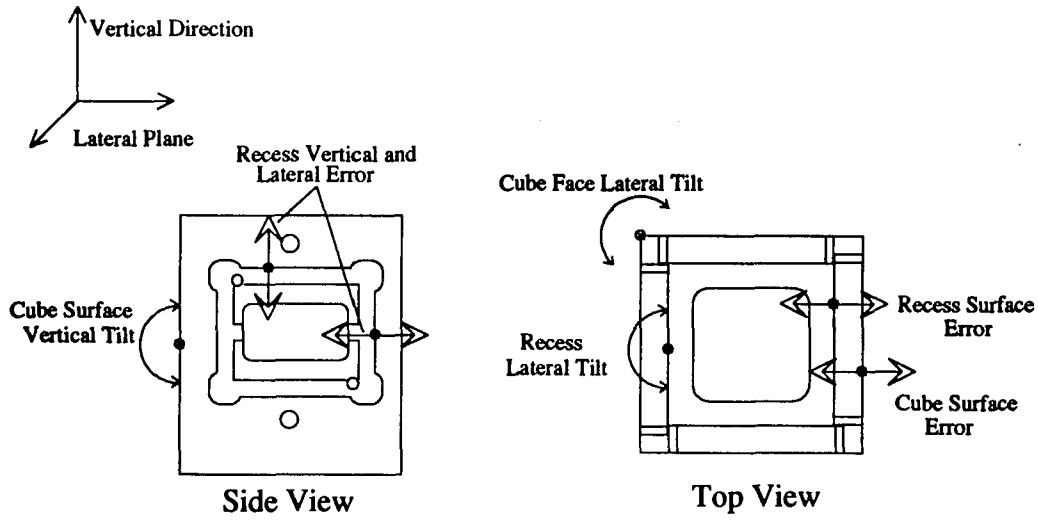

Figure 6.1. Connection Cube Tower Error Analysis

6.1.1.2 HOE module

The distance from the front plane of the DCG plate to the HOE Module face was carefully controlled to about +/-0.015 mm. The error in the guide pin locations relative to the edges is approximately +/-0.02 mm. The cumulative error in the location of the hologram edges as defined by the exposure mask, which also use the guide pins as a locating reference, is estimated at +/-0.03mm.

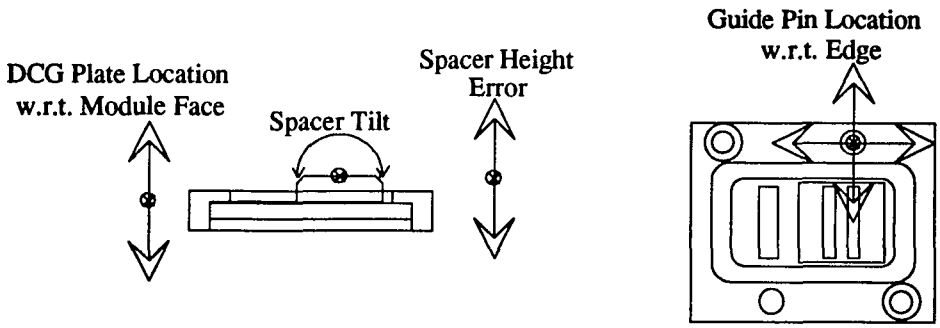

Figure 6.2. Plateholder Error Analysis

6.1.1.3 Glass Spacer

The positioning of the glass spacer is performed using a fixture as described in chapter 4. The accuracy in setting the spacer height is determined by the accuracy of the fixture which is approximately +/-0.02 mm while the tilt is within (0.02 mm / 10 mm) radian =+/-0.11 degree.

6.1.1.4 E/O module

The accuracy of the lateral position of the apertures for the laser diode and detector are the combined accuracy of guide pin location, aperture center location, and lens cap/aperture. The lathing process used to produce the lens caps and guide pins yield

centering accuracy for the aperture of +/-0.015mm while the guide pin diameters are within +/-0.01mm. The mill was used to drill the receiving holes for the guide pins in the E/O module to within +/-0.015 mm in lateral and vertical directions.

The total accuracy of the aperture center referenced to the guide pins is the rms of the aperture centering and guide pin lateral and vertical location error of +/-0.03mm.

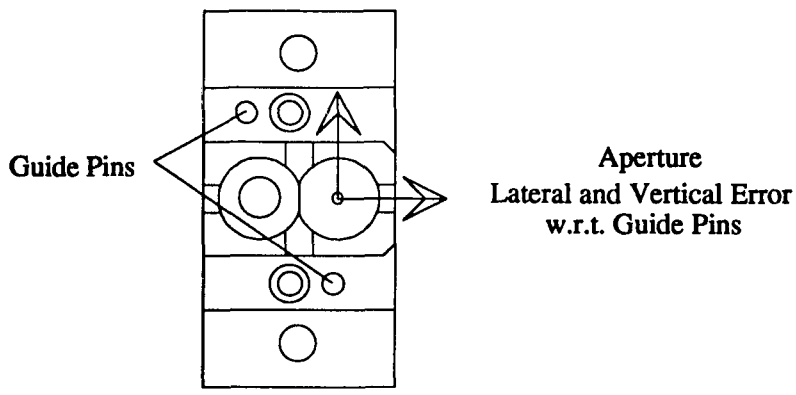

Figure 6.3. E/O Module Error Analysis

6.1.2 HOE Fabrication Variations

The exposure procedure for the HOE modules described in Chapter 4 has several sources of fabrication error: the basic accuracy of the rotation stage, the accuracy of the fixture alignment procedure, accuracy of the exposure mask, and exposure variation. The rotation stage used for exposure (Newport RSX-2) has 5 arc minute absolute resolution using a vernier scale.

The alignment procedure for the exposure arrangement described in chapter 4 consists of using back reflections from a dummy plate in the exposure fixture to set the correct interbeam angle. The offset of the near normal beam is then used to rotate the stage to the correct exposure angle. The error in the two beam angle settings and the

offset angle can be treated independently to create a total error equal to the root mean square of the three errors. The error in each back reflection is approximately (error at aperture/twice beam path length) = 1mm/850mm rad. =0.067 degree. The root mean square of back reflection error and the rotation stage setting accuracy is the rms of 0.083 deg and 0.067 deg = +/-0.11 deg.

One quantity of interest is the error in grating period due to variation in exposure beam angle. This error can be derived from the estimated error in beam angles and the plane grating equation. We can ignore any tilt of the DCG plate with respect to the reference surface of the HOE module because the exposure method makes this tilt irrelevant. The equation for grating period in lines/micron is $1/d = (\sin\alpha - \sin\beta)/\lambda$ and the actual exposure angles used were α=13 degrees and β=49 deg 50 min (figure 4.2). The maximum and minimum grating period for +/-0.11 deg beam angle error is 1.054 lines/micron max. and 1.042 lines/micron min. The beam offset error, which either adds or subtracts 0.083 deg from both beam angles, increases grating period error to 1.055 lines/micron maximum and 1.041 lines/micron minimum.

6.1.3 Active Alignment Errors

The collimation and alignment of the laser diode beam and the detector in the electro-optics module was performed using the alignment procedure detailed in Chapter 2. The accuracy of collimation and alignment of the laser diode beam on the E/O module is determined by the baseline used for setting the normal. The normal for the laser diode alignment was set using multiple back-reflections of the HeNe alignment laser with an error of approximately .5mm/(2 x 500mm) = 0.03 deg. The accuracy of aligning the laser diode beam with the prealigned apertures was about 1mm/700mm = 0.08 deg. The rms of these two processes yields +/-0.09 deg. total error.

The detector has an active area and focus set point as specified in Chapter 2. The estimated accuracy in setting the beam focus at the center of the detector is +/-0.01mm for both horizontal and vertical axes; however, the focus is relatively insensitive to misalignment and is ignored for this analysis. The effect of errors in lateral offset of the detector is tested by assuming smaller detector radii than the measured diameter. The 140 micron detector diameter used in the model is a good test for the effect of maximum lateral detector alignment error.

6.1.4 Thermally Induced Error

Misalignment can be introduced into an optical system by temperature changes due to expansion and contraction or by the change in optical properties such as refractive index change with temperature. The effect of uniform thermal variations on the Connection Cube Tower or the HOE Module due to the Coefficient of Thermal Expansion (CTE) of materials is limited because of geometrical symmetry. Any expansion in the HOE Module aluminum frame, for instance, is matched on all four sides and no net misalignment is produced. The same is true for the connection cube tower. One significant asymmetry in the HOE Modules that can be affected by thermal variation is the glass spacer. Two potential thermal variations in the glass spacer are the CTE and the change in refractive index. The CTE for glass is approximately $8 \times 10^{-6}/^{o}C$ and the refractive index thermal coefficient is about $10 \times 10^{-6}/^{o}C$. Small (+/-20 ^{o}C) temperature changes would produce little change in the corresponding variables and no significant change in beam alignment.

Thermal effects in the E/O Module such as index change in the plastic asphere or shifts in alignment of the laser diode are potentially significant, however, these effects are dependent on the physical structure of the E/O Module. Since the physical structure of

the single channel prototype was not intended to simulate that of the array sources, detectors, and coupling optics likely to be used in actual systems, thermal analysis of the E/O Module structure would serve little purpose and was not performed. Variation in the laser diode wavelength due to temperature is also potentially significant, however, the laser diode in the E/O Module is well heat sinked and no wavelength shift is seen during room temperature operation.

Table 6.1 Fabrication Error Summary and Source Spectrum Variation

Component	Description	Error (+/-)
Connection Cube Tower	Cube Surface Error	0.01 mm
	Cube Face Lateral Tilt	0.033 deg
	Module Recess Lateral Error	0.014 mm
	Module Recess Surface Error	0.01 mm
	Module Recess Lateral Tilt	0.03 deg
HOE Module	Module Lateral / Guide Pin Error	0.02 mm
	Module Face / DCG Plate Error	0.012 mm
	Hologram (Mask) Location Error	0.03mm
Glass Spacer	Spacer Height Error	0.02 mm
	Spacer Tilt Error	0.11 deg
E/O Module	Aperture / Guide Pin Lateral Error	0.03 mm
Guide Pin Diameter Error		0.01 mm

HOE Fabrication Error		min	1.041 lines/micron
		nominal	1.048 lines/micron
		max	1.055 lines/micron
Active Alignment Error	Laser Diode alignment to normal		0.09 deg
	Detector radial alignment		0.01 mm
Laser Diode Spectrum Variation			
	Center Wavelength Spread (Diode to Diode)		+/- 2.5 nm
	Spectrum Spread under Modulation		1.5 nm @ 500 Mhz

6.2 Beam Path Models

Optical paths in the connection cube system shown in figure 2.1 can be separated into three separate links. The implementation of these optical paths in the optical design program ZEMAX is shown in figures 6.4, 6.5, and 6.6. The variable parameters used to investigate the alignment sensitivities (lateral shift, input tilt, etc.) are shown in the figures.

Figure 6.6 shows all the apertures and variable parameters used in modeling the system. All linear errors in the lateral plane are accumulated into the lateral shift parameter and applied to the output module. The tilts near the input HOE module are accumulated in an input tilt and all the tilts near the output HOE module, except the glass spacer tilt, are accumulated in an output tilt. Three potential detector diameters (180, 140 and 100 microns) are used to quantify detector misalignment error, investigate the potential for using smaller detectors, and show the movement of the focal spot in the detector plane.

The long leg optical path model is used as the baseline for the analysis because it is the most sensitive to all system errors due to the long path length.

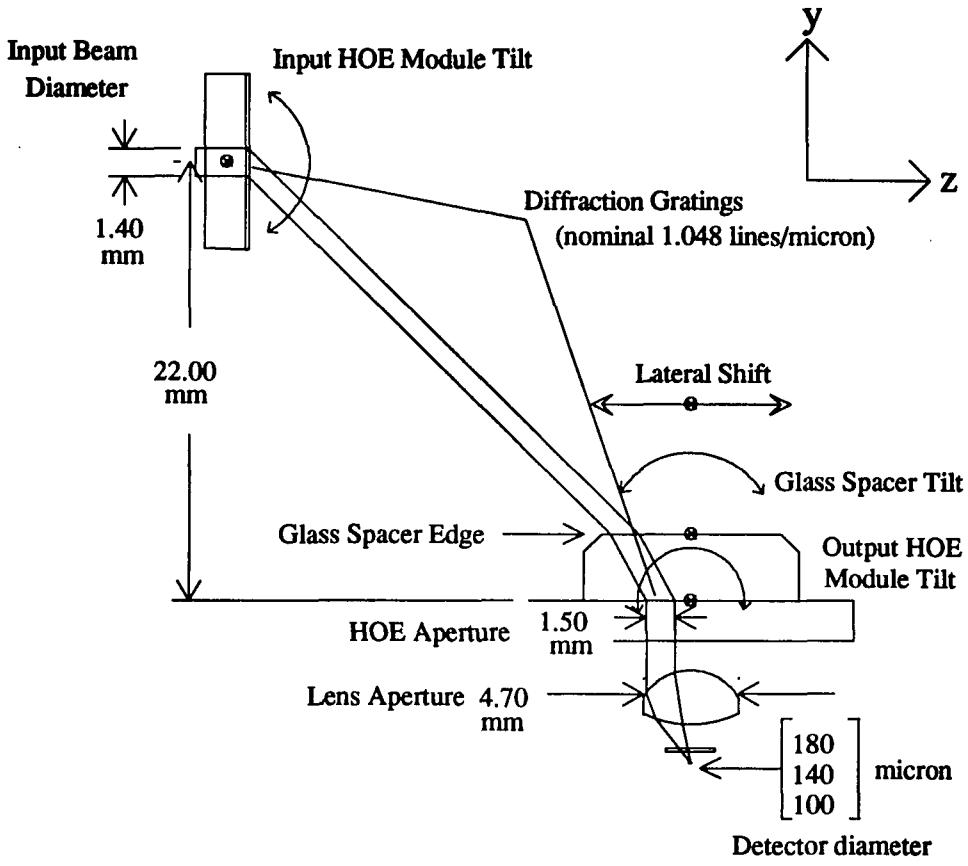

Figure 6.4 Long Leg Optical Path Model

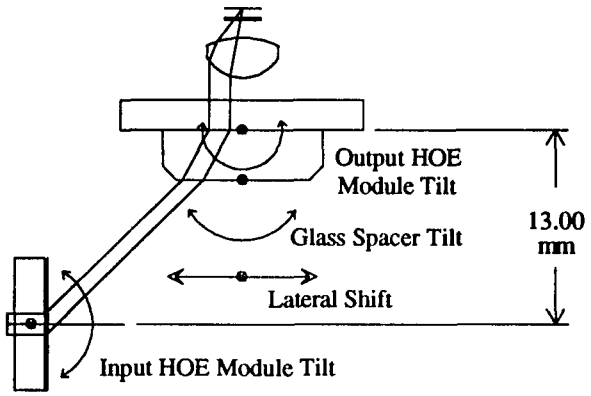

Figure 6.5 Short Leg Optical Path Model

The short leg is less sensitive to tilt related errors acting at the input because of the shorter path length.

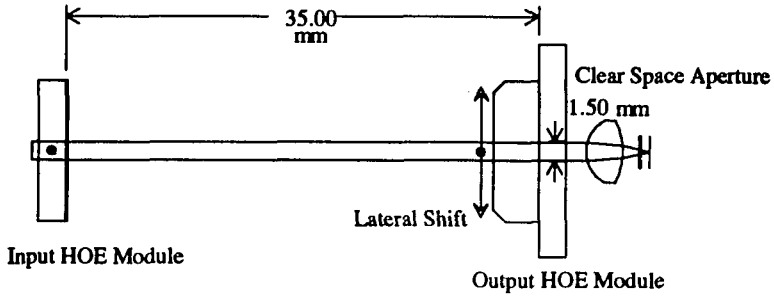

Figure 6.6 Through Beam Optical Path Model

The through beam is not affected by wavelength dependent errors because it does not depend on the diffraction angle from the grating. The spot size of the beam at the detector plane shows no aberration above the diffraction limit and this further reduces alignment errors. Input and output module tilt only produce a small lateral shift in the location of the beam, but the focus spot remains on the detector with no effect on the beam power. Only vignetting of the beam at the receive hologram aperture resulting from lateral shift affects the beam power at the detector.

6.2.1 Aspheric Lens Model

The plastic apheric lens used in the E/O Module (Universe Kogaku LP-05) is manufactured for use with laser diodes for applications such as compact disc heads. In order to model the lens performance with ZEMAX, the lens parameters are derived by optimizing values for an asphere with the following optimum working conditions specified by the manufacturer.

Wavelength	780nm
IO distance	25.182mm
Cover Glass	1.20mm
Cover Glass index	1.56
Working Distance	1.80mm

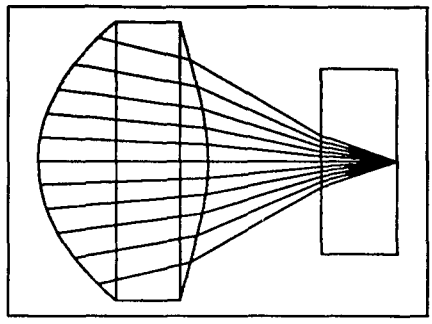

Figure 6.7 Aspheric Lens Model

Both front and back surfaces were allowed to be aspheres using the first two parameters β_1 and β_2 in the surface equation:

[eqn 6.1] $$z = \frac{c \cdot r^2}{1+\sqrt{1-(1+k)c^2r^2}} + \beta_1 r_1 + \beta_2 r_2 + \beta_3 r_3 + \ldots,$$

where k= conic constant; c= 1/radius of surface; and r = radial coordinate of the lens.

Surface 1		Surface 2	
c =	1/1.95766	c =	-1/2.81463
k =	-0.84704	k =	-5.14103
β_1 =	-0.00145	β_1 =	-0.00203
β_2 =	-0.02527	β_2 =	0.03528

6.3 Optical Beam Profile

The profile shown in figure 6.8 for a collimated beam produced by an E/O Module was measured using a 200 micron aperture scanned across the aperture. The vertical gaussian profile is well within the 1.4mm beam aperture while the horizontal profile is vignetted. The optical beam profile in the error analysis is assumed to be uniform because the difference between vignetting of a uniform beam and the broad gaussian beam is small, and the uniform beam profile gives slightly more conservative results.

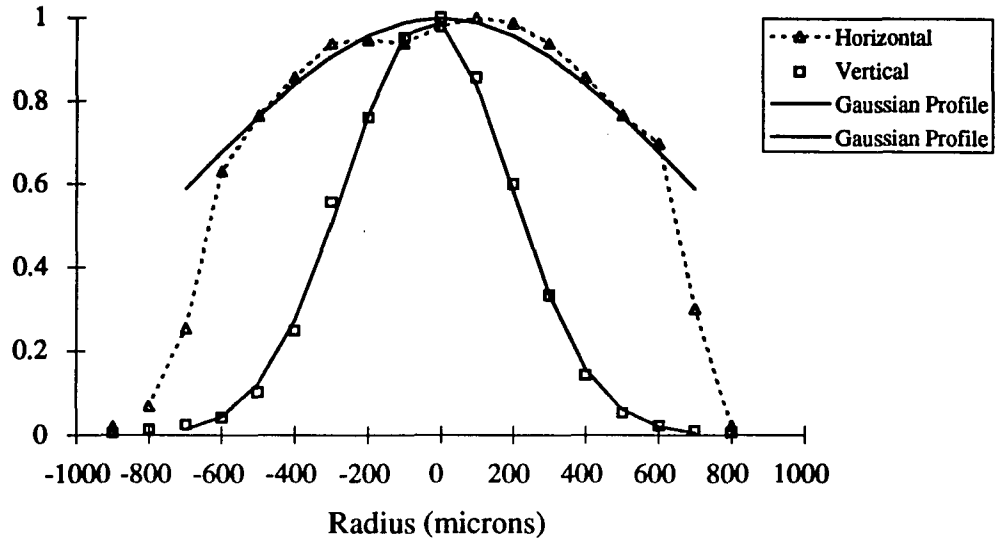

Figure 6.8 Collimated and Apertured Beam Profile

6.4 Estimated Lateral Misalignments

The estimated errors in each component must now be gathered together and simplified into the relevant single parameters that are shown in the beam path models. Root mean squared (RMS) accumulations of the individual errors are made because each error is independent.

6.4.1 Off Axis Beam Lateral Shift

For the 45 degree off-axis beams all lateral linear misalignments can be gathered into one parameter. The justification for this can be understood by looking at figure 6.4 and considering what a displacement in either of the orthogonal lateral directions has on the beam. For example, any positive offset along the y axis of the output HOE module results in an equal negative offset in the z direction of the collimated beam relative to the glass spacer surface. Each lateral error except the glass spacer height error and hologram

location error must be considered for both input and output. Gathering all the errors together and taking the rms :

Description	Error (mm)	Locations
Cube Surface Error	0.01	x2
Aperture/ Guide Pin Error	0.02	x2
Guide Pin Diameter Error	0.01	x2
Module Recess Lateral Error	0.015	x2
Module Recess Surface Error	0.01	x2
Module Face / DCG Plate Error	0.015	x2
Glass Spacer Height Error	0.02	x1
Hologram Location Error	0.03	x1
Off Axis Beams Lateral Shift RMS	0.06 mm	

6.4.2 Through Beam Lateral Shift

The through beam is distinct from the off-axis beams in that errors in the two axes are not coupled. In addition, the through beam is very insensitive to errors along the beam axis. Considering only lateral shifts:

Description	Error (mm)	Locations
Aperture / Guide Pin	0.02	x2
Module Recess Lateral Error	0.015	x2
Guide Pin Diameter Error	0.01	x1
Hologram Location Error	0.03	x1
Through Beam Lateral Shift RMS	0.05 mm	

6.4.3 Input Tilt

The input and output tilts are separated because the effects are translated to the detector along different path lengths. All tilts near the input HOE module are gathered

together and centered on the input HOE module as shown in the beam path models.

Description	Error (deg)
Laser Diode alignment to normal	0.09 deg
Cube Face Lateral Tilt	0.033 deg
Module Recess Lateral Tilt	0.03 deg
Input Tilt RMS	0.10 deg

6.4.4 Output Tilt

Output tilt includes all tilts in the output HOE module as well as tilt to the E/O module produced by the cube face.

Description	Error (deg)
Cube Face Lateral Tilt	0.033 deg
Module Recess Lateral Tilt	0.03 deg
Glass Spacer Tilt	0.11 deg
Output Tilt RMS	0.12 deg

6.5 Calculated Sensitivity of Model Parameters

Figures 6.9 to 6.16 show calculated sensitivity of each of the variable parameters in the optical path models. The vertical axis is given as relative output power and is a measure of the number of vignetted rays in a 2500 random ray trace performed for each data point in each plot.

6.5.1 Lateral Shift

Lateral shift in all three optical path model results in vignetting at the receive

hologram over the range calculated (+/-0.6mm). As a consequence, all three beam paths have the same characteristic error plot shown in figure 6.9. The region of estimated error is shown.

6.5.2 Input Module Tilt

The effect of input module tilt for both the short and long legs is shown in figure 6.10. The through beam has no appreciable sensitivity to input module tilt and is not shown.

6.5.3 Glass Spacer Tilt

The glass spacer tilt error shown in figure 6.11 is considered separately from the output module tilt because of the separation of the glass spacer surface from the module. The asymetric characteristic of the plots for the smaller diameter detectors is common to all the plots showing errors that induce tilt in the beam prior to the aspheric lens. The asymmetry is due to coma in the off-axis image spot.

6.5.4 Output Module Tilt

Output module tilt has the same effect on the short and long legs (figure 6.12). Once again, the through beam is not sensitive to output module tilt. The drop off in power is produced only by the image spot walking off the detector; no vignetting is produced.

6.5.5 Grating Period

The error in the grating period is introduced to both gratings simultaneously since the exposure procedure ensures that both gratings are the same. The effect of vignetting at the hologram plane as well as the effect of tilt is seen in the plots for the short and long leg grating period error (figure 6.13 and figure 6.14). Vignetting produces the larger droop in the top line in the long leg as compared to the short leg. The curves showing the effect of reduced detector diameter are the same for the short and long leg, indicating that similiar tilts are induced by the grating period error in the short and long legs.

The error limits calculated from the system errors are large enough to make the use of a small detector diameter unacceptable. This indicates that a future system should more tightly constrain the hologram construction errors.

6.5.6 Wavelength Error

The wavelength error plots (figures 6.15 and 6.16) are similiar to the grating period error plots since the effect of wavelength change is identical to a grating period change. Once again, the wavelength error limits are large for the prototype system. A practical system would require tighter specification of the acceptable laser wavelength variation than that provided in the literature (+/- 10nm). The consistency of the individual laser diodes used in the prototype system, however, indicates that it is possible to produce laser diodes in reasonable quantity with small wavelength variation (+/-2.5nm).

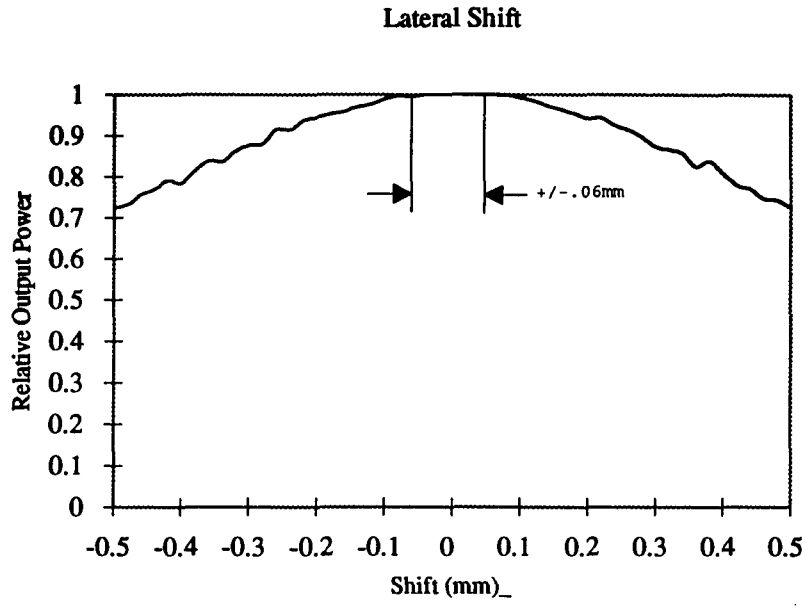

Figure 6.9 Lateral Shift

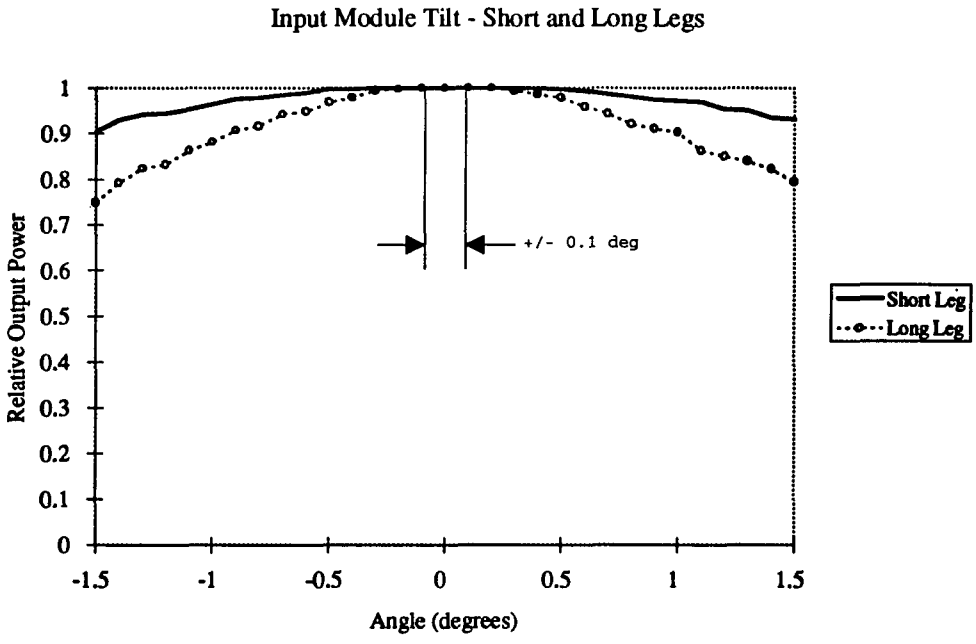

Figure 6.10 Input Module Tilt

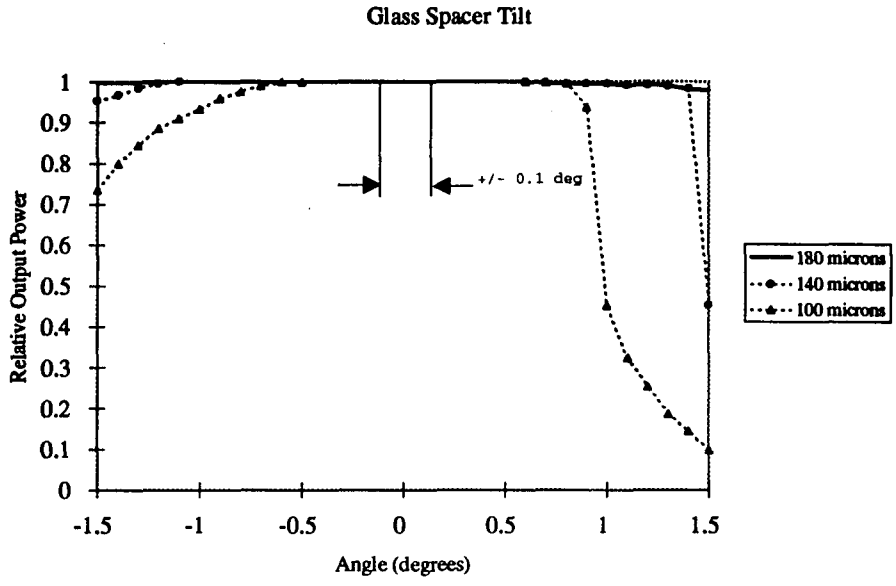

Figure 6.11 Glass Spacer Tilt

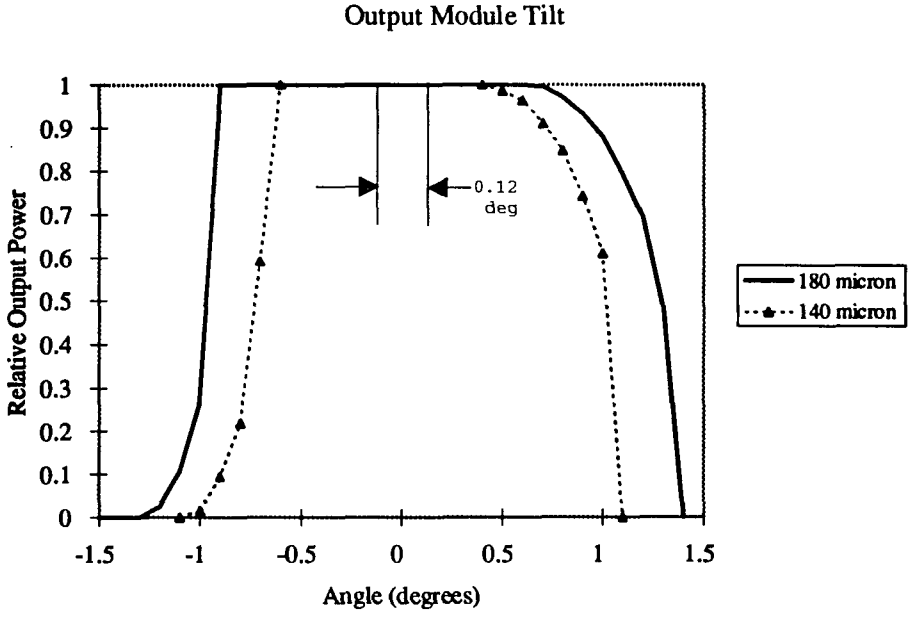

Figure 6.12 Output Module Tilt

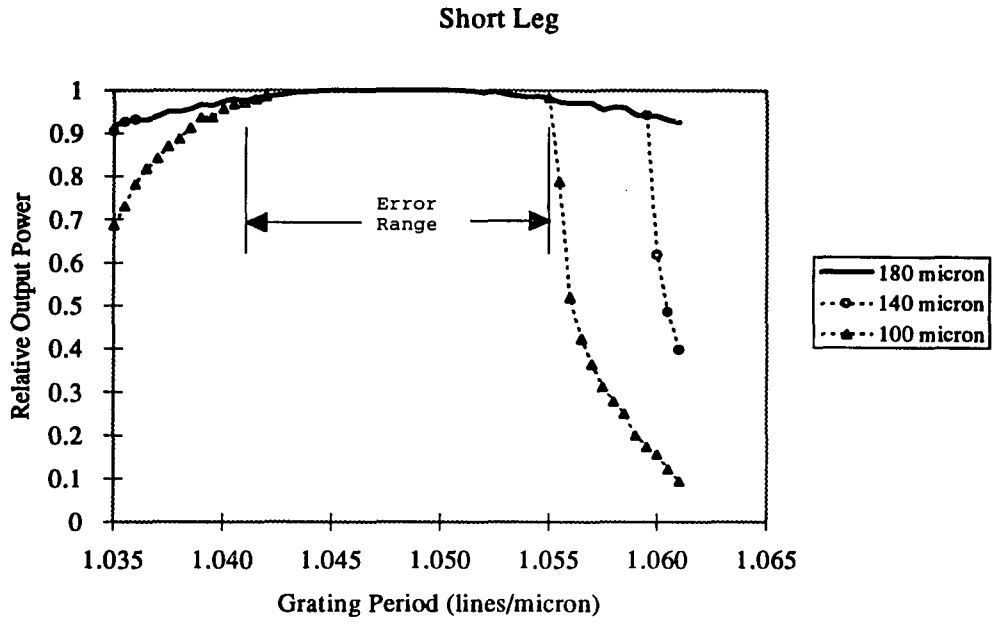

Figure 6.13 Grating Period Error - Short Leg

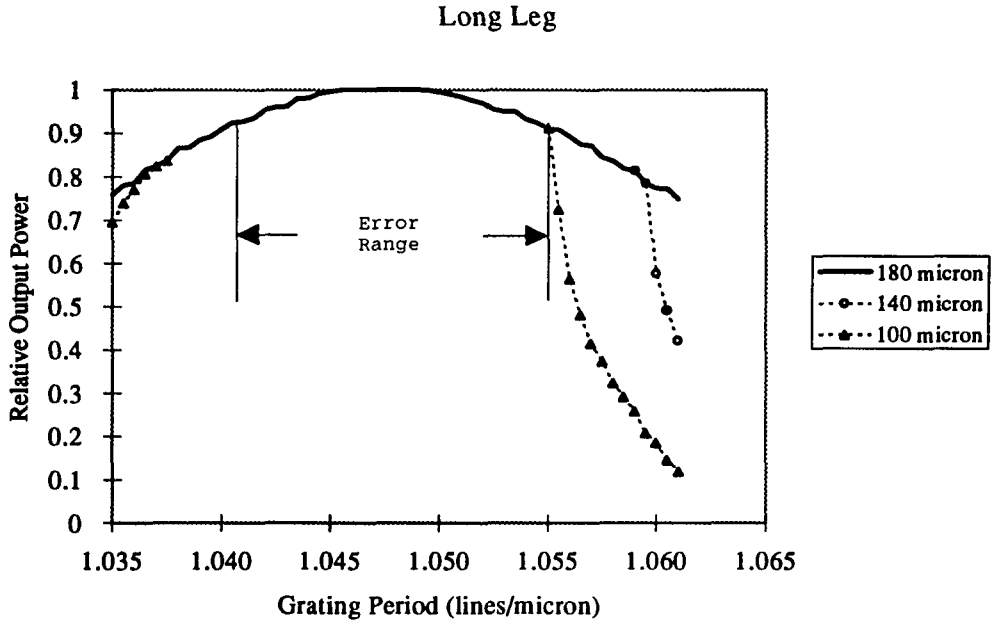

Figure 6.14 Grating Period Error - Long Leg

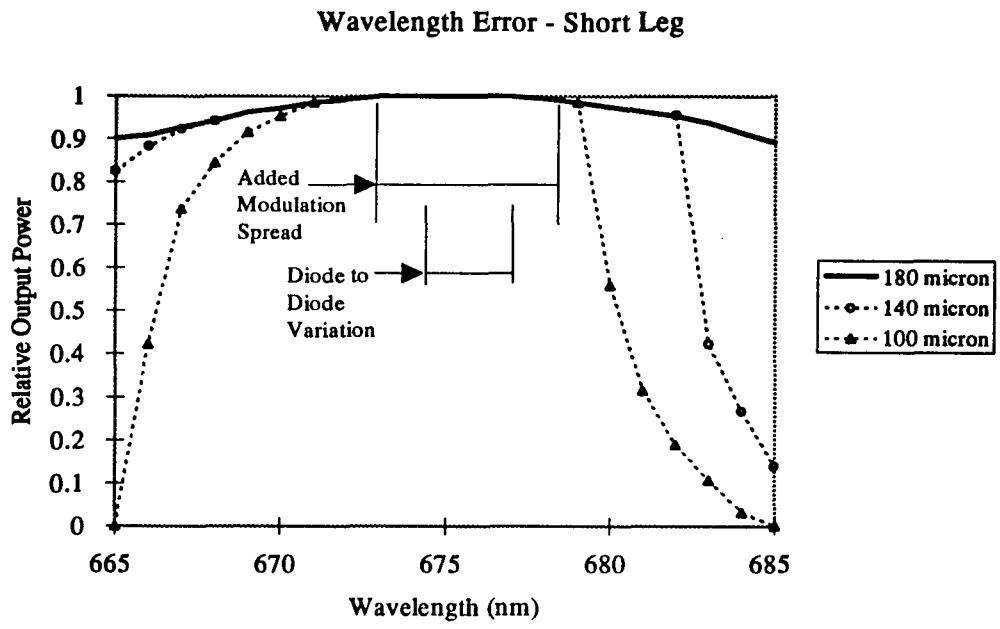

Figure 6.15 Wavelength Error - Short Leg

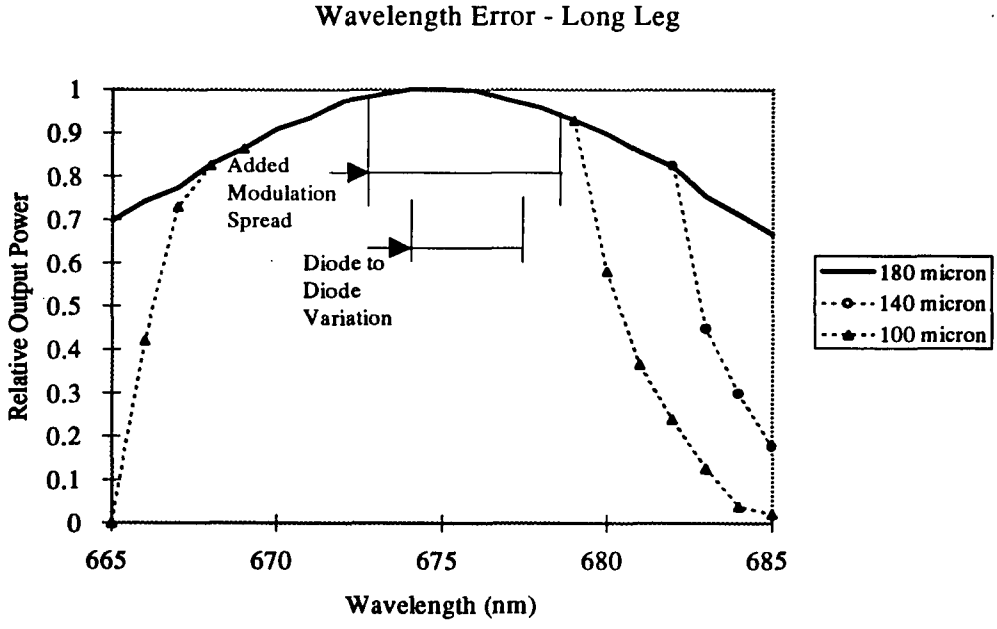

Figure 6.16 Wavelength Error - Long Leg

6.6 Vertical Misalignments

No vignetting occurs at the receive hologram or the glass spacer for vertically misaligned beams. Also, grating period error and source wavelength variation do not contribute to vertical misalignment. Figures 6.17 and 6.18 show that tolerance for vertical shift is greater than for lateral shift, while vertical tilt tolerance is about the same as lateral output module tilt. Vertical misalignments are thus less critical than lateral misalignments.

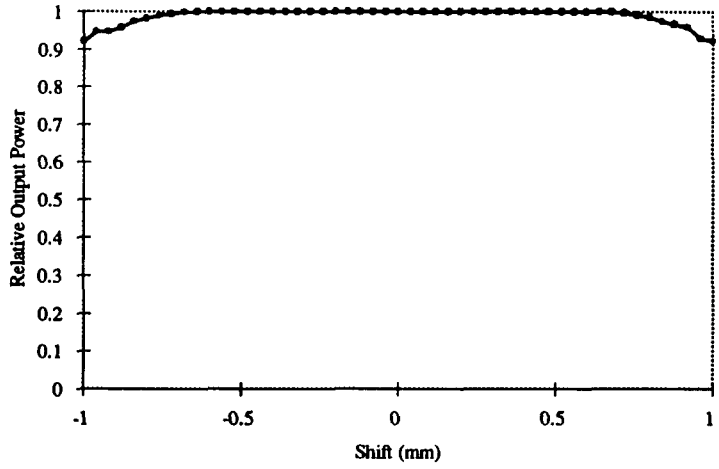

Figure 6.17 Vertical Shift Error

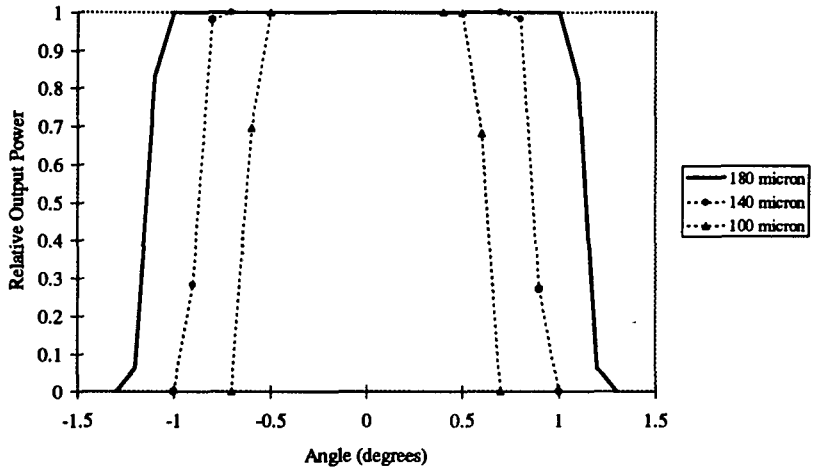

Figure 6.18 Vertical Tilt Error

6.7 Focal Spot Effects of Spectrum Spread due to Modulation

Spot diagrams for the long off-axis beam were made for single wavelength (675nm) and for the broad spectrum given in chapter 5 for the laser diode modulated at 500 Mhz.

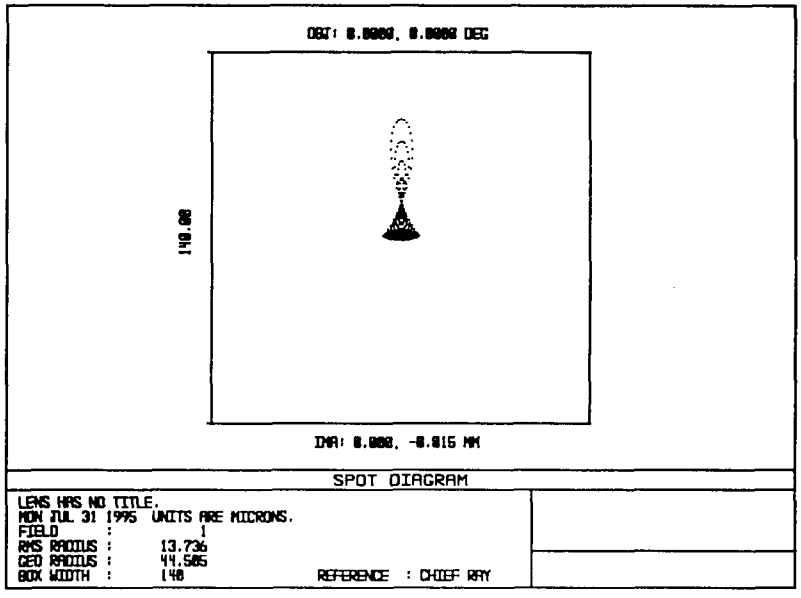

Figure 6.19 Spot Diagram for 675nm Long Leg Beam

The lateral and vertical directions are interchanged from the spot diagram plots to the prototype(i.e., the vertical direction in the spot diagram is the lateral direction in the prototype). The box area for the off-axis spot diagrams is 140μm x 140μm centered on the detector. The abberation introduced by the off-axis positioning is evident, but, there is little difference in the spot size introduced by the spectral spread in the source wavelength relative to the size of the detector.

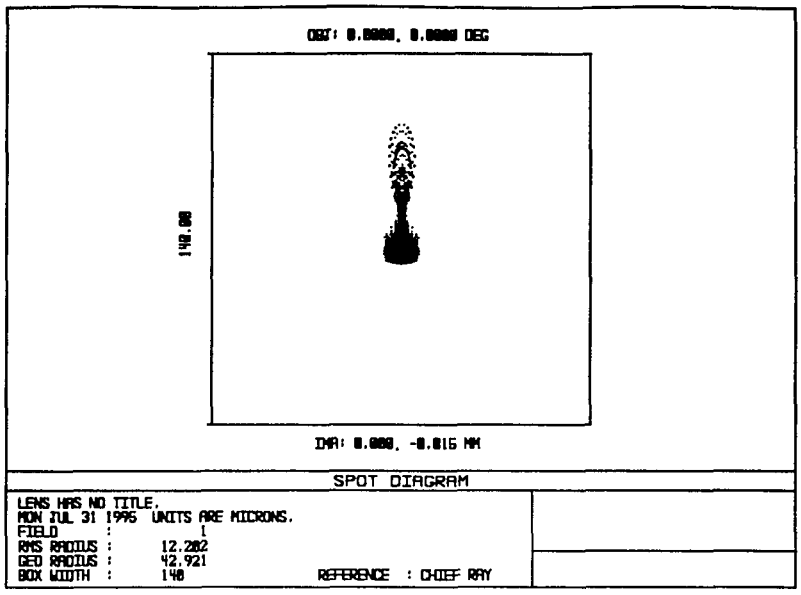

Figure 6.20 Spot Diagram for 500Mhz Modulation Spectrum (ref. figure 5.5)

6.8 HOE and E/O Module Alignment Tests

Several alignment tests of the HOE Modules and the E/O Modules without electronics were made in the connection cube tower. The four test HOE modules are designated 1 to 4 as are the four cube positions and the four E/O modules.

The first test checked the consistency of the four E/O modules by mating E/O module #3 to cube position 1 with the HOE modules in the configuration shown in figure 6-21. The laser diode in E/O module #3 was turned on to 40 mA input current, then detector current output from the other three E/O modules was measured as they were mated to each cube position. Finally, E/O module #1 was mated to cube position 1 and its laser diode was turned on to 40 mA. Detector output from E/O module #3 was measured at each cube position. The results are shown in table 6.2 with X indicating source location.

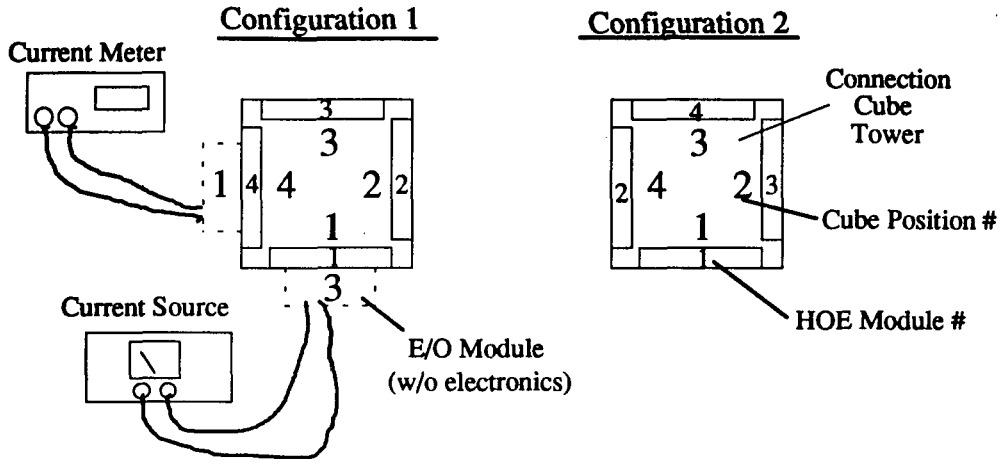

Figure 6.21 HOE Module Mating Locations for Alignment Tests

Table 6.2 E/O Module Consistency Test - Detector Output Current in μA

	Output Cube Position			
E/O Module	1	2	3	4
1	X	72.5	172	97.8
2	X	69.9	170	112
3	X	73.3	170	111
4	X	70.0	163	103

The random error in detected power in each output position is small. The standard deviation for each column is about 2%. This shows excellent consistency between the E/O modules and demonstrates that random alignment errors are small.

6.8.1 Calculated Beam Efficiencies based on HOE Module Measurements

The measured module efficiencies for normal beam incidence are given in table 6.3 These numbers are taken prior to fixing the glass spacer or the cover slip over the DCG plate and include Fresnel reflection from the front and back surfaces. These numbers are used to calculate beam efficiencies given in table 6.5

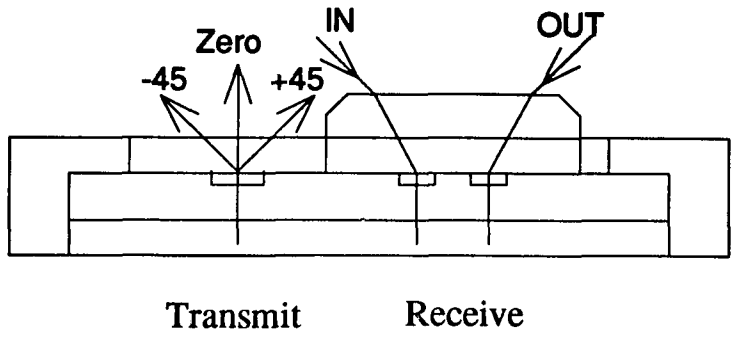

Figure 6.22 HOE Module Beam Designations

Table 6.3 HOE Module Fractional Efficiencies at Normal Incidence (uncompensated for Fresnel reflection)

	Multiplexed Grating			Inside Grating	Outside Grating
Module	+45	Zero	-45	IN	OUT
1	.275	.324	.237	.703	.659
2	.343	.188	.297	.695	.703
3	.237	.401	.215	.785	.714
4	.272	.289	.262	.763	.752

Each optical beam path in the connection cube is diffracted by two holograms, the 1-to-3 fan-out transmitter hologram and the receiver hologram. The total expected efficiency of each optical path for configuration 1 and 2 can be calculated from the measured HOE Module efficiencies in table 6.3 by multiplying the efficiencies of the gratings in each path. Table 6.4 gives each combination of input and output grating for the four HOE modules in configurations 1 and 2. For instance $+45_1$ is the +45 beam efficiency in the multiplexed grating on HOE Module 1, and for configuration 1, the corresponding output grating efficiency is the outside grating in HOE Module 4 or OUT_4. Power lost by reflection in the through beam is accounted for by the factor **R**.

Table 6.4 Total Beam Efficiency Factor Matrix

Configuration 1

		Output Cube Position			
		1	2	3	4
Input	1	X	$-45_1 * IN_2$	$Zero_1 * R$	$+45_1 * OUT_4$
Cube	2	$+45_2 * OUT_1$	X	$-45_2 * IN_3$	$Zero_2 * R$
Position	3	$Zero_3 * R$	$+45_3 * OUT_2$	X	$-45_3 * IN_4$
	4	$-45_4 * IN_1$	$Zero_4 * R$	$+45_4 * OUT_3$	X

Configuration 2

		Output Cube Position			
		1	2	3	4
Input	1	X	$-45_1 * IN_3$	$Zero_1 * R$	$+45_1 * OUT_2$
Cube	2	$+45_3 * OUT_1$	X	$-45_3 * IN_4$	$Zero_3 * R$
Position	3	$Zero_4 * R$	$+45_4 * OUT_3$	X	$-45_4 * IN_2$
	4	$-45_2 * IN_1$	$Zero_2 * R$	$+45_2 * OUT_4$	X

Table 6.5 gives the calculated beam efficiencies by combining the grating efficiency data given in table 6.3 with the total beam efficiency factor matrix given in table 6.4.

Table 6.5 Calculated Beam Efficiencies Based on Module Data (Relative to Total Output)

Configuration 1

		Output Cube Position			
		1	2	3	4
Input	1	X	.246	.445	.309
Cube	2	.358	X	.369	.274
Position	3	.527	.239	X	.234
	4	.286	.413	.301	X

Configuration 2

		Output Cube Position			
		1	2	3	4
Input	1	X	.275	.440	.285
Cube	2	.227	X	.238	.535
Position	3	.414	.302	X	.283
	4	.307	.278	.415	X

6.8.2 Measured Beam Efficiencies

The second series of tests used E/O module #3 as the source module and E/O module #1 as the detector module. With the HOE Modules in configuration 1 (figure 6-21), the input E/O module was mated to each cube position while the output E/O module was used to measure the output at each cube position. This sequence of measurements was repeated for the second HOE module configuration.

Table 6.6 Measured Beam Efficiencies Relative to Total Output

Configuration 1		Output Cube Position			
		1	2	3	4
Input	1	X	.211	.503	.285
Cube	2	.370	X	.328	.301
Position	3	.582	.221	X	.296
	4	.278	.407	.315	X

Configuration 2		Output Cube Position			
		1	2	3	4
Input	1	X	.231	.501	.267
Cube	2	.217	X	.209	.574
Position	3	.416	.299	X	.284
	4	.271	.309	.420	X

Comparison of the actual to calculated beam efficiencies shows the standard deviation between the two is 3.3%. This demonstrates that variation in beam output is dominated by the HOE module efficiencies and not by random misalignments.

The final comparison of calculated total output efficiency to actual total output shows that there is a 16% uniform loss above that predicted by the individual HOE module measurements. This may be due to excess loss in the UV cement, glass spacer loss, or grating period error (figures 6.13 and 6.14). All of these factors could produce uniform (not random) loss.

Table 6.7 Comparison of Measured and Calculated Total Output Efficiency

	Configuration 1			Configuration 2		
	Calculated	Measured	Meas./Calc	Calculated	Measured	Meas./Calc
1	.670	.571	.852	.677	.582	.860
2	.632	.507	.802	.688	.579	.842
3	.700	.587	.839	.642	.557	.868
4	.644	.524	.814	.622	.516	.830

Average Measured / Calculated = 83.9%

Standard Deviation Measured / Calculated = 2.2%

Chapter 7
Alternate System Components

The connection cube system prototype is a starting point for the development of a board level free space optical interconnect. Application of free space optical interconnects to computer architectures requires the development of array sources, detectors, and lenses to provide bus oriented communication. In this chapter, potential components for future development are examined and evaluated.

7.1 Sinusoidal Surface Relief Gratings

The optical functions performed in the prototype system are beamsplitting, beam directing, collimation, and focusing; and all of these functions can be performed by diffractive elements. Surface relief diffractive elements are an alternative to volume holographic elements that provide greater potential for mass production. Surface relief elements can be created in optical substrates using processing techniques borrowed from semiconductor technologies[29,30], or replicated using plastic molding techniques.[31]

Sinusoidal gratings may simplify design of a 1 to 3 beamsplitter element for several reasons:

-The off-axis beams have identical amplitudes.

-Diffraction efficiency of the resulting grating varies slowly with input angle.

-Only one exposure is required to produce the beamsplitter grating in photoresist.

As a consequence of single exposure fabrication, the only variable that needs to be optimized is exposure energy. The resulting photoresist grating can be used as a master in a replication process to produce multiple copies of the grating[32].

Dispersion characteristics of the grating as determined by the grating frequency are identical to the volume grating, and so output angle variations for small wavelength changes are the same as for the volume grating.

7.1.1 Diffracted Order Amplitudes

Sinusoidal surface relief gratings can be described by the transmittance function [33]:

[eqn. 7.1] $$t(x,y) = e^{\left[j\frac{m}{2}\sin(2\pi f_o x)\right]} rect\left(\frac{x}{l}\right) rect\left(\frac{y}{l}\right).$$

The factor (m/2) is the amplitude of the phase variation in the grating and is proportional to the height of the surface relief structure.

Following the derivation in reference [33] the intensity of the Fraunhofer (far field) diffraction pattern for a unit amplitude field incident normal to the grating surface is:

[eqn. 7.2] $$I(x,y) = \left(\frac{l^2}{\lambda z}\right)^2 \sum_{q=-\infty}^{\infty} J_q{}^2\left(\frac{m}{2}\right) \mathrm{sinc}^2\left[\frac{l}{\lambda z}(x_o - q f_o \lambda z)\right] \mathrm{sinc}^2\left(\frac{ly}{\lambda z}\right).$$

The intensity of the diffracted order q is proportional to the square of the Bessel function , or: $I \propto \left[J_q(m/2)\right]^2$. The relative amplitudes of the diffracted orders are given by squared Bessel functions of different orders as shown in figure 7.1. The value of each Bessel function at a given phase depth gives the relative amplitudes of each diffracted order in the grating. For a 1 to 3 beamsplitter only the zero and +/-1 orders (J0,J1) are significant and nearly all relative amplitudes between the zero and +/-1 orders are accessible. However, if an element with 0,+/-1,+/-2 orders (5 beam fan-out) is desired, it is seen from the plot that all relative amplitudes between the orders are not possible.

Beamsplitter design using sinusoidal gratings becomes a trade off between obtaining appropriate beam amplitudes without losing energy in higher order diffracted beams.

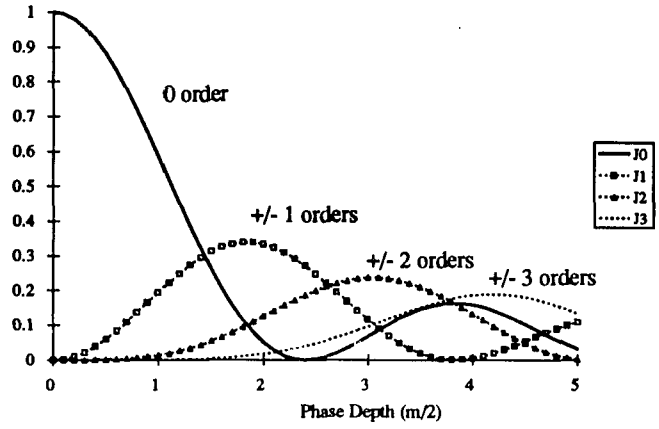

Figure 7.1 Sinusoidal Surface Relief Beamsplitter - Power vs. Phase Depth

Several sinusoidal surface relief gratings were fabricated by spinning Shipley 1811 photoresist on a glass substrate and using the 457.9 nm Ar+ line in an exposure configuration given in figure 7.2. The exposure angles were set to produce a sinusoidal grating of frequency 1.044 lines/micron.

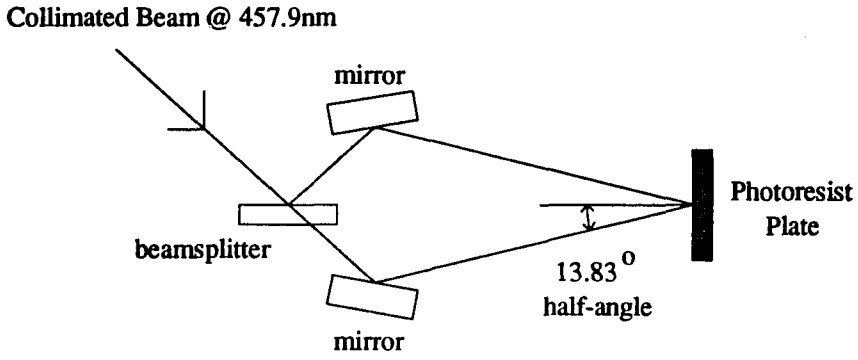

Figure 7.2 Photoresist Exposure Setup

The slow variation of diffracted beam power with input angle in a surface relief grating helps make the system less sensitive to misalignments. Diffracted beam powers in the sample photoresist gratings were measured and are shown in figure 7.3. Note that the off-axis beams have nearly identical amplitudes at normal incidence and the off-axis beams have higher power to compensate for reflection loss in the off-axis beam paths.

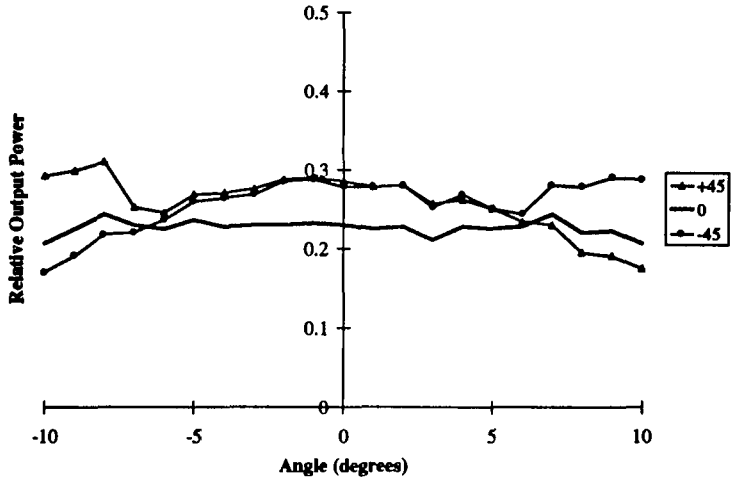

Figure 7.3 Photoresist Surface Relief Beamsplitter Power Out vs. Angle

7.2 Binary Phase Lenses

The large diameter aspheric lens used in the prototype system is not a practical solution for a real free space interconnect system. A practical system with dense, highly parallel connection paths would require arrays of microlenses to provide collimation and focusing. One candidate technology for implementing this function are diffractive microlenses fabricated using lithographic techniques common to the semiconductor industry[29,30].

Binary phase lenses are diffractive elements that approximate the 2π contour of a Fresnel-type lens by successive etch steps. A four phase level lens is shown with the ideal

profile in figure 7.4. The lithographic process used to produce the etched pattern permits $N=2^m$ phase levels where m = number of masks/etch steps. Thus an 8 level binary lens would require 3 masks and 3 etch steps.

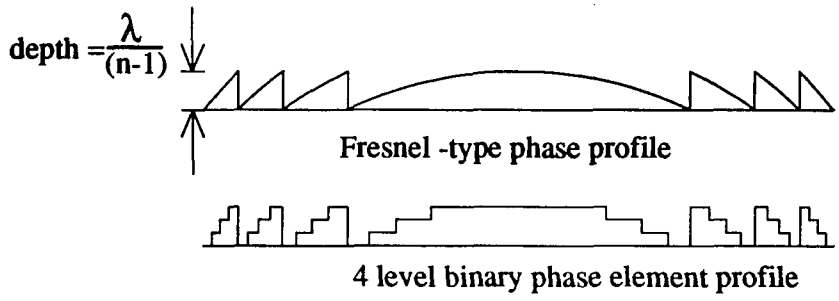

Figure 7.4 Binary Lens Element Phase Profile

The efficiency of a binary phase lens is related to the number of phase levels used as shown in table 7.1. The ideal efficiency of a binary lens becomes comparable to reflection losses at 8 to 16 phase levels. Actual efficiency of binary lenses is dependent on process parameters such as the accuracy in aligning exposure masks and control of etch depth. Controlling these process parameters becomes increasingly difficult with more masks and etch steps, and thus, more phase levels.

Table 7.1 Binary Lens Efficiency per Phase Level

Masks/Etch Steps	# phase levels	maximum efficiency
1	2	40.5%
2	4	81.1%
3	8	95%
4	16	98.7%

The efficiency of high NA binary lenses is critical for application to free space interconnects. The limiting factor for the number of phase levels in a binary lens is the minimum feature size at the edge of the lens. The minimum feature size can be

approximated by the equation $\Delta r \approx \frac{\lambda_o f}{D \cdot N}$, where f=focal length, D=lense diameter, and N=number of phase levels. This equation can also be stated in terms of the half angle of a hypothetical source $\Delta r \approx \frac{\lambda_o}{N \tan\theta}$.

To guage the performance of a real binary lens in producing collimated beams for a free space interconnect system, a binary phase lens was used to collimate a 657nm laser diode identical to those used in the prototype system. The binary phase lens is etched in fused silica with a diameter of 1.85mm, a focal length of 2.5 mm, and has a central region with four phase levels (880 micron diameter) with the remaining area having only two phase levels.

The measured profile of the incident source beam at the lens and of the collimated beam out of the lens are shown in figure 7.5. The input beam profile was measured by scanning an aperture across the diverging source beam near the lens plane. The collimated output beam profile was measured by scanning the aperture across the collimated beam at 6mm distance from the lens to reduce stray undiffracted light. The low off-axis lens efficiency and the transition from four to two phase levels is evident in the horizontal output beam profile shown in figure 7.5.

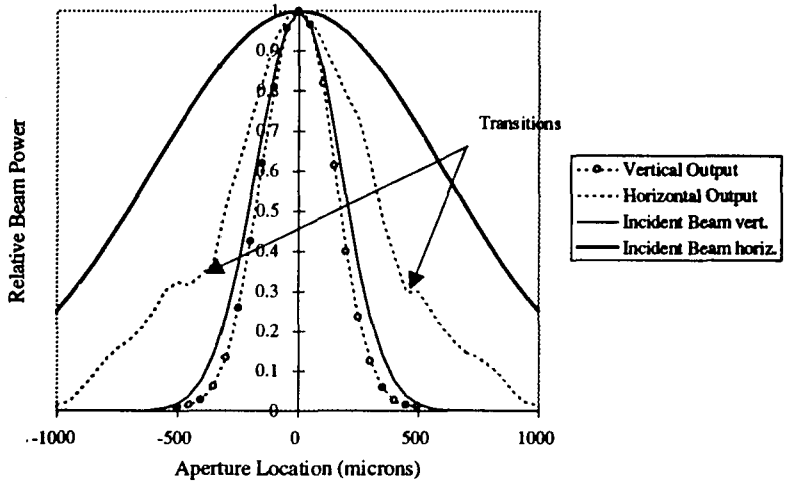

Figure 7.5 675nm Laser Diode Beam Profile - (Collimated with Binary Lens)

The reason for the transition from four phase levels to two phase levels can be guessed from figure 7.6. The minimum possible feature size for the process used is evidently 1 micron and this limits the realm of four phase levels to less than 850 microns while the upper limit of the two phase levels at this minimum feature size is about 1800 microns.

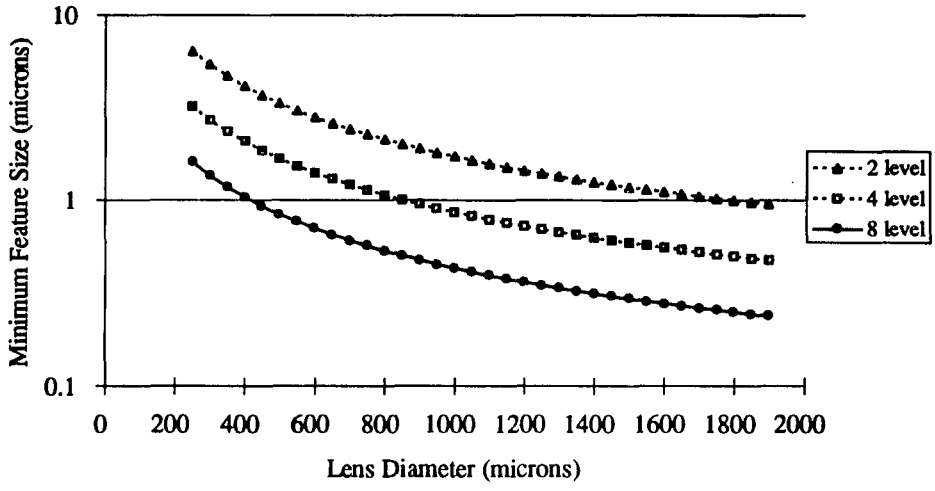

Figure 7.6 Binary Lens Minimum Feature Size vs. Lens Diameter at 675nm for f= 2.5mm

The rapid fall off of the beam power with diameter when compared to the beam produced by the aspheric lens in figure 6.8 demonstrates that this binary lens is inefficient in collimating the divergent laser diode beam. A plot of minimum feature size vs. source divergence angle (figure 7.7) demonstrates the need to use low divergence angle sources in order to access the high efficiency of 8 phase level binary elements at reasonable feature sizes (0.5 to 1 micron).

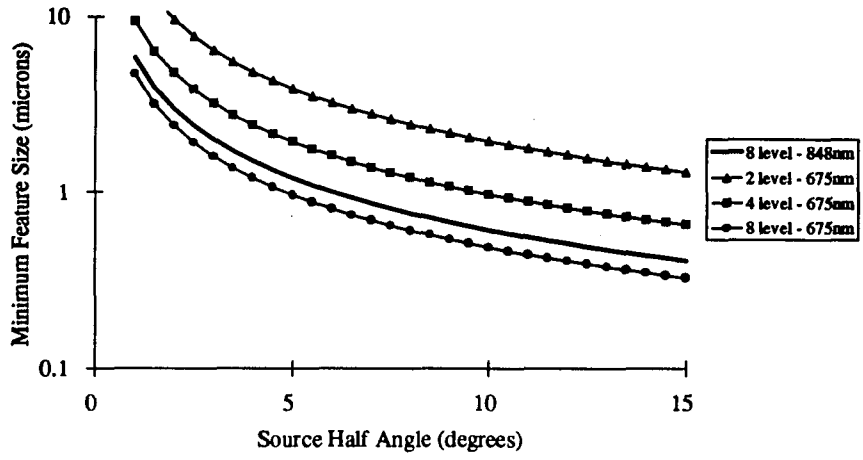

Figure 7.7 Minimum Feature Size vs. Source Half Angle for Binary Lens

7.3 Vertical Cavity Surface Emitting Lasers (VCSELs)

A promising source for highly dense free space interconnects is the vertical cavity surface emitting laser (VCSEL)[34]. A typical VCSEL structure is shown in figure 7.8 where a quantum well structure is sandwiched between epitaxially grown quarter wavelength dielectric layers that act as Bragg reflectors. This structure produces a narrow linewidth singlemode spectrum with a low divergence and nearly circular beam profile. Additionally, tight lateral current confinement reduces the threshold current[35].

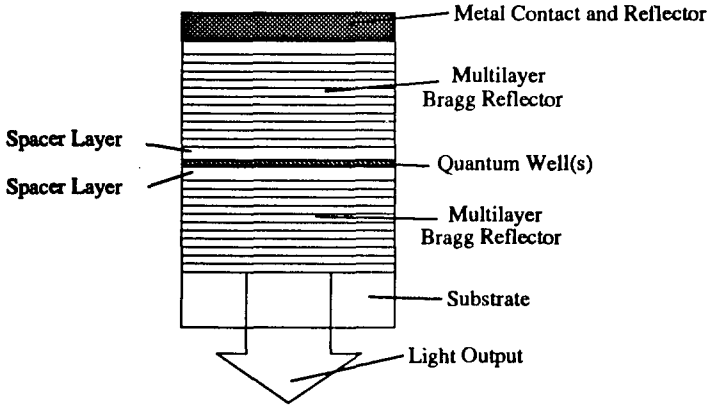

Figure 7.8 VCSEL structure

Data from a VCSEL demonstrating these properties is shown in figures 7.9 and 7.10. The optical power output vs. input current shows the low threshold current. The current to this device at threshold is 1 mA as compared to 34 mA for the laser diode that was characterized in figure 5.1. Reduced threshold current reduces power dissipation and permits densely packed interconnect spacing. High density and high speed modulation capability[36] make VCSELs ideal sources for optical interconnects in a parallel processing computer environment.

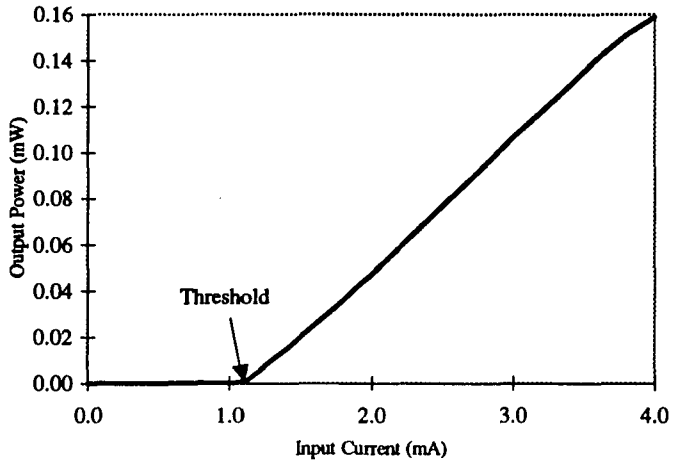

Figure 7.9 VCSEL Optical Power Out vs. Input Current

The uniform beam profile for the VCSEL shown in figure 7.10 shows a much lower divergence than the laser diode used in the prototype (figure 5.3b) as well as a circularly symmetric beam profile. Low VCSEL beam divergence makes the use of efficient binary lenses possible (see figure 7.7). VCSELs at shorter wavelengths (670nm) are being actively developed due to demand in consumer products.[37]

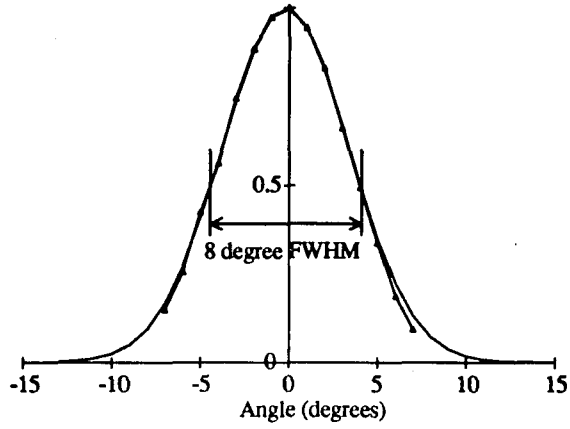

Figure 7.10 VCSEL Beam Profile

The commercial application of VCSELs is currently limited partly because the devices are in an early stage of development. Available VCSELs are limited by high series resistance (>160 ohm as compared to 16 ohm for the TOLD 9211) which increases the device RC time constant and decreases power efficiency[38]. VCSELs are currently more expensive to produce than edge emitting laser diodes due to the lack of volume applications and the high cost of equipment and process control required to produce the fine quantum well structure.

7.4 Expanding the Connection Cube Concept

The connection cube concept can be expanded to provide for interconnection of a larger number of processing boards. The fan out of the beamsplitter can be increased to increase the number of receiver boards as shown in figure 7.11 a[6]. Both volume holograms and surface relief elements can produce large fan-out, but surface relief elements may be easier to design and fabricate in this application. The configuration shown in 7.11a would be limited in maximum fan out by the high angle of the off-axis beams and by the spacing requirements of the boards.

A connection cube structure can be used as a broadcast node for multiple boards as shown in figure 7.11 b. This structure is a compromise between fully parallel and heavily multiplexed data channels. The 1-to-3 fan-out reduces the data overhead required to route data in this structure over a multiplexed single channel to all boards.

Identical HOE Modules could be used to expand the number of boards as shown in figure 7.11c. A large number of modules could be accommodated by expanding this arrangement, however, all boards are not connected via a direct path.

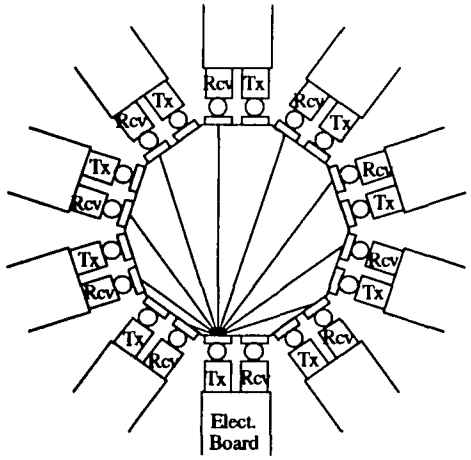

a. 1-to-9 fan-out

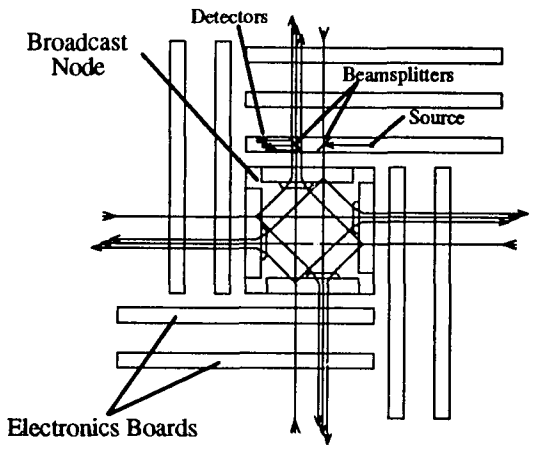

b. broadcast node

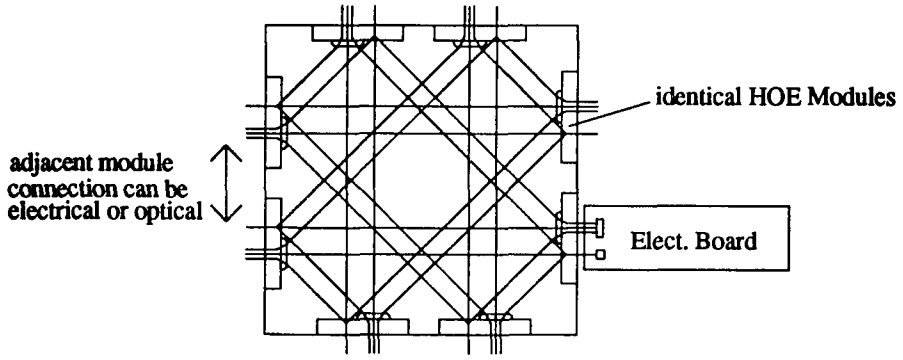

c. symmetric expansion

Figure 7.11 a,b,c Expansion of the Connection Cube Concept

Chapter 8
Conclusion

A free space optical interconnect prototype that implements the connection paths shown in figure 1.1 has been successfully fabricated and tested. Modular holographic optical elements were fabricated, demonstrating the feasibility of mass producing holographic elements for a free space interconnect. A complete electrical / optical / electrical data channel was demonstrated with a 3dB bandwidth of 320 Mhz using square wave input. The prototype system demonstrates a modular system with random alignment errors causing less than 4% power variation. The most significant factors affecting system alignment were found to be grating period error, which is caused by misalignment during hologram exposure, and wavelength variations in the laser diode sources.

Electrical interconnects have several frequency dependent factors that limit interconnect length and speed: increasing attenuation with signal frequency due to the conductor skin effect, crosstalk,[39] and greater sensitivity to path discontinuities such as connectors[40,41]. Optical interconnects, on the other hand, offer a pathway (i.e. freespace) immune to signal frequency dependent effects because the carrier frequency ($>10^{14}$ Hz) is several orders of magnitude above the signal frequency. Attenuation and crosstalk due to the optical path in an optical interconnect are determined primarily by the path geometry and carrier wavelength but are independent of the signal frequency.

A number of analyses have been made comparing electrical and optical interconnects[42,43,44,45]. The large number of parameters and the differing assumptions made in each analysis make it difficult to define a precise "break-even" point

where optical interconnects become superior to electrical interconnects. Practical limitations may be deduced from work on high speed telecommunication rack systems [46], multichip module interconnections[41], or data from state of the art supercomputer systems[47]. The referenced work deals with electrical interconnects at the backplane level (20cm to 60cm) in the 500 Mb/s to 1Gb/s range, but only point to point electrical connections (no fan-out) are demonstrated. This indicates that backplane level interconnects above 1Gb/s with multiple fan out may require optical links.

Free space optical interconnects offer several advantages over the two competing optical technologies : fiber optics and planar waveguides. Free space optical interconnects can provide more compact packaging for backplane length connections than fiber optics because the requirement for mechanical support and stress relief of the optical fiber limits the ultimate packaging density of fiber optic systems. The complexity of fabricating an interconnect system with a large number of channels (>100) and multiple fan out in a backplane level package is much less for a free space system. Multiple channels can be defined by multiple elements on a single substrate in a free space system, versus a fiber system that requires a properly terminated fiber for each path. Free space optical interconnects also offer the least propagation delay and loss over either planar waveguides or fiber optic systems. A final advantage that may apply to future computer architectures is the ability of free space optical interconnects to provide out-of-plane interconnects so that the interconnect is not confined to planar cards or boards. This would permit a large increase in effective interconnect density.

Disadvantages of free space interconnects include the requirement for line-of-sight alignment between the transmitter and receiver(s) with a clear path between them. Also, the adjacent channel density for a given propagation distance is limited by beam diffraction and the alignment tolerance of the coupling optics. Maximum beam propagation distances

using 1mm beam (channel) spacing is on the order of 1m. Finally, the demanding alignment tolerance of coupling optics (beam collimation and focusing to detectors) will require precision manufacturing techniques.

Further development of the connection cube concept as a free space interconnect requires the extension to arrays of sources and detectors[48]. The tight alignment tolerances (1μm to 2μm) required to assemble a free space interconnect system using lithographically defined element arrays is readily achieved using the C4 (flip chip) process[49]. The HOE Modules and Connection Cube Tower could be used with array sources and detectors in their current form and similar components could be designed and fabricated to fit the requirements of a given system.

Free space optical interconnect schemes have been proposed and demonstrated [4,50]; however, their competitiveness with electrical interconnects and is in part constrained by availability and the speed / power limitations of the necessary electro-optics and electronics. The near term development path for optical interconnects is probably through expanded use of fiber optic links in the computer environment. This will provide impetus for development of the electro-optical components that can then be applied to free space optical interconnects as the density and complexity of the required links exceeds the packaging capability of fiber optics.

REFERENCES

[1]. T. Lane, et. al., "Gigabit optical interconnects for the Connection Machine," *Proc. SPIE Vol. 1178 Optical Interconnects in the Computer Environment*, 1989, pp. 24-35.

[2]. Ashok K Goel, *High Speed VLSI Interconnections*, John Wiley and Sons, 1994, p. 574.

[3]. Special Issue on Optical Interconnections for Information Processing, *J. of Lightwave Tech.*, Vol. 9, No. 12, Dec. 1991.

[4]. J.P.G. Bristow, et. al., "Polymer Waveguide Based Optical Backplanes for Fine Grained Computing," *Proc. SPIE vol. 1178 Optical Interconnects in the Computer Environment*, Sept. 1989, pp. 103-114.

[5]. T. Sakano, et. al., "Design and performance of a multiprocessor system employing board-to-board free space optical interconnections: COSINE-I," *Applied Optics*, Vol. 30, No. 17,1991,pp. 2334-2343.

[6]. T.J. Kim, D. Ramsey, K. Y. Tu, T. H. Oh, and R. K. Kostuk, "Optical Interconnects for Multiprocessors in Computer Backplanes," *Proc. SPIE ,vol. 2400, Photonics West '95 - Optoelectronic Interconnects III*, Feb. 1995.

[7]. R. Collier, C. B. Burckhardt, L. H. Lin, *Optical Holography*, Academic Press, 1971.

[8]. M. C. Hutley, *Diffraction Gratings*, Academic Press, London, 1982.

[9]. D. H. Close and A. Graube, " Materials for Holographic Optical Elements," *Technical Report AFML-TR-73-267*, National Technical Information Service, 1973.

[10]. H. Kogelnik, "Coupled wave theory for thick hologram gratings", *Bell System Technical Journal*, Vol. 48, No. 9, 1969, p. 2909.

[11]. S. K. Case, "Coupled -wave theory for multiply exposed thick holographic gratings," *J.Opt. Soc. of Am.*, Vol. 65, No. 6, 1975, p. 724-729.

[12]. J. H. Yeh, "Board-level optical interconnections with substrate mode holograms," *Ph.D Dissertation, University of Arizona*, 1994.

[13]. P. Blackman, *Introduction to State Variable Analysis*, Macmillan, London, 1977.

[14]. H. Smith, ed., *Holographic Recording Materials*, Topics in Applied Physics - Volume 20, Springer-Verlag, Berlin, 1977.

[15]. T. J. Kim, "Optimization of dichromated film coatings for holographic recordings," *MS Thesis, University of Arizona*, 1991.

[16]. D. Meyerhofer, "Dichromated Gelatin," in *Holographic Recording Materials*, Topics in Applied Physics - Volume 20, H. M. Smith ed., Springer-Verlag, 1977.

[17]. D. M. Samoilovich, A. Zeichner, and A. A. Friesen, The Mechanism of Volume Hologram Formation in Dichromated Gelatin, " *Photographic Sci. and Eng.*, Vol. 24, No. 3, 1980, p. 161.

[18]. B.J. Chang, "Dichromated Gelatin holograms and their applications," *Opt. Eng.*, Vol. 19, No. 5, 1980, pp. 642-648.

[19]. G. Campbell, T. J. Kim, and R. K. Kostuk, "Comparison of methods for determining the bias index of a dichromated gelatin holograms," *Applied Optics*, Vol. 34, No. 14, 1995, pp. 2548-2555.

[20]. D. H. R. Vilkomerson and D. Bostwick, " Some Effects of Emulsion Shrinkage on a Hologram's Image Space," *Applied Optics*, Vol. 6., No. 7, 1967, p. 1270

[21]. D. Meyerhofer, "Spatial Resolution of Relief Holograms in Dichromated Gelatin," *Applied Optics*, Vol. 10, No. 2, 1971, pp. 416-421.

[22]. G.M. Naik, A. Mathur, S. V. Pappu, "Dichromated gelatin holograms, an investigation of their environmental stability," *Applied Optics*, Vol. 29, No. 35, 1990, pp. 5292-5297.

[23]. T. Kubota, " The bending of interference fringes inside a hologram," *Optica Acta*, Vol. 26, No. 6, 1979, p731.

[24]. D. D. Cook and F. R. Nash, "Gain induced guiding and astimagtic output beam of GaAs lasers," *J. of Applied Physics*, Vol. 46, No. 4, 1975, p 1660.

[25]. A. Yariv, *Optical Electronics, 4th ed.*, Holt, Rinehart, and Winston Inc., Philadephia, 1991.

[26]. T. Ikegami, "Longitudinal Mode Control in Laser Diodes," in *Optoelectronic Technology and Lightwave Communication Systems*, Chinlon Lin ed., Van Nostrand Reinhold, New York, 1989, p. 267.

[27]. T. V. Muoi, "Optical Receivers," in *Optoelectronic Technology and Lightwave Communication Systems*, Chinlon Lin ed., Van Nostrand Reinhold, New York, 1989, p. 449.

[28]. J.C. Palais, *Fiber Optic Communications, 2nd ed.*, Prentice Hall, Englewood Cliffs, NJ, 1988.

[29]. M.B. Stern, et. al, "Fabricating binary optics: Process variables critical to optical efficiency," *J. Vac. Sci. Tech. B*, Vol. 9, No. 6, Nov/Dec. 1991, pp. 3117-3121.

[30] J. Jahns, S.J. Walker, "Two-dimensional array of diffractive microlenses fabricated by thin film deposition," *Applied Optics*, Vol. 29, No. 7, 1990, pp. 931-936.

[31]. Technical Data Pamphlet, Donnelly Optics, Tucson, AZ, 1995.

[32]. I. D. Torbin and A. M. Nizhin, "The use of polyerizing cements for making replicas of optical surfaces," *Soviet J. of Opt. Tech.*, Vol. 40, March 1973, p.192.

[33]. J. W. Goodman, *Introduction to Fourier Optics*, McGraw-Hill, Inc., 1968.

[34]. J. Jewell, et. al., "Vertical Cavity Surface Emitting Lasers: Design, Growth, Fabrication, Characterization," *IEEE J. of Quantum Elect.*, Vol. 27, No. 6, 1991, pp. 1332-1346.

[35] M. Mittlestein, et. al., "Ultra low threshold Quantum Well Lasers for Computer Interconnects," *Proc. SPIE Vol. 1178 Optical Interconnects in the Computer Environment*, 1989, pp.177-187.

[36]. F. S. Chou, et. al, " High Speed Modulation of Vertical Cavity Surface Emitting Lasers, " *IEEE Photonics Tech. Let.*, Vol. 3 No. 8, 1991, p. 697.

[37]. D.M. Kuchta, et. al, "Performance of fiber-optic data links using 670nm cw VCSELs and a monlithic Si photodetector and CMOS preamplifier," *IBM J. Res. & Develop.*, Vol. 39, No. 1/2, January/March 1995, pp. 63-72.

[38]. J. Cheng, et. al.,"Surface-Emitting Laser-Based Smart Pixels for Two-Dimensional Optical Logic and Reconfigurable Optical Interconnections", *IEEE J. of Quantum Elect.*, Vol. 29, No. 2, 1993, pp. 741-800.

[39]. Tummala, Rao R. and Rymaszewski, Eugene J., eds., *Microelectronics Packaging Handbook*, Van Nostrand Reinhold, New York, 1989.

[40]. N. Sugiura and K. Yasuda, "A High-Density Multipin Connector for High-Speed Signal Transmission in a Rack System," *ECTC Proceedings - 41st Electronics Comp. & Tech. Conf.*, May 1991, pp. 256-260.

[41]. S. Sasaki, T. Kishimoto, " High-Density, High-Pin-Count Flexible SMD Connector for High-Speed Data Bus," *IEICE Trans. Electronics*, Vol. E77-C, No. 10, Oct. 1994, pp. 1694-1700.

[42]. M. R. Feldman, et. al, "Comparison between optical and electrical interconnects based on power and speed considerations," *Applied Optics*, Vol. 27, No. 9, 1988, pp. 1742-1751.

[43]. P.R.Haugen, S. Rychnovsky, A. Husain, and L.D. Hutchenson, "Optical Interconnects for high speed computing," *Opt. Eng.*, Vol. 25, No. 10, 1986, pp. 1076-1084.

[44]. S.E. Schacham, et. al., "Waveguides as Interconnects for High Performance Packaging," *Proc. 9th Int. Electron. Packaging Conf.*, Vol. II, 1989, pp. 1003-1013.

[45]. H.S. Hinton, "Digital Switching Systems Based on the SEED Technology and Free-Space Optical Interconnects," *Photonics Switching and Interconnects*, A. Marakchi ed., Marcel Dekker, Inc., 1994, pp. 213-247.

[46]. N. Sugiura, K. Yasuda, H. Oka, "High-Speed Signal Transimission Characteristics for Improved Coaxial Printed Board Connector in a Rack System," *The Int. J. of Microcircuits & Elect. Packaging*, Vol. 18, No. 2, 2nd quarter 1995, pp. 85-91.

[47]. Technical Data for Cray T-90 Backplane.

[48]. N.C. Craft, A.Y. Feldblum, "Optical interconnects based on arrays of surface-emitting lasers and lenslets," *Applied Optics*, Vol. 31, No. 11, 1992, pp. 1735-1739.

[49]. M.J. Goodwin, et. al., "Optoelectronic Component Arrays for Optical Interconnection of Circuits and Subsystems," *J. of Lightwave Tech.*, Vol. 9, No. 12, 1991, pp. 1639-1645.

[50]. I.R. Redmond, E. Schenfeld, "A Free Space Optical Interconnection Network for Massively Parallel Processing," *IEEE LEOS Newsletter*, June 1995, pp. 10-13.